

Experimental and Theoretical Investigations of Multifunctional (Li, Nd) Co-Doped ZnO Ceramics for the Application in Microelectronics

Md. Zahidur Rahaman

*A Dissertation Submitted to the Department of Physics, Bangladesh
University of Engineering and Technology in Partial Fulfillment of the
Requirement for the Degree of Master of Science in Physics*



Department of Physics
BANGLADESH UNIVERSITY OF ENGINEERING AND TECHNOLOGY
DHAKA-1000, BANGLADESH

June, 2019

Experimental and Theoretical Investigations of Multifunctional (Li, Nd) Co-Doped ZnO Ceramics for the Application in Microelectronics

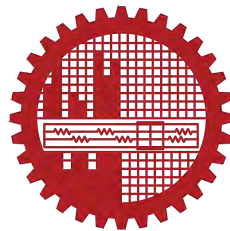
by

Md. Zahidur Rahaman

Student ID: 1017142510

Session: October 2017

MASTER OF SCIENCE



Department of Physics
BANGLADESH UNIVERSITY OF ENGINEERING AND TECHNOLOGY
DHAKA-1000, BANGLADESH

June, 2019



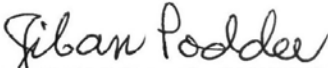

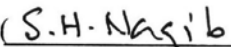


**BANGLADESH UNIVERSITY OF ENGINEERING AND TECHNOLOGY
DEPARTMENT OF PHYSICS, DHAKA -1000, BANGLADESH**

CERTIFICATION OF THESIS

The thesis titled “**EXPERIMENTAL AND THEORETICAL INVESTIGATIONS OF MULTIFUNCTIONAL (Li, Nd) CO-DOPED ZnO CERAMICS FOR THE APPLICATION IN MICROELECTRONICS**” submitted by **MD. ZAHIDUR RAHAMAN**, Roll No.: 1017142510, Session: October 2017, has been accepted as satisfactory in partial fulfillment of the requirement for the degree of **Master of Science (M.Sc.) in Physics** on 16 June, 2019.

BOARD OF EXAMINERS

1. () Chairman
Dr. A. K. M. Akther Hossain (Supervisor)
Professor, Department of Physics, BUET.
2. () Member
Professor Dr. Md. Forhad Mina
Head, Department of Physics, BUET. (Ex-Officio)
3. () Member
Dr. Jean Podder
Professor, Department of Physics, BUET.
4. () Member
Dr. Mohammad Jellur Rahman
Associate Professor, Department of Physics, BUET.
5. () Member
Dr. Salch Hasan Naqib
Professor, Department of Physics,
University of Rajshahi, Rajshahi-6205, Bangladesh. (External)

CANDIDATE'S DECLARATION

It is hereby declared that this thesis or any part of it has not been submitted elsewhere for the award of any degree or diploma.

Md. Zahidur Rahaman

To

My father Md. Habibur Rahaman

My late mother Jarina Begum

My mother Sharmin Aktar

who sacrificed immensely so that their children can gain a fairer share of life.

ACKNOWLEDGMENTS

All praise for Allah who has created us and given a greatest status among his all creations. I am so grateful to almighty Allah for giving me strength, courage, patience and ability to complete this study. I have been extremely fortunate in my life to be surrounded by many loving and inspiring people whose friendship, companionship, and support has been a gift to my life. They have each shaped me personally and professionally in unique ways, and I am forever grateful for their presence by my side. Expressing my gratitude for their roles in my life in these few pages is the smallest thing I could do to treasure them.

Firstly, I would like to express my deepest sense of gratitude to my honorable supervisor sir Prof. Dr. A.K.M. Akther Hossain for his scholastic supervision, valuable guidance and helpful discussion throughout the progress of this work. His undaunted capacity for work and enthusiasm for scientific investigations are always a great source of inspiration to me. I am highly grateful to him for allowing me to conduct independent research.

I am extremely grateful to Prof. Dr. Md. Forhad Mina, Head, Department of Physics, BUET, for kindly permitting me to carry out this research in the Physics Lab. and to the BUET authorities for providing the necessary financial grant for the research.

I would like to express my gratitude to Prof. Dr. Md. Abu Hashan Bhuiyan, Prof. Dr. Jiban Podder, Prof. Dr. Md. Feroz Alam Khan, Mrs. Fahima Khanam, Prof. Dr. Md. Mostak Hossain, Prof. Dr. Md. Rafi Uddin, Prof. Dr. Nasreen Akter, Prof. Dr. Mohammed Abdul Basith, Dr. Mohammad Jellur Rahman, Dr. Mohammad Abu Sayem Karal, Dr. Muhammad Samir Ullah, Dr. Md. Azizur Rahman, Dr. Muhammad Rakibul Islam and all other teachers of Department of Physics, BUET for their sincere cooperation. I would also like to convey my thanks to the employees of the department of Physics, BUET for their co-operation.

I am grateful to my undergrad supervisor Md. Atikur Rahman and all other teachers of Department of Physics, Pabna University of Science and Technology for their extensive encouragement. My university life would not have been the same without the guidance and inspiration of them.

I am so thankful to all members of the Solid State Physics Research Laboratory, Department of Physics, BUET for their cooperation and constant support throughout the study. I would like to extend my gratitude to all of my friends, younger and relatives for their good wishes.

Finally my parents, Md. Habibur Rahaman, Jarina Begum and Sharmin Aktar Lipi: it is indeed difficult for me to write words that sufficiently express my love for you, and my appreciation for all you have gone through in your life for me. I will always remain indebted to you for yours unconditional love and support. Your integrity throughout all the aspects and periods of your lives has set a standard for me, with which I actively gauge my actions and decisions in life. I would also like to acknowledge the moral support and the sustained inspiration of all members of my family. This dissertation would have never been possible without their love, affection, encouragement and sacrifices.

The Author

Md. Zahidur Rahaman

ABSTRACT

Multifunctional materials have become essential for the fabrication of miniaturized, light weight, low power consumption, cost-effective and high performance modern electronic devices. Pure and (Li, Nd) co-doped multifunctional $(\text{Nd}_{0.5}\text{Li}_{0.5})_x\text{Zn}_{1-x}\text{O}$ ceramics have been prepared by using the conventional solid state reaction route for the first time. Phase identification and structural analysis of the investigated samples have been carried out by X-ray diffraction technique. The XRD patterns confirm the formation of wurtzite hexagonal type zinc oxide. Surface morphology and microstructure of all the samples have been investigated by using FESEM and EDS analysis. FESEM images confirm that all the compositions contain randomly aligned non-uniform grains in size and shape due to very high sintering temperature. A high precision impedance analyzer has been used to study the frequency dependent dielectric and magnetic properties. A room temperature colossal dielectric constant $\geq 10^3$ with very low dielectric loss is obtained for $(\text{Nd}_{0.5}\text{Li}_{0.5})_{0.01}\text{Zn}_{0.99}\text{O}$ ceramics sintered at 1623 K. The origin of giant dielectric constant has been investigated by using the electric modulus spectroscopy and impedance analysis. For further justification and interpretation of the obtained results a DFT based first principles study have been carried out by using the plane wave pseudopotential approach. The present study provides a new route to design optimal multifunctional materials and related devices for further research and technological applications.

CONTENTS

Acknowledgments	iv
Abstract	vi
List of Figures	xi
List of Tables	xvi
1. Introduction	1
1.1 Background	1
1.2 Literature Review	2
1.3 Objectives of the Present Study	4
1.4 Outline of the Thesis	5
Bibliography	6
2. Theoretical Background	8
2.1 General Features of Zinc Oxide	10
2.1.1 Chemical properties of ZnO	10
2.1.2 Structural properties of ZnO	11
2.1.3 Mechanical properties of ZnO	13
2.1.4 Optical properties of ZnO	14
2.1.5 Electrical properties of ZnO	14
2.2 Dielectrics	15
2.2.1 Dielectric polarization	16
2.2.2 Mechanisms of polarization	17
2.2.3 Dielectric properties	19
2.2.4 Dielectric relaxation	22
2.2.5 Dependence of dielectric properties on various factors	23

2.2.6	ZnO as a dielectric	24
2.3	Magnetism	24
2.3.1	Permeability	25
2.3.2	Magnetism in ZnO	27
	Bibliography	29
3.	Methodology of Sample Preparation	33
3.1	Sample Preparation Techniques	33
3.2	Standard Solid State Reaction Route	34
3.2.1	Reagents	35
3.2.2	Mixing	35
3.2.3	Calcination	36
3.2.4	Green body preparation	37
3.2.5	Sintering	39
3.2.6	Etching	41
3.3	Synthesis of the Present Samples	41
	Bibliography	44
4.	Experimental Techniques	45
4.1	Structural and Morphological Characterization	45
4.1.1	X-ray diffraction	45
4.1.2	Microstructural studies by SEM/FESEM	49
4.1.3	Energy-dispersive X-ray spectroscopy	53
4.2	Density and Porosity Calculation	55
4.3	Dielectric Properties Measurement	56
4.3.1	Impedance Analyzer	57
4.3.2	Theory and working principle of Impedance Analyzer	57

4.3.3	Dielectric measurement techniques	59
4.3.4	Measurement of ac-conductivity	60
4.4	Impedance Spectroscopy	61
4.5	Modulus Spectroscopy	64
4.6	Study of Magnetic Properties	64
4.6.1	Complex permeability measurement	64
	Bibliography	67
5.	Theoretical Methodology	69
5.1	First-principles Techniques	69
5.1.1	The Schrödinger equation	70
5.1.2	Born-Oppenheimer Approximation	70
5.1.3	Hartree-Fock approximations	71
5.1.4	Density Functional Theory	72
5.2	Generalized Gradient Approximation	72
5.3	k-point Sampling	73
5.4	Cutoff energy	74
5.5	Pseudopotential	75
5.6	Ground State Energy	77
5.7	Computation of Different Properties	78
	Bibliography	83
6.	Results and Discussion	85
6.1	Structural Analysis	85
6.2	Density and Porosity	92
6.3	Morphological Analysis	94
6.4	Energy Dispersive X-ray Analysis	100
6.5	Dielectric Properties	101
6.5.1	Dielectric constant	101

6.5.2	Dielectric loss factor	102
6.5.3	Composition and T_s dependence of ϵ' and $\tan\delta$	104
6.5.4	The ac-conductivity	106
6.5.5	Complex impedance spectra analysis	107
6.6	Magnetic Properties	111
6.6.1	Complex initial permeability	111
6.6.2	Relative quality factor	113
6.7	Theoretical Analysis	114
6.7.1	Structural properties	114
6.7.2	Mechanical properties	115
6.7.3	Electronic properties	117
6.7.4	Optical properties	122
	Bibliography	126
7.	Conclusions	131
7.1	Summary	131
7.2	Future Work	134
	List of Publications	136

LIST OF FIGURES

2.1	A schematic illustration of ZnO UV laser diode and the corresponding device structure.	9
2.2	ZnO as anode material of Li-ion battery.	9
2.3	Powder form of zinc oxide.	10
2.4	Zincblende phase of zinc oxide. Zn atoms are shown as violet sphere and O atoms are shown as yellow sphere.	12
2.5	Wurtzite phase of zinc oxide. Zn atoms are shown as gray sphere and O atoms are shown as yellow sphere.	12
2.6	A parallel plate capacitor, where the electrodes are separated by vacuum and a dielectric material.	15
2.7	Non-polar dielectric structure polarizing with external applied field.	16
2.8	(a) Imposed forces (torque) acting on a dipole by an electric field. (b) Final dipole alignment with the field.	17
2.9	Frequency dependent typical dielectric polarization.	18
2.10	Equivalent circuit diagrams: (a) capacitive cell, (b) charging loss current and (c) loss tangent.	21
2.11	Impedance diagrams (top) and Cole-Cole diagrams (bottom) for one polarizable specie in the dielectric (a) and typical Debye relaxation with two polarizable species (b). Impedance diagram is not an appropriate plot to observe the relaxation process.	23
2.12	Various types of magnetism.	25
3.1	Balance, mortar and pestle.	36
3.2	Typical diagram of a crucible and a programmable electric furnace.	37
3.3	Schematic diagram of uniaxial pressing technique.	38

3.4	Typical diagram of a Hydraulic press.	39
3.5	Schematic representation of sintering stages: (a) green body, (b) initial stage, (c) intermediate stage and (d) final stage.	40
3.6	Graphical representation for the synthesis of ceramics samples by the solid-state reaction route.	42
3.7	Cylindrical and toroid shaped green body.	43
4.1	Graphical representation of X-ray diffraction technique.	46
4.2	Schematic diagram for a typical X-ray powder diffraction experiment.	47
4.3	A typical X-ray diffractometer used for XRD.	48
4.4	Various types of signals which are generated by electron-matter interactions.	50
4.5	Schematic diagram of scanning electron microscope (SEM).	51
4.6	Field emission scanning electron microscope (FESEM) setup.	52
4.7	A typical setup for EDX/EDS.	53
4.8	Characteristic X-ray generation process.	54
4.9	Some techniques for the measurement of dielectric properties.	56
4.10	A typical diagram of an impedance analyzer.	57
4.11	Experimental setup of Wayne Kerr Impedance Analyzer (6500B).	60
4.12	Silver paste painted two probe arrangements on the sintered sample.	60
4.13	An impedance plot with the corresponding equivalent circuit.	63
4.14	Impedance plot for an ideal polycrystalline sample with the equivalent circuit.	63
4.15	Toroid shaped sample for the measurement of permeability.	65
5.1	Flowchart representing the Hartree–Fock method.	71

5.2	A schematic illustration of the all-electron and pseudized wavefunctions and potentials.	76
5.3	The crystal structure ($2 \times 2 \times 2$ supercell) of Li and Nd co-doped ZnO.	79
6.1	(a) The X-ray diffraction pattern of $(\text{Nd}_{0.5}\text{Li}_{0.5})_x\text{Zn}_{1-x}\text{O}$ ceramics sintered at 1623 K and (b) the shifting of peak corresponding to (101) plane.	86
6.2	(a) The X-ray diffraction pattern of $(\text{Nd}_{0.5}\text{Li}_{0.5})_x\text{Zn}_{1-x}\text{O}$ ceramics sintered at 1648 K and (b) the shifting of peak corresponding to (101) plane.	86
6.3	Refined X-ray diffraction profiles of $(\text{Nd}_{0.5}\text{Li}_{0.5})_x\text{Zn}_{1-x}\text{O}$ ceramics sintered at 1623 K.	88
6.4	(a) Variation of lattice constants and (b) unit cell volume, as a function of doping concentration of $(\text{Nd}_{0.5}\text{Li}_{0.5})_x\text{Zn}_{1-x}\text{O}$ ceramics.	90
6.5	Variation of crystallites size as a function of doping content of $(\text{Nd}_{0.5}\text{Li}_{0.5})_x\text{Zn}_{1-x}\text{O}$ ceramics.	91
6.6	(a) Sintering temperature dependent bulk density of $(\text{Nd}_{0.5}\text{Li}_{0.5})_x\text{Zn}_{1-x}\text{O}$ ceramics. (b) Doping content dependent bulk density, theoretical density and porosity of $(\text{Nd}_{0.5}\text{Li}_{0.5})_x\text{Zn}_{1-x}\text{O}$ ceramics sintered at 1623 K.	93
6.7	FESEM micrographs of $(\text{Nd}_{0.5}\text{Li}_{0.5})_x\text{Zn}_{1-x}\text{O}$ ceramics sintered at 1623 K. Micrographs illustrated in the left (right) panel is 3000 (5000) times magnified.	96
6.8	FESEM micrographs of $(\text{Nd}_{0.5}\text{Li}_{0.5})_x\text{Zn}_{1-x}\text{O}$ ceramics sintered at 1648 K. Micrographs illustrated in the left (right) panel is 1000 (3000) times magnified.	97
6.9	FESEM micrographs of $(\text{Nd}_{0.5}\text{Li}_{0.5})_x\text{Zn}_{1-x}\text{O}$ ceramics sintered at 1573, 1623, and 1648 K.	98
6.10	Variation of average grain size as a function of (a) doping content and (b) sintering temperature of $(\text{Nd}_{0.5}\text{Li}_{0.5})_x\text{Zn}_{1-x}\text{O}$.	99
6.11	EDX spectra of 1% (Li, Nd) co-doped ZnO ceramics sintered at 1623 K.	

- (a) Image used for EDX analysis. Information corresponding to (b) point 001, (c) point 002 and (d) point 003, of $\text{Nd}_{0.005}\text{Li}_{0.005}\text{Zn}_{0.99}\text{O}$ ceramics. 100
- 6.12** Variation of dielectric constant as a function of frequency of $(\text{Nd}_{0.5}\text{Li}_{0.5})_x\text{Zn}_{1-x}\text{O}$ ceramics sintered at (a) 1473 K, (b) 1573 K, (c) 1623 K and (d) 1648 K. 102
- 6.13** Variation of loss tangent as a function of frequency of polycrystalline $(\text{Nd}_{0.5}\text{Li}_{0.5})_x\text{Zn}_{1-x}\text{O}$ ceramics sintered at (a) 1473 K, (b) 1573 K, (c) 1623 K and (d) 1648 K. 103
- 6.14** (a) The permittivity and loss tangent as a function of doping concentration of $(\text{Nd}_{0.5}\text{Li}_{0.5})_x\text{Zn}_{1-x}\text{O}$ ceramics sintered at 1623 K. (b) Sintering temperature dependent permittivity and loss tangent of 1% (Li, Nd) co-doped ZnO ceramics. 105
- 6.15** Variation of ac-conductivity with frequency of polycrystalline $(\text{Nd}_{0.5}\text{Li}_{0.5})_x\text{Zn}_{1-x}\text{O}$ ceramics sintered at (a) 1473 K, (b) 1573 K, (c) 1623 K and (d) 1648 K. 107
- 6.16** Variation of $\log\sigma_{ac}$ with $\log\omega$ of polycrystalline $(\text{Nd}_{0.5}\text{Li}_{0.5})_x\text{Zn}_{1-x}\text{O}$ ceramics sintered at (a) 1473 K, (b) 1573 K, (c) 1623 K and (d) 1648 K. 108
- 6.17** Variation of (a) Z' and (b) Z'' , as a function of frequency of $(\text{Nd}_{0.5}\text{Li}_{0.5})_x\text{Zn}_{1-x}\text{O}$ ceramics sintered at 1623 K. 109
- 6.18** Variation of (a) M' and (b) M'' , as a function of frequency of polycrystalline $(\text{Nd}_{0.5}\text{Li}_{0.5})_x\text{Zn}_{1-x}\text{O}$ ceramics sintered at 1623 K. 109
- 6.19** The Cole-Cole plot of polycrystalline $(\text{Nd}_{0.5}\text{Li}_{0.5})_x\text{Zn}_{1-x}\text{O}$ ceramics sintered at 1623 K. (a) Z'' vs Z' plot at low frequency region. (b) Z'' vs Z' plot at high frequency region. (c) Equivalent circuit model. 110
- 6.20** Frequency dependent real part of complex initial permeability μ'_i of polycrystalline $(\text{Nd}_{0.5}\text{Li}_{0.5})_x\text{Zn}_{1-x}\text{O}$ ceramics sintered at (a) 1473 K, (b) 1573 K, (c) 1623 K and (d) 1648 K. 112

6.21	Frequency dependent RQF of polycrystalline $(\text{Nd}_{0.5}\text{Li}_{0.5})_x\text{Zn}_{1-x}\text{O}$ ceramics sintered at (a) 1473 K, (b) 1573 K, (c) 1623 K and (d) 1648 K.	113
6.22	The crystal structure ($2 \times 2 \times 2$ supercell) of (Li, Nd) co-doped ZnO ceramics. (a) Three dimensional and (b) two dimensional view.	115
6.23	The band structure diagram of ZnO ceramics calculated by using (a) pure supercell, (b) Li-doped, (c) Nd-doped and (d) Li and Nd co-doped sample.	118
6.24	The total and partial density of states of ZnO ceramics simulated by using (a) pure supercell, (b) Li-doping at Zn-site, (c) Nd-doping at Zn-site and (d) Li and Nd co-doping at Zn-site of ZnO.	119
6.25	Dopant contribution at Fermi level of ZnO ceramics. (a) Pristine ZnO, (b) Li-doped ZnO, (c) Nd-doped ZnO and (d) (Li, Nd) co-doped ZnO.	120
6.26	The total charge density of (a) pristine ZnO, (b) Li-doped ZnO, (c) Nd-doped ZnO and (d) Li and Nd co-doped ZnO.	121
6.27	Calculated light absorption spectra of pure and metal doped ZnO ceramics. (a) Photon energy dependent and (b) wavelength dependent absorption coefficient.	123
6.28	The simulated photon energy dependent (a) Reflectivity, (b) Conductivity, (c) Real part of dielectric function and (d) Imaginary part of dielectric function of pristine and doped ZnO ceramics.	124

LIST OF TABLES

6.1	Refined crystallographic data of $(\text{Nd}_{0.5}\text{Li}_{0.5})_x\text{Zn}_{1-x}\text{O}$ ceramics.	89
6.2	Fractional atomic coordinates of $(\text{Nd}_{0.5}\text{Li}_{0.5})_x\text{Zn}_{1-x}\text{O}$ ceramics.	89
6.3	Bulk density, ρ_B of $(\text{Nd}_{0.5}\text{Li}_{0.5})_x\text{Zn}_{1-x}\text{O}$ ceramics at different sintering temperatures.	92
6.4	Bulk density, theoretical density and porosity of $(\text{Nd}_{0.5}\text{Li}_{0.5})_x\text{Zn}_{1-x}\text{O}$ ceramics sintered at 1623 K.	94
6.5	Average grain size of $(\text{Nd}_{0.5}\text{Li}_{0.5})_x\text{Zn}_{1-x}\text{O}$ sintered at 1573, 1623, and 1648 K.	95
6.6	The theoretical and experimental unit cell parameters of pristine and (Li, Nd) co-doped ZnO ceramics.	114
6.7	The evaluated elastic constants C_{ij} (GPa) and Cauchy pressure of pristine and (Li, Nd) co-doped ZnO ceramics.	116
6.8	The evaluated mechanical parameters of pristine and (Li, Nd) co-doped ZnO ceramics.	116

CHAPTER 1

INTRODUCTION

1.1 Background

Multifunctional materials have become essential for the fabrication of miniaturized, light weight, low power consumption, cost-effective and high performance modern electronic devices. These materials are capable to perform multiple functions in a system because of their particular properties. Multifunctional materials can be both naturally existing and specially engineered. For example, some traditional materials that possess very high mechanical strength can also be modified at the nanoscale to have other useful properties, such as self-heating, energy absorption etc. In nature numerous examples of multifunctional materials are present. Bio-materials contain healing, sensing, actuation, and other functions built into the primary structures of an organism. The materials that are able to respond to their environment have a great technological impact. In the recent years, such smart systems are being constructed in which material properties (such as electrical, optical or mechanical characteristics) respond to external stimuli. Generally, the multifunctionality of a material occurs at the nano to macro scales and on different compositional levels. Multifunctional advanced materials have tremendous potential and significant impact on a system. Such as,

1. Increasing efficiency of a system.
2. Lowering power consumption.
3. Reducing system weight.
4. Reducing system size.
5. Reducing system cost.
6. Reducing environmental effects.

7. Increasing versatility.

Recently, semiconductor hybrid materials (SHMs) have been the origin of great attention for their utilization as multifunctional material with enhanced dielectric, photocatalytic, magnetic and optical properties [1]. Especially, synthesis and properties of semiconductor-metal heterostructures such as SnO_2 , TiO_2 , ZnO , etc. (doped with Ag, Au, Nd and Gd) have been investigated in recent years due to their potential and crucial applications in cellular imaging, catalysis, immunoassay, luminescence tagging, spintronics and drug delivery [2–7]. Among these semiconductor hybrid materials zinc oxide (ZnO) is one of the most potential candidate in the metal oxide family. It has a number of applications including UV absorption, photocatalysts, spintronics, sensing, UV light-emitting devices etc. The properties of ZnO can be controlled by the particular amount of impurities doping and formation of defect cluster [8]. Oxygen vacancies play a significant role to tune the optical, electronic and even magnetic properties of ZnO . Therefore, particular impurity doping can be one possible route to fabricate multifunctional ZnO making it suitable for the applications in microelectronics.

1.2 Literature Review

Wurtzite-type ZnO is a well-known simple transition-metal oxide, which has been sufficiently studied for the semiconducting properties. However, besides its semiconducting properties ZnO is also capable to have room temperature ferromagnetic properties and good dielectric properties. Recently, it has been reported that, in Mg-doped ZnO ceramics, the colossal permittivity can reach nearly 10^4 due to the IBLC mechanism, indicating that ZnO could be another promising material of colossal permittivity [9]. Meanwhile, the (In, Li) co-doped ZnO ceramics exhibit giant permittivity nearly 10^3 due to hopping of the charged oxygen vacancies [10]. In 2018, You Wu *et al.* investigated the colossal dielectric behavior in (Li, Fe) co-doped ZnO ceramics [11]. Colossal dielectric constant nearly 10^4 with comparatively low dielectric loss nearly 0.61 have been achieved at 20 °C and 1 kHz which is the highest

in co-doped ZnO ceramics reported so far. They reported that the colossal permittivity is brought out by the step-like dielectric abnormalities resulting from the mix-valent ions of $\text{Fe}^{2+}/\text{Fe}^{3+}$ in major, while the grain boundaries tend to make the dominant contribution at the elevated temperature above the step-like abnormality. The defect dipole ($\text{Li}^+-\text{Fe}^{3+}$) can localize the electrons to a certain extent in the ZnO matrix inducing effective suppression of the dielectric loss. However, donor-acceptor co-doping in the ZnO does not always give rise to colossal permittivity. (Li, Al) co-doped ZnO is a conductor at room temperature and some others, like (Li, Sc) co-doped ZnO exhibit quite low permittivity up to 300 °C [11]. Moreover, giant dielectric behavior have also been reported in high pressure treated pure ZnO [12]. High pressure treated ZnO Ceramics sintered at 1050 °C possess the optimal giant room temperature dielectric constants nearly 10^4 at 100 Hz with low relative density and dielectric loss. The improved dielectric constant can be attributed to enhanced Maxwell–Wagner poly-dispersive relaxation due to the high pressure treating process, which makes ZnO porous ceramics a potential material for high dielectric constant applications [12].

On the other hand, rare earth and transition metal doped ZnO exhibits both semiconducting and useful ferromagnetic properties (known as Diluted Magnetic Semiconductor) which are the best candidates for opticomagnetic and spintronics applications. ZnO could become ferromagnetic, even at room temperature when doped with 1–10% of magnetic ions such as Mn, Fe, Co, Ni, etc [13, 14]. In ZnO based DMSs, the incorporation of TM ions is the primary means of controlling magnetic properties, and may also have an immense effect on the electrical conductivity, dielectric properties or other physical properties. The origin of ferromagnetic behavior of TM doped ZnO has been studied extensively by different groups and contradictory results were obtained in many cases. It is not clear yet whether it originates from the matrix itself or from secondary oxide phases. However, ferromagnetism is also reported in pure ZnO nanoparticles without doping with magnetic impurities [15]. The reason can be attributed to the absorption of certain organic molecules onto ZnO nanoparticles and various kinds of native defects such as oxygen

vacancies (V_O) or zinc interstitials (I_{Zn}) created during the heating process [16].

Li-doped ZnO exhibits outstanding optical and weak ferromagnetic properties [17, 18] whereas Nd-doped ZnO possesses good dielectric properties [19]. Hence, co-doping of Li and Nd into ZnO ceramics may possess outstanding ferroelectric, ferromagnetic and optical properties and can be used as a multifunctional advanced material.

1.3 Objectives of the Present Study

The main objective of the present study is to investigate the internal mechanisms of Li and Nd co-doped ZnO ceramics to find out a better multifunctional material in the transition metal oxide family with enhanced dielectric and magnetic properties for the application in high energy storage system and microelectronics. For implementing this objective the following works are performed step by step rigorously,

- Synthesis of $(Nd_{0.5}Li_{0.5})_xZn_{1-x}O$ (where, $x = 0.00, 0.01, 0.03, 0.05, 0.10$) by standard solid-state reaction route.
- Investigation of the crystal structure, surface morphology and average grain size of all the doped samples.
- Determination of the composition and frequency dependent dielectric constant, dielectric loss and AC-conductivity.
- Study of the dielectric relaxation mechanism of the studied compositions by Complex impedance spectroscopy(CIS).
- Evaluation of the complex initial permeability as a function of frequency of all the studied samples.
- Investigation of bonding and mechanical properties of all the doped samples through DFT based theoretical method.

1.4 Outline of the Thesis

The rest of the thesis is organized as follows:

- Chapter two provides a brief overview about the general properties of ZnO with detailed fundamentals of structural, magnetic and transport properties.
- The sample preparation methodologies that are used to prepare the studied compositions are described in chapter three.
- Chapter four provides a general description of the experimental techniques employed in this thesis work.
- The theoretical methodologies which are used to study the co-doped profile of ZnO are described in chapter five.
- The results associated with different properties investigated in this research are presented and discussed in chapter six.
- Chapter seven contains the concluding remarks and the scope of future work.

Bibliography

- [1] Huang, D., Liu, Z., Li, Y., and Liu, Y., "Colossal permittivity and dielectric relaxation of (Li, In) co-doped ZnO ceramics," *J. Alloy. Compd.*, vol. 698, pp. 200-206, 2017.
- [2] Lee, D.H., Kim, J.E., Han, T.H., Hwang, J.W., Jeon, S., Choi, S.Y., Hong, S.H., Lee, W.J., Ruoff, R.S. and Kim, S.O., "Versatile carbon hybrid films composed of vertical carbon nanotubes grown on mechanically compliant graphene films," *Adv. Mater.*, vol. 22(11), pp.1247-1252, 2010.
- [3] Nayral, C., Ould-Ely, T., Maisonnat, A., Chaudret, B., Fau, P., Lescouzeres, L. and Peyrelavigne, A., "A novel mechanism for the synthesis of tin/tin oxide nanoparticles of low size dispersion and of nanostructured SnO₂ for the sensitive layers of gas sensors," *Adv. Mater.*, vol. 11(1), pp.61-63, 1999.
- [4] Özgür, Ü., Alivov, Y.I., Liu, C., Teke, A., Reshchikov, M., Doğan, S., Avrutin, V.C.S.J., Cho, S.J. and Morkoç, H., "A comprehensive review of ZnO materials and devices," *J. Appl. Phys.*, vol. 98(4), pp.11, 2005.
- [5] Chao, L.C., Huang, J.W. and Chang, C.W., "Annealing effects on the properties of Nd containing ZnO nanoparticles prepared by sol-gel process," *Physica B*, vol. 404(8-11), pp.1301-1304, 2009.
- [6] Wang, R., Xin, J.H., Yang, Y., Liu, H., Xu, L. and Hu, J., "The characteristics and photocatalytic activities of silver doped ZnO nanocrystallites," *Appl. Surf. Sci.*, vol. 227(1-4), pp.312-317, 2004.
- [7] Dietl, T., Ohno, H., Matsukura, F., Cibert, J. and Ferrand, E.D., "Zener model description of ferromagnetism in zinc-blende magnetic semiconductors," *science*, vol. 287(5455), pp.1019-1022, 2000.
- [8] Kumar, S. and Sahare, P.D., "Nd-doped ZnO as a multifunctional nanomaterial," *J. Rare Earth*, vol. 30(8), pp.761-768, 2012.
- [9] Raj, C.J., Paramesh, G., Prakash, B.S., Meher, K.P. and Varma, K.B.R., "Origin of giant dielectric constant and conductivity behavior in Zn_{1-x}Mg_xO (0 ≤ x ≤ 0.1) ceramics," *Mater. Res. Bull.*, vol. 74, pp.1-8, 2016.
- [10] Huang, D., Liu, Z., Li, Y. and Liu, Y., "Colossal permittivity and dielectric relaxation of (Li, In) Co-doped ZnO ceramics," *J. Alloy. Compd.*, vol. 698, pp. 200-206, 2017.
- [11] Wu, Y., Li, J., Bai, H., He, S., Hong, Y., Shi, K. and Zhou, Z., "Colossal Dielectric Behavior

- and Dielectric Relaxation of (Li, Fe) Co-Doped ZnO Ceramics,” *Phys. Status Solidi Rapid Res. Lett.*, vol. 12(6), pp. 1800126, 2018.
- [12] Li, X., Xu, L., Liu, L., Wang, Y., Cao, X., Huang, Y., Meng, C. and Wang, Z., “High pressure treated ZnO ceramics towards giant dielectric constants,” *J. Mater. Chem. A*, vol. 2(39), pp.16740-16745, 2014.
- [13] Dolai, S., Sarangi, S.N., Hussain, S., Bhar, R. and Pal, A.K., “Magnetic properties of nanocrystalline nickel incorporated CuO thin films,” *J. Magn. Magn. Mater.*, 2019.
- [14] Sato, K. and Katayama-Yoshida, H., “Stabilization of ferromagnetic states by electron doping in Fe-, Co-or Ni-doped ZnO,” *Jpn. J. Appl. Phys.*, vol. 40(4A), pp.L334, 2001.
- [15] Garcia, M.A., Merino, J.M., Fernández Pinel, E., Quesada, A., De la Venta, J., Ruíz González, M.L., Castro, G.R., Crespo, P., Llopis, J., González-Calbet, J.M. and Hernando, A., “Magnetic properties of ZnO nanoparticles,” *Nano Lett.*, vol. 7(6), pp.1489-1494, 2007.
- [16] Das, J., Pradhan, S.K., Sahu, D.R., Mishra, D.K., Sarangi, S.N., Nayak, B.B., Verma, S. and Roul, B.K., “Micro-Raman and XPS studies of pure ZnO ceramics,” *Physica B*, vol. 405(10), pp. 2492-2497, 2010.
- [17] Ullah Awan, S., Hasanain, S.K., Bertino, M.F. and Hassnain Jaffari, G., “Ferromagnetism in Li doped ZnO nanoparticles: The role of interstitial Li,” *J. Appl. Phys.*, vol. 112.10, pp. 103924, 2012.
- [18] Chand, P., Gaur, A., Kumar, A. and Gaur, U.K., “Structural, morphological and optical study of Li doped ZnO thin films on Si (100) substrate deposited by pulsed laser deposition,” *Ceram. Int.*, vol. 40.8, pp. 11915-11923, 2014.
- [19] Divya, N.K. and Pradyumnan, P.P., “Enhancement of photocatalytic activity in Nd doped ZnO with an increase in dielectric constant,” *J. Mater. Sci. Mater. Electron.*, vol. 28.2, pp. 2147-2156, 2017.

CHAPTER 2

THEORETICAL BACKGROUND

The discovery of semiconducting materials has led to an outburst of research activities in materials science as well as condensed matter physics. Recently, scientists have made significant progress to fabricate a better dielectric material in the family of wide band gap semiconducting materials (Transition metal oxide family). One of the most important field of current interest in material science as well as condensed matter physics is the development of novel fundamental aspects and applications of these wide band gaped transition metal oxides through various impurity doping.

In transition metal oxides, zinc oxide (ZnO) is the widely studied and most promising candidate due to its various useful properties and wide variety of applications. ZnO is a wide-bandgap semiconductor of the II-VI semiconductor group. Due to oxygen vacancies or zinc interstitials ZnO is typically n-type [1]. This metal oxide possesses several favorable properties such as, high electron mobility, good transparency, wide bandgap and strong room-temperature luminescence [1]. Due to these several useful properties zinc oxide is used in light-emitting diodes [Fig. 2.1], transparent electrodes in liquid crystal displays, electronics as thin-film transistors, and energy-saving or heat-protecting windows [1]. ZnO is also a promising anode material for lithium-ion battery [Fig. 2.2] because it is cheap, biocompatible, and environmentally friendly. It is widely used as an additive in numerous materials and products including plastics, rubbers, ceramics, glass, lubricants, cement, paints, ointments, sealants, adhesives, pigments, foods, batteries, fire retardants, ferrites, and first-aid tapes [2]. In electronics, ZnO plays a vital role because of its semiconducting properties which make it a prospective candidate for optoelectronic device fabrication. It is also non-toxic, cost effective and sustainable. In solar cell technology, owing to its properties such as high transparency and conductivity, zinc oxide based dye sensitized solar cell has been developed and it has achieved rather good efficiency.

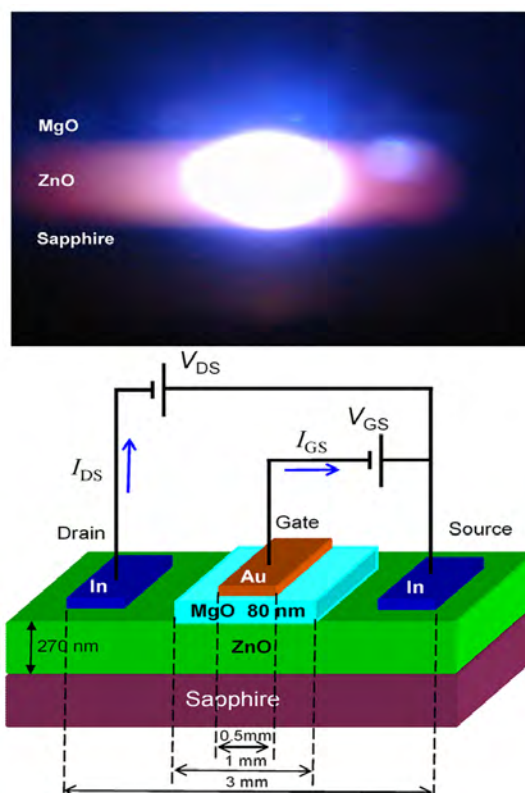


Fig. 2.1: A schematic illustration of ZnO UV laser diode and the corresponding device structure [25].

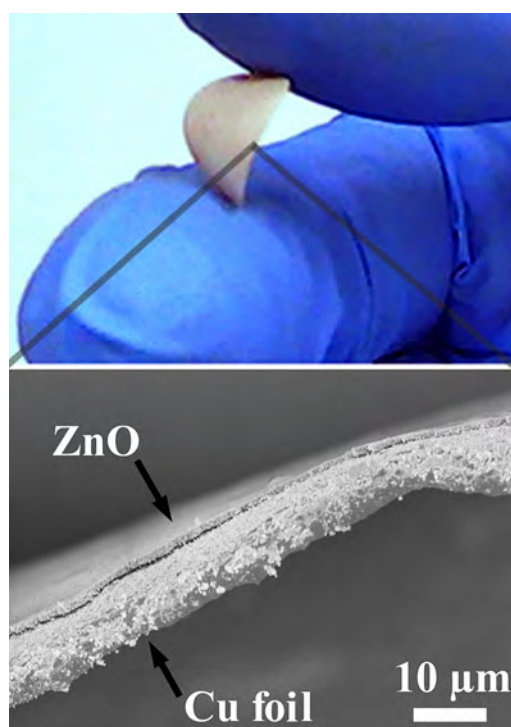


Fig. 2.2: ZnO as anode material of Li-ion battery [26].

The zinc oxide based solar cells are expected to be an alternative candidate for Silicon based solar cell as a replacement due to their thermal and chemical stability including the stability against photo corrosion [3]. Zinc oxide is used as different kind of sensors dependent on its properties. Due to the large band gap zinc oxide can also be used as ultraviolet absorber.

2.1 General Features of Zinc Oxide

Zinc oxide is an inorganic compound typically a white powder [Fig. 2.3] that is insoluble in water [2]. ZnO has direct band gap energy of approximately 3.2 to 3.4 eV at room temperature [4]. The crucial physical and chemical properties of zinc oxide is discussed in the following sections.

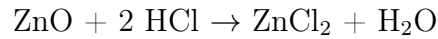


Fig. 2.3: Powder form of zinc oxide [2].

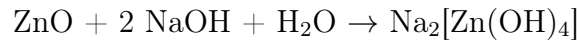
2.1.1 Chemical properties of ZnO

Naturally ZnO occurs as the rare mineral zincite, which usually contains manganese and other impurities having usually yellow to red color [5]. Crystalline ZnO is thermochromic, switching from white to yellow color when heated in air [6]. By reverting the process (by cooling) the white powder can also be obtained. This switching of color is caused by a small loss of oxygen to the environment at high

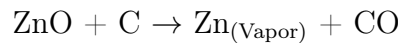
temperatures to form the non-stoichiometric Zn_{1+x}O , where $x = 0.00007$ at $800\text{ }^\circ\text{C}$ [6]. ZnO is typically an amphoteric oxide. Though it is insoluble in water, it is dissolved in most acids, such as hydrochloric acid [7]:



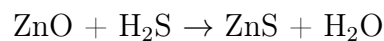
Solid form of ZnO is also dissolved in alkalis to produce soluble zincates [2]:



Zinc oxide usually decomposes into zinc vapor and oxygen at nearly $1975\text{ }^\circ\text{C}$ with a standard oxygen pressure. However in a carbothermic reaction, heating with carbon converts the oxide into zinc vapor at a much lower temperature (around $950\text{ }^\circ\text{C}$) [8].



Zinc oxide reacts slowly with fatty acids in oils to yield the corresponding carboxylates, for example oleate or stearate. Cement-like products are formed when ZnO is mixed with a strong aqueous solution of zinc chloride typically described as zinc hydroxy chlorides [9]. Zinc oxide also forms cement-like material when treated with phosphoric acid [2]. ZnO reacts violently with magnesium and aluminium powders, with chlorinated rubber and linseed oil on heating causing fire and explosion hazard [10, 11]. It can also react with hydrogen sulfide to yield zinc sulfide [2].



2.1.2 Structural properties of ZnO

Zinc oxide possesses two main forms of crystal structure, cubic zincblende and hexagonal wurtzite [12]. The zincblende type structure can be stabilized by growing ZnO on substrates with cubic lattice structure [2]. At ambient conditions, the wurtzite (B4-type) structure is most stable and thus it is the most common form of ZnO [2]. Both the zincblende and wurtzite structured ZnO is illustrated in Fig. 2.4 and Fig. 2.5, respectively. Hexagonal and zincblende polymorphs have no inversion symmetry. This and other lattice symmetry properties result in piezoelectricity of

the hexagonal and zincblende ZnO, and pyroelectricity of hexagonal ZnO [2].

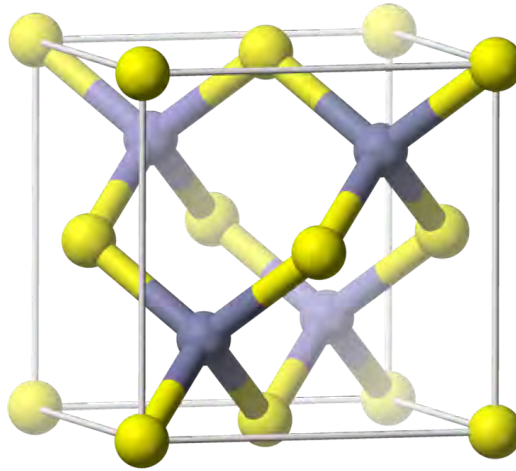


Fig. 2.4: Zincblende phase of zinc oxide [2]. Zn atoms are shown as violet sphere and O atoms are shown as yellow sphere.

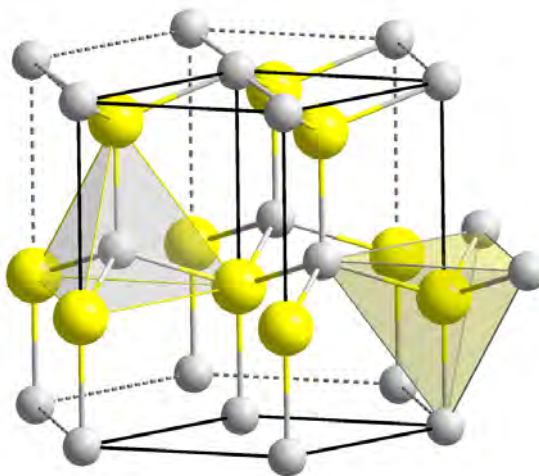


Fig. 2.5: Wurtzite phase of zinc oxide [2]. Zn atoms are shown as gray sphere and O atoms are shown as yellow sphere.

The hexagonal structure belongs to the point group 6 mm or C_{6v} , with the space group $P6_3mc$ or C_{6v}^4 [2]. The hexagonal lattice is characterized by two interconnecting sublattices of Zn^{2+} and O^{2-} , such that each Zn ion is surrounded by a tetrahedral of O ions and vice-versa. This tetrahedral coordination gives rise to

polar symmetry along the hexagonal axis. This polarity is responsible for a number of properties of ZnO, including its piezoelectricity and spontaneous polarization. It is also a key factor in crystal growth, etching and defect generation. The lattice constants are $a = 3.25 \text{ \AA}$ and $c = 5.2 \text{ \AA}$; their ratio $c/a = 1.60$ is very close to the ideal value for hexagonal cell $c/a = 1.633$ [13].

The bonding in ZnO is mostly ionic ($\text{Zn}^{2+}\text{-O}^{2-}$) with the corresponding radii of 0.074 nm for Zn^{2+} and 0.140 nm for O^{2-} . This property accounts for the preferential formation of wurtzite rather than zinc blende structure, as well as the strong piezoelectricity of ZnO [14]. However, the Zn–O bond also possesses weak covalent character and thus ZnO lies on the borderline between being classified as a covalent and ionic compound. Typically, oxygen and zinc planes are electrically charged due to the polar Zn–O bonds. To maintain electrical neutrality, those planes reconstruct at atomic level in most relative materials, but not in ZnO – its surfaces are atomically flat, stable and exhibit no reconstruction. This anomaly of zinc oxide is not fully explained yet [15].

2.1.3 Mechanical properties of ZnO

The elastic constants of zinc oxide are comparatively smaller than those of relevant III-V semiconductors. ZnO is classified as comparatively soft material with the approximate hardness value of 4.5 on the Mohs scale [16]. It has relatively high heat conductivity and heat capacity, high melting temperature and low thermal expansion [17]. These properties are beneficial for ceramic materials making ZnO suitable for many real life applications.

In the family of tetrahedrally bonded semiconductors, zinc oxide has the highest piezoelectric tensor, comparable to that of AlN and GaN [18]. This property makes ZnO a technologically important material for many piezoelectrical applications, which require a large electromechanical coupling [2].

2.1.4 Optical properties of ZnO

Zinc oxide is a wide band gap semiconductor that possesses luminescent properties and high optical transparency in the visible and near ultra violet regions. Due to these characteristics ZnO is a promising material for electronic and optoelectronic applications such as anti-reflecting coating, solar cells, and transparent conducting materials. The exciton binding energy of ZnO is nearly 60 meV. This high exciton binding energy allows ZnO for excitonic transitions even at room temperature indicating high radiative recombination efficiency for spontaneous emission as well as a lower threshold voltage for laser emission [19]. It creates the way for an intense near-band-edge excitonic emission at room and even higher temperatures. Numerous efforts is going on to fine tune the properties of ZnO by band gap engineering through various impurities doping to make it suitable and potential for different applications.

2.1.5 Electrical properties of ZnO

Zinc oxide possesses higher breakdown voltage and lower electronic noise due to its large band gap energy. It has ability to sustain large electric fields [2]. Typically zinc oxide has n-type character in nature even without any intentional impurity doping. Nonstoichiometry is usually the origin of n-type nature [20]. However, theoretical study suggests that unintentional substitutional hydrogen impurities can also be responsible for this type of nature of ZnO [21]. Generally, n-type doping can easily be achieved by substituting oxygen with group-VII elements and zinc with group-III elements such as Al, Ga, In.

Controllable p-type doping of ZnO is still difficult due to low solubility of p-type dopants and their compensation by abundant n-type impurities. Measurement of p-type in "intrinsically" n-type material is complicated by the inhomogeneity of samples [22]. Difficulty in p-type doping limit the electronic and optoelectronic applications of ZnO. P-type ZnO can be obtained with appropriate dopants to create

holes in the materials, including substitution at the O-site with group-V elements such as N, P, As, or Sb and substitution at the Zn-site with group-I elements, such as Li, Na, or K. However, many of these form deep acceptors and do not produce significant p-type conduction at room temperature [1].

Electron mobility of ZnO is nearly $2000 \text{ cm}^2/(\text{V}\cdot\text{s})$ at 80 K [23]. It varies strongly with temperature. The hole mobility varies in the range $5\text{-}30 \text{ cm}^2/(\text{V}\cdot\text{s})$ [24].

2.2 Dielectrics

The word dielectric is derived from the prefix dia, originally from Greek, which means “through” or “across”; thus, the dielectric is referred to as a material that permits the passage of the electric field or electric flux, but not particles [27]. Dielectrics are defined as an electrical insulator that can be polarized by an applied electric field. No current flows in them because, unlike metals, they have no loosely bound, or free, electrons that may drift through the material. Instead, electric polarization occurs. Because of dielectric polarization, positive charges are displaced toward the field and negative charges shift in the opposite direction. This creates an internal electric field which reduces the overall field within the dielectric itself. A typical dielectric polarization is shown in Fig. 2.6.

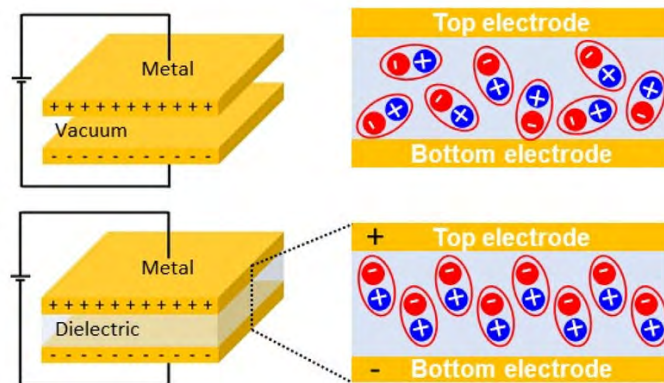


Fig. 2.6: A parallel plate capacitor, where the electrodes are separated by vacuum and a dielectric material [28].

The study of dielectric properties concerns storage and dissipation of electric energy in materials. a good dielectric (or good insulator) should have a relative high band gap to obtain low equilibrium charge carrier density and high injection barriers at the contacts.

Dielectrics are broadly divided into two classes: Polar dielectrics and Non-polar dielectrics. In polar dielectrics, a shift has occurred in the atomic structure such that the positive and negative charges have an asymmetrical alignment producing an electric dipole. Non-polar dielectric materials lack this inherent dipole in the absence of a polarizing field, however when an external potential is applied, a dipole forms from a shift in the electron cloud as shown in Fig. 2.7 [29].

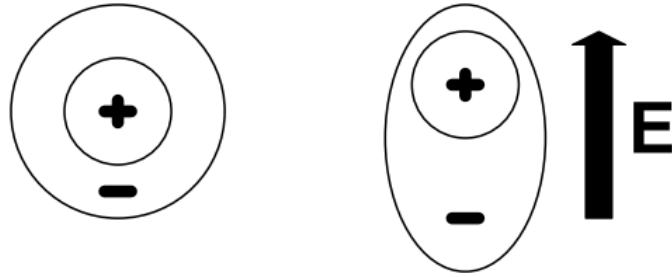


Fig. 2.7: Non-polar dielectric structure polarizing with external applied field [29].

2.2.1 Dielectric polarization

For every dipole, there is a separation between a positive and a negative electric charge. An electric dipole moment \mathbf{p} is associated with each dipole as follows:

$$\mathbf{p} = q \times \mathbf{d} \quad (2.1)$$

where q is the magnitude of each dipole charge and \mathbf{d} is the distance of separation between them. In the presence of an electric field \mathbf{E} , which is a vector quantity, a force (or torque) will come to bear on an electric dipole to orient it with the applied field; this phenomenon is illustrated in Fig. 2.8. The process of dipole alignment is termed as polarization [30].

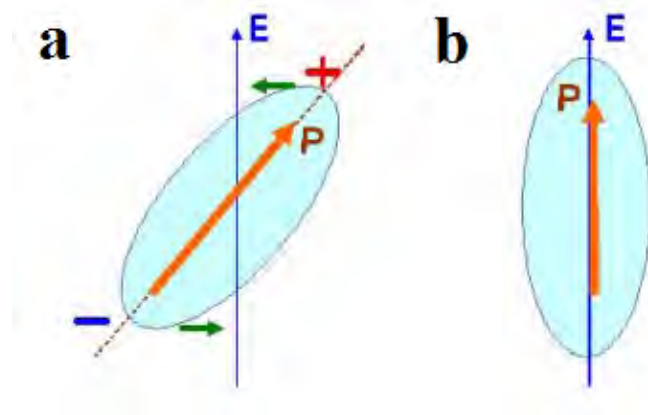


Fig. 2.8: (a) Imposed forces (torque) acting on a dipole by an electric field. (b) Final dipole alignment with the field [30].

2.2.2 Mechanisms of polarization

There are several mechanisms of polarization which can contribute to the dielectric response. Each one contributes to dielectric response but at different frequency regimes since they involve different polarizable species. There are four basic types of polarization mechanisms.

- (a) Ionic polarization.
- (b) Electronic polarization.
- (c) Orientational polarization.
- (d) Space-charge polarization.

Frequency dependent different types of polarization is illustrated in Fig. 2.9.

Ionic polarization is the polarization caused by relative displacements between positive and negative ions in ionic crystals. If a crystal or molecule consists of atoms of more than one kind, the distribution of charges around an atom in the crystal or molecule leans to positive or negative. As a result, when lattice vibrations or molecular vibrations induce relative displacements of the atoms, the centers of positive and negative charges are also displaced. The locations of these centers are affected by the symmetry of the displacements. When the centers don't correspond, polarization arises in molecules or crystals. This polarization is called ionic polarization

[32]. Ionic polarization causes the ferroelectric effect as well as dipolar polarization.

Electronic polarization is a result of dipole moments induced by the electric field. Atoms are composed of heavy nuclei surrounded by negative electron clouds. In the absence of an external field the movements of the electrons are such that the resultant orbital paths are symmetrical about the nucleus. These orbital paths become distorted by an external electric field because the paths of the electrons tend to shift against the direction of the applied field. A dipole is thus induced; this dipole is in effect positive on the left-hand side for the assumed direction of the field.

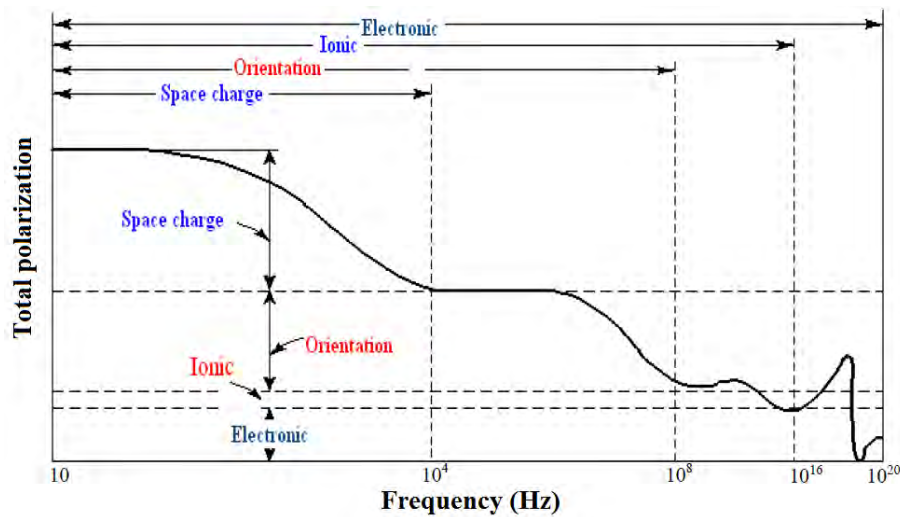


Fig. 2.9: Frequency dependent typical dielectric polarization [31].

Dipolar polarization is a polarization that is either inherent to polar molecules (orientation polarization), or can be induced in any molecule in which the asymmetric distortion of the nuclei is possible (distortion polarization) [32]. Orientation polarization results from a permanent dipole, e.g., that arising from the 104.45° angle between the asymmetric bonds between oxygen and hydrogen atoms in the water molecule, which retains polarization in the absence of an external electric field. The assembly of these dipoles forms a macroscopic polarization.

Space charge or interfacial polarization could exist in dielectric material if the density of charge carrier is not homogeneously distributed. This polarization is the slowest process, as it involves the diffusion of ions over several inter-atomic dis-

tances. The relaxation time for this process is related to the frequency of successful jumps of ions under the influence of the applied field, a typical value being 10^2 Hz. Correspondingly, space charge polarization occurs at lower frequencies ($10 - 10^4$ Hz). A type of polarization known as Maxwell- Wagner polarization is related to the space charge polarization because this type of polarization is occurred within the frequency range of $10 - 10^4$ Hz.

2.2.3 Dielectric properties

The study of dielectric properties provide a great deal of information about the suitability of the material for various applications. Dielectric constant, dielectric loss and dielectric break down are three important parameters for dielectric materials.

Dielectric Constant: The dielectric constant is a number relating the ability of a material to carry alternating current to the ability of vacuum to carry alternating current. The capacitance created by the presence of the material is directly related to the dielectric Constant of the material. Also, the dielectric constant is the ratio of the permittivity of a substance to the permittivity of free space. It is an expression of the extent to which a material concentrates electric flux, and is the electrical equivalent of relative magnetic permeability. As the dielectric constant increases, the electric flux density increases, if all other factors remain unchanged. This enables objects of a given size, such as sets of metal plates, to hold their electric charge for long periods of time, and/or to hold large quantities of charge.

The capacitance for a parallel plate capacitor with vacuum between the capacitor plates is given by,

$$C_o = \frac{\epsilon_o A}{d} \quad (2.2)$$

where ϵ_o is the permittivity of free space, A is the area of electrode and d is the separation between two electrodes.

When a dielectric (electrical insulator) fills the space between the plates, the ca-

capacitance of the capacitor is increased by a factor ϵ' , which is called the dielectric constant of the dielectric material. Therefore, for a parallel plate capacitor with a dielectric between the capacitor plates, the capacitance, C is given by,

$$C = \frac{\epsilon' \epsilon_0 A}{d} \quad (2.3)$$

Therefore, the dielectric constant of the given dielectric material can be written as,

$$\epsilon' = \frac{C}{C_0} \quad (2.4)$$

Dielectric loss: Dielectric loss is a special type of friction. When an electric field is applied to a dielectric material, dielectric polarization occurs. The total polarization is the sum of various contributions, e.g. electronic polarization due to the relative displacement of electrons and nuclei, dipolar polarization due to orientation of dipoles, ionic polarization due to the relative displacement of ions and interfacial or Maxwell-Wagner polarization when there are boundaries between the components of a heterogeneous system. Each mechanism contributes to the polarization up to a given frequency. Above that frequency, its contribution can no longer contribute and lowers the dielectric constant. At very low frequencies the polarization easily follows the alternating field, thus its contribution to the dielectric constant is maximum and no loss occurs. But at high frequency the polarization begins to lag behind the electric field and energy is dissipated. An ideal dielectric would allow no flow of electronic charge, only a displacement of charge via polarization. If a plate of such ideal material is placed between the capacitive cell shown in Fig. 2.10 and a dc voltage is applied, the current through the circuit would decay exponentially to zero with time. But this will not happen if an alternating (sine wave) electric field is applied. For real dielectric material, the current I has two vector components, real I_R and imaginary I_C . The condition of loss (not so good) is illustrated in Fig. 2.10(b) which is an equivalent circuit analogous of a resistance in parallel with the capacitor [33]. The current I_C represents a (watt less) capacitive current proportional to the charge stored in the capacitor. It is frequency

dependent and leads the voltage by 90° . On the other hand, the current I_R is ac conduction current in phase with the voltage V , which represents the energy loss or power dissipated in the dielectric. The resultant angle between the current and the voltage is ϕ somewhat less than 90° . The current in real capacitor lags slightly behind what it would be in an ideal capacitor. The angle of lag is defined as δ and the amount of lag becomes $\tan\delta$ or loss tangent.

By definition,

$$\tan\delta = \left| \frac{I_C}{I_R} \right| = \frac{\epsilon''}{\epsilon'} \quad (2.5)$$

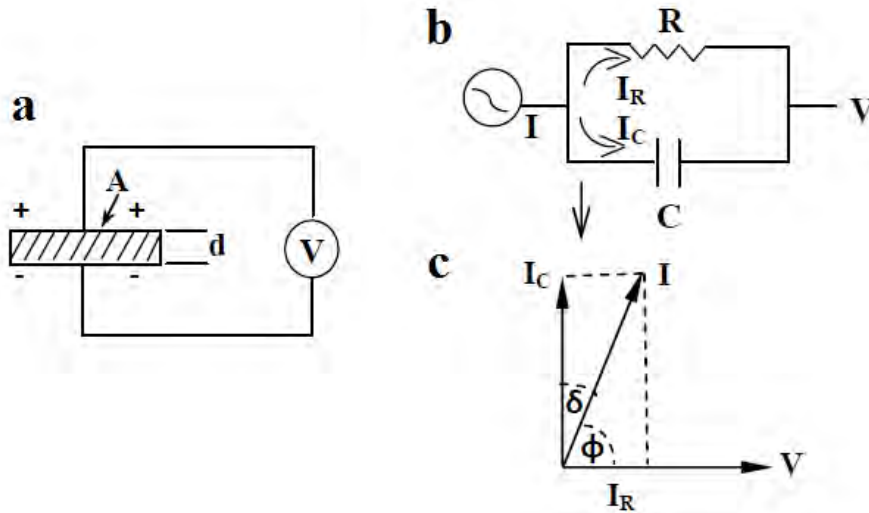


Fig. 2.10: Equivalent circuit diagrams: (a) capacitive cell, (b) charging loss current and (c) loss tangent [33].

Dielectric strength: The dielectric breakdown is sometimes referred to as the dielectric strength. The theoretical dielectric strength of a material is an intrinsic property of the bulk material, and is independent of the configuration of the material or the electrodes with which the field is applied. This "intrinsic dielectric strength" corresponds to what would be measured using pure materials under ideal laboratory conditions. The dielectric strength is referred to as the maximum electric field that an insulating material can withstand under ideal conditions without breaking down (i.e. without failure of its insulating properties). There are three main breakdown

mechanisms; thermal, electrical and discharge [27]. Discharge breakdown is similar to electrical breakdown but its cause is more specific. In this type of breakdown, the electric field is greater in a flaw than in the rest of the dielectric. This will cause the flaw to discharge, which leads to charge leakage and breakdown.

2.2.4 Dielectric relaxation

Dielectric relaxation is the momentary delay (or lag) in the dielectric constant of a material. This is usually caused by the delay in molecular polarization with respect to a changing electric field in a dielectric medium [32]. This relaxation is often described in terms of permittivity as a function of frequency, which can, for ideal systems, be described by the Debye equation. Debye relaxation is a very simple model where only two polarizable species are assumed in the dielectric. Thus, the dielectric parameters will undergo a single relaxation time τ which denotes the transition time between one species and the other one. Both are contributing to the dielectric response but at different frequencies. Each dielectric contribution is usually represented by using the impedance diagram ($-Z''$ vs. Z'), as illustrated in Fig. 2.11 (b). They can also be represented by an equivalent circuit depicted in Fig. 2.11. Both contributions can be easily distinguished with the impedance diagram but the relaxation process between them can only be evidenced using the Cole-Cole diagram. It is crucial to note that if only one species is taken into account in the dielectric, no mechanism of relaxation has to be expected (as shown in Fig. 2.11 (a)).

Maxwell-Wagner polarization processes should be taken into account during the investigation of inhomogeneous materials like suspensions or colloids, biological materials, phase separated polymers, blends, and crystalline or liquid crystalline polymers [34]. This dispersion occurs because of the charging of the interfaces within the material. This phenomenon does not arise from dielectric relaxation in the bulk phases of the material (which might also be present), but is a consequence of the boundary conditions on the fields at the interfaces between phases [27].

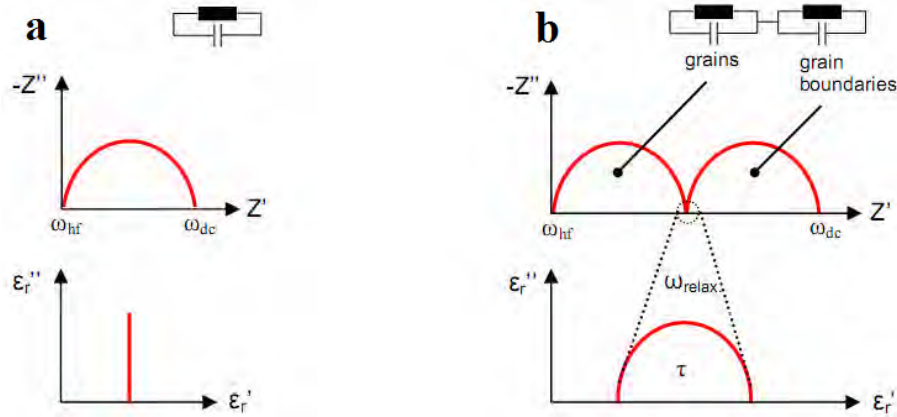


Fig. 2.11: Impedance diagrams (top) and Cole-Cole diagrams (bottom) for one polarizable specie in the dielectric (a) and typical Debye relaxation with two polarizable species (b). Impedance diagram is not an appropriate plot to observe the relaxation process [35].

2.2.5 Dependence of dielectric properties on various factors

The value of dielectric constant depends on several external factors, such as the frequency of the voltage applied to the dielectric, temperature, particle size etc.

The value of dielectric constant depends on frequency only in the case of polar dielectrics. The value of ϵ' of non-polar dielectrics does not depend on frequency when it changes within very broad limits [33]. When the frequency of alternative voltage increases the value of ϵ' of a polar dielectric at first remains invariable but above a certain critical frequency (when polarization fails to settle itself completely during one half periods) ϵ' begins to drop. At very high frequencies, ϵ' behaves like the typical value of non-polar dielectrics.

The process of electronic polarization in non-polar dielectric does not depend on temperature because temperature does not affect the electronic polarizability of molecules [33]. In polycrystalline materials at low frequency region space charges become more active during the arise of temperature and hence ϵ' increases. However, in some cases, the value of ϵ' may diminish when temperature rises, particularly in those substances in which ionic displacement intensifies the internal field and thereby electronic polarization.

2.2.6 ZnO as a dielectric

Wurtzite-type ZnO is a well-known simple transition-metal oxide, which has been sufficiently studied for the semiconducting properties. Recently, it has been reported that, in Mg-doped ZnO ceramics, the colossal permittivity can reach nearly 10^4 due to the IBLC mechanism, indicating that ZnO could be another promising material of colossal permittivity [41]. Meanwhile, the (In, Li) co-doped ZnO ceramics exhibit giant permittivity nearly 10^3 due to hopping of the charged oxygen vacancies [42].

Recently, a new dielectric polarization mechanism, e.g. electron-pinned defect dipoles (EPDD), has been proposed to explain the CP phenomenon of donor and acceptor co-doped metal oxide [43]. In this model, electrons are created by the donor atom. These electrons are localized by the presence of acceptor atom. These defect complexes formed by co-doping give rise to strong dipoles that are responsible for the high dielectric permittivity. The localized electrons also lead to extra low dielectric loss.

2.3 Magnetism

Magnetism is a class of physical phenomena that are mediated by magnetic fields. Electric currents and the magnetic moments of elementary particles give rise to a magnetic field, which acts on other currents and magnetic moments. The origin of the magnetic moments responsible for magnetization can be either microscopic electric currents resulting from the motion of electrons in atoms or the spin of the electrons or the nuclei [40]. Five basic types of magnetism can be described: diamagnetism, paramagnetism, ferromagnetism, antiferromagnetism and ferrimagnetism. In the presence of an externally applied magnetic field the atomic current loops created by the orbital motion of electrons respond to oppose the applied field. All materials display this type of weak repulsion to a magnetic field known as diamagnetism. Diamagnetism is observed in materials with filled electronic subshells where the magnetic moments are paired and overall cancel each other. All other

types of magnetic behavior observed in materials are at least partially attributed to unpaired electrons in atomic shells, often in the 3d or 4f shells of each atom. Materials whose atomic magnetic moments are uncoupled display paramagnetism. The most familiar effects occur in ferromagnetic materials, which are strongly attracted by magnetic fields and can be magnetized to become permanent magnets, producing magnetic fields themselves. Only a few substances are ferromagnetic; the most common ones are iron, nickel and cobalt and their alloys. Materials having atomic magnetic moments of equal magnitude that arranged in an antiparallel fashion display antiferromagnetism. Ferrimagnetism is a property exhibited by materials whose atoms or ions tend to assume an ordered but nonparallel arrangement of moments in zero applied field below a certain characteristic temperature known as the Neel temperature. Different types of magnetism are illustrated in Fig. 2.12.

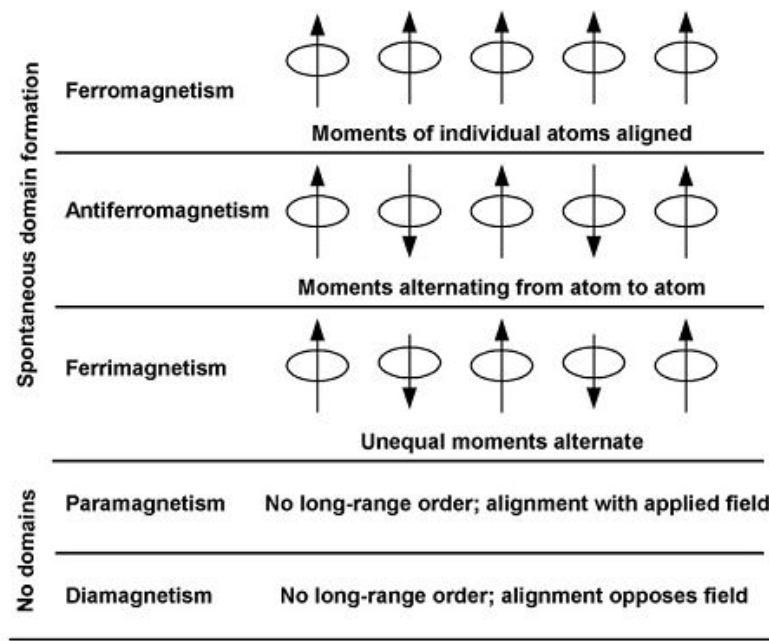


Fig. 2.12: Various types of magnetism [36].

2.3.1 Permeability

In electromagnetism, permeability is the measure of the ability of a material to support the formation of a magnetic field within itself [37]. Hence, it is the degree

of magnetization that a material obtains in response to an applied magnetic field. Permeability is defined as the proportionality constant between the magnetic field induction \mathbf{B} and applied field intensity \mathbf{H} :

$$\mathbf{B} = \mu\mathbf{H} \quad (2.6)$$

If the applied field is very low, approaching zero, the ratio will be called the initial permeability μ_i .

A useful tool for dealing with high frequency magnetic effects is the complex permeability. While at low frequencies in a linear material the magnetic field and the auxiliary magnetic field are simply proportional to each other through some scalar permeability, at high frequencies these quantities will react to each other with some lag time [38, 39]. A magnetic material subjected to an ac magnetic field can be written as,

$$H = H_o e^{i\omega t} \quad (2.7)$$

It is observed that the magnetic induction \mathbf{B} lag behind \mathbf{H} . This is caused by the presence of various losses and is thus expressed as,

$$B = B_o e^{i(\omega t - \delta)} \quad (2.8)$$

Here δ is the phase angle that marks the delay of \mathbf{B} with respect to \mathbf{H} . The permeability is then given by,

$$\mu = \frac{B}{H} = \frac{B_o e^{i(\omega t - \delta)}}{H_o e^{i\omega t}} = \frac{B_o e^{-i\delta}}{H_o} \quad (2.9)$$

By Euler's formula, the complex permeability can be translated from polar to rectangular form,

$$\mu = \frac{B_o}{H_o} \cos\delta - i \frac{B_o}{H_o} \sin\delta = \mu' - i\mu'' \quad (2.10)$$

where

$$\mu' = \frac{B_o}{H_o} \cos \delta \quad (2.11)$$

$$\mu'' = \frac{B_o}{H_o} \sin \delta \quad (2.12)$$

The real part μ' of complex permeability (μ), as expressed in equation (2.10) represents the component of \mathbf{B} which is in phase with \mathbf{H} , so it corresponds to the normal permeability. If there are no losses, we should have $\mu = \mu'$. The imaginary part μ'' corresponds to that of \mathbf{B} , which is delayed by phase angle 90° from \mathbf{H} [36]. The presence of such a component requires a supply of energy to maintain the alternating magnetization, regardless of the origin of delay.

The ratio of the imaginary to the real part of the complex permeability is called the loss tangent,

$$\tan(\delta) = \frac{\mu''}{\mu'} \quad (2.13)$$

which provides a measure of how much power is lost in a material versus how much is stored. This occurs due to the irreversible domain wall movements [36].

2.3.2 Magnetism in ZnO

Magnetic semiconductors are semiconductor materials that exhibit both ferromagnetism (or a similar response) and useful semiconductor properties. Doped Wide band-gap metal oxides such as zinc oxide (ZnO) and titanium oxide (TiO_2) are among the best candidates for industrial DMS due to their multifunctionality in opticomagnetic applications [44]. In particular, ZnO-based DMS with properties such as transparency in visual region and piezoelectricity have generated huge interest among the scientific community as a strong candidate for the fabrication of spin transistors and spin-polarized light-emitting diodes [45]. However, the origin of the observed ferromagnetism is unclear, and the existing theories can not satisfactorily

explain the observed phenomena.

Recently, room temperature ferromagnetism is reported in ZnO nanoparticles without doping with magnetic impurities but simply inducing an alteration of their electronic configuration [46]. Absorption of certain organic molecules onto ZnO nanoparticles modifies its electronic structure and gives rise to a ferromagnetic like behavior at room temperature even in the absence of magnetic ions. The reason can also be attributed to various kinds of native defects such as oxygen vacancies (V_O) or zinc interstitials (I_{Zn}) and their clusters created inside the bulk ceramics during heating by slow step sintering schedule (SSSS) [47].

Bibliography

- [1] Özgür, Ü., Alivov, Y.I., Liu, C., Teke, A., Reshchikov, M., Doğan, S., Avrutin, V.C.S.J., Cho, S.J. and Morkoç, H., “A comprehensive review of ZnO materials and devices,” *J. Appl. Phys.*, vol. 98 (4), pp. 11, 2005.
- [2] “Zinc Oxide.” Wikipedia, Wikimedia Foundation, 21 Feb. 2019, en.wikipedia.org/wiki/Zinc_oxide.
- [3] Anta, J.A., Guillen, E. and Tena-Zaera, R., “ZnO-based dye-sensitized solar cells,” *J. Phys. Chem. C*, vol. 116(21), pp. 11413-11425, 2012.
- [4] Srikant, V. and Clarke, D.R., “On the optical band gap of zinc oxide,” *J. Appl. Phys.*, vol. 83(10), pp. 5447-5451, 1998.
- [5] Klingshirn, C., “ZnO: material, physics and applications,” *ChemPhysChem*, vol. 8(6), pp. 782-803, 2007.
- [6] Wang, T., “An overview of IGCC systems”, *Integrated Gasification Combined Cycle (IGCC) Technologies*, pp. 1-80, Woodhead Publishing, 2017.
- [7] Earnshaw, Alan (1997) *Chemistry of the Elements* (2nd ed.). Butterworth-Heinemann. ISBN 0-08-037941-9
- [8] Greenwood, N. N. and Earnshaw, A. (1997) *Chemistry of the Elements*. Oxford: Butterworth-Heinemann. ISBN 978-0-7506-3365-9.
- [9] Nicholson, J.W. and Parker, L., “The chemistry of cements formed between zinc oxide and aqueous zinc chloride,” *J. Mater. Sci.*, vol. 33(9), pp. 2251-2254, 1998.
- [10] International Occupational Safety and Health Information Centre (CIS) Access date January 25, 2009.
- [11] Zinc oxide MSDS. hazard.com. Access date January 25, 2009.
- [12] Fierro, J. L. G (2006) *Metal Oxides: Chemistry & Applications*. CRC Press. p. 182. ISBN 978-0824723712.
- [13] Rossler, U. (1999) Landolt-Bornstein, New Series, Group III. Vol. 17B, 22, 41B.
- [14] Klingshirn, C.F., Waag, A., Hoffmann, A. and Geurts, J., (2010) *Zinc oxide: from fundamental properties towards novel applications*. Vol. 120, Springer Science & Business Media.
- [15] Baruah, S. and Dutta, J., “Hydrothermal growth of ZnO nanostructures,” *Sci. Technol. Adv. Mater.*, vol. 10(1), pp. 013001, 2009.

- [16] Battez, A.H., González, R., Viesca, J.L., Fernández, J.E., Fernández, J.D., Machado, A., Chou, R. and Riba, J., “CuO, ZrO₂ and ZnO nanoparticles as antiwear additive in oil lubricants,” *Wear*, vol. 265(3-4), pp. 422-428, 2008.
- [17] Porter, F. (1991) *Zinc Handbook: Properties, Processing, and Use in Design*. CRC Press. ISBN 978-0-8247-8340-2.
- [18] Dal Corso, A., Posternak, M., Resta, R. and Baldereschi, A., “Ab initio study of piezoelectricity and spontaneous polarization in ZnO,” *Phys. Rev. B*, vol. 50(15), pp. 10715, 1994.
- [19] Mang, A. and Reimann, K., “Band gaps, crystal-field splitting, spin-orbit coupling, and exciton binding energies in ZnO under hydrostatic pressure,” *Solid State Commun.*, vol. 94(4), pp. 251-254, 1995.
- [20] Look, D.C., Hemsley, J.W. and Sizelove, J.R., “Residual native shallow donor in ZnO,” *Phys. Rev. Lett.*, vol. 82(12), pp. 2552, 1999.
- [21] Janotti, A. and Van de Walle, C.G., “Hydrogen multicentre bonds,” *Nat. Mater.*, vol. 6(1), pp. 44, 2007.
- [22] Ohgaki, T., Ohashi, N., Sugimura, S., Ryoken, H., Sakaguchi, I., Adachi, Y. and Haneda, H., “Positive Hall coefficients obtained from contact misplacement on evident n-type ZnO films and crystals,” *J. Mater. Res.*, vol. 23(9), pp. 2293-2295, 2008.
- [23] Wagner, P. and Helbig, R., “Halleffekt und anisotropie der beweglichkeit der elektronen in ZnO,” *J. Phys. Chem. Solids*, vol. 35(3), pp. 327-335, 1974.
- [24] Ryu, Y.R., Lee, T.S. and White, H.W., “Properties of arsenic-doped p-type ZnO grown by hybrid beam deposition,” *Appl. Phys. Lett.*, vol. 83(1), pp. 87-89, 2003.
- [25] Liu, X.Y., Shan, C.X., Zhu, H., Li, B.H., Jiang, M.M., Yu, S.F. and Shen, D.Z., “Ultraviolet lasers realized via electrostatic doping method,” *Sci. Rep.*, vol. 5, pp. 13641, 2015.
- [26] Zheng, X., Shen, G., Wang, C., Li, Y., Dunphy, D., Hasan, T., Brinker, C.J. and Su, B.L., “Bio-inspired Murray materials for mass transfer and activity,” *Nat. Commun.*, vol. 8, pp.14921, 2017.
- [27] Shah, M. R., *Dielectric properties of alkaline earth (D = Ba, Sr, Ca) and rare earth (T = La, Nd) substituted polycrystalline D_{1-x}T_x(Ti_{0.5}Fe_{0.5})O₃ perovskite*, Ph. D. Thesis, Department of Physics, Bangladesh University of Engineering and Technology, 2013.
- [28] Park, S., Kim, C.H., Lee, W.J., Sung, S. and Yoon, M.H., “Sol-gel metal oxide dielectrics for

- all-solution-processed electronics,” *Mater. Sci. Eng.: R: Reports*, vol. 114, pp. 1-22, 2017.
- [29] Demarest, K., (1997). *Engineering Electromagnetics*. p. 416, Prentice-Hall.
- [30] Callister, W. D, J., (2005) *Materials Science and Engineering, An Introduction*. 5th edition, John Wiley & Sons.
- [31] Peláiz-Barranco, A. and Guerra, J.D.L.S., “Dielectric relaxation phenomenon in ferroelectric perovskite-related structures,” *In Ferroelectrics. InTech.*, 2010.
- [32] “Dielectric.” Wikipedia, Wikimedia Foundation, 20 Feb. 2019, en.wikipedia.org/wiki/Dielectric.
- [33] Miah, M. J., *Study of Multiferroic Properties of Rare Earth Substituted $x\text{Ba}_{0.95}\text{Sr}_{0.05}\text{TiO}_3 - (1-x)\text{BiFe}_{0.9}\text{Re}_{0.1}\text{O}_3$ Perovskite Ceramics*, Ph. D. Thesis, Department of Physics, Bangladesh University of Engineering and Technology, 2016.
- [34] Kremer, F. and Schönhals, A., (2003) *Molecular and collective dynamics of (polymeric) liquid crystals*. In *Broadband Dielectric Spectroscopy* (pp. 385-432). Springer, Berlin, Heidelberg.
- [35] Arveux, P. E., *Surface and interface properties of BaTiO_3 ferroelectric thin films studied by in-situ photoemission spectroscopy*, Ph. D. Thesis, Material science, L’UNIVERSITÉ BORDEAUX 1, 2009.
- [36] Mazumdar, S. C., *Synthesis and Investigation of Cu Doped Ni-Zn Ferrites and La, Dy Doped BiFeO_3 Multiferroic Composites*, Ph. D. Thesis, Department of Physics, Bangladesh University of Engineering and Technology, 2016.
- [37] “Permeability (Electromagnetism).” Wikipedia, Wikimedia Foundation, 20 Feb. 2019, [en.wikipedia.org/wiki/Permeability_\(electromagnetism\)](http://en.wikipedia.org/wiki/Permeability_(electromagnetism)).
- [38] Getzlaff, M., (2007) *Fundamentals of magnetism*. Springer Science & Business Media.
- [39] “Magnetic Hysteresis.” Wikipedia, Wikimedia Foundation, 15 Feb. 2019, en.wikipedia.org/wiki/Magnetic_hysteresis.
- [40] Chikazumi, S. and Graham, C.D., (1997) *Physics of Ferromagnetism*. (International Series of Monographs on Physics; 94). Oxford University Press.
- [41] Raj, C.J., Paramesh, G., Prakash, B.S., Meher, K.P. and Varma, K.B.R., “Origin of giant dielectric constant and conductivity behavior in $\text{Zn}_{1-x}\text{Mg}_x\text{O}$ ($0 \leq x \leq 0.1$) ceramics,” *Mater. Res. Bull.*, vol. 74, pp. 1-8, 2016.
- [42] Huang, D., Liu, Z., Li, Y. and Liu, Y., “Colossal permittivity and dielectric relaxation of (Li, In) Co-doped ZnO ceramics,” *J. Alloy. Comp.*, vol. 698, pp. 200-206, 2017.

- [43] Hu, W., Liu, Y., Withers, R.L., Frankcombe, T.J., Norén, L., Snashall, A., Kitchin, M., Smith, P., Gong, B., Chen, H. and Schiemer, J., “Electron-pinned defect-dipoles for high-performance colossal permittivity materials,” *Nat. Mater.*, vol. 12(9), pp. 821, 2013.
- [44] “Magnetic Semiconductor.” Wikipedia, Wikimedia Foundation, 4 Nov. 2018, en.wikipedia.org/wiki/Magnetic_semiconductor.
- [45] Ogale, S.B., “Dilute doping, defects, and ferromagnetism in metal oxide systems,” *Adv. Mater.*, vol. 22(29), pp. 3125-3155, 2010.
- [46] Garcia, M.A., Merino, J.M., Fernández Pinel, E., Quesada, A., De la Venta, J., Ruíz González, M.L., Castro, G.R., Crespo, P., Llopis, J., González-Calbet, J.M. and Hernando, A., “Magnetic properties of ZnO nanoparticles,” *Nano Lett.*, vol. 7(6), pp.1489-1494, 2007.
- [47] Das, J., Pradhan, S.K., Sahu, D.R., Mishra, D.K., Sarangi, S.N., Nayak, B.B., Verma, S. and Roul, B.K., “Micro-Raman and XPS studies of pure ZnO ceramics,” *Physica B*, vol. 405(10), pp. 2492-2497, 2010.

CHAPTER 3

METHODOLOGY OF SAMPLE PREPARATION

Multifunctional materials have become very essential for the fabrication of miniaturized, light weight, low power consumption, cost-effective and high performance modern electronic devices. Recently, semiconductor hybrid materials (SHMs) have been the origin of great attention for their utilization as multifunctional material with enhanced dielectric, photocatalytic, magnetic and optical properties [1]. However, it is very difficult to prepare such multifunctional material which possesses all the useful properties. These properties are not only influenced by the intrinsic factors of a sample but also extrinsic factors such as sample preparation methodology. It is still very difficult to prepare polycrystalline multifunctional materials which have all the optimum desired properties. Hence, it is very important to have proper knowledge about the homogeneity, microstructure, preparation and control of chemical composition for synthesizing the desired multifunctional material.

This chapter contains a brief description about the various techniques for the preparation of ceramic samples with their advantages and disadvantages. The sample preparatory method used in the present work will also be discussed.

3.1 Sample Preparation Techniques

In the literature, there are various methods available for the synthesis of ceramic samples. There are basically two approaches for sample preparation [2].

1. The chemical method.
2. The mechanical method.

The mechanical methods can be divided into two types,

- a. High energy ball milling.
- b. Solid state reaction technique or mixed oxide process.

Similarly, the following chemical methods are generally used for the synthesis of the ceramics material.

- a. Auto-combustion technique.
- b. Sol-gel method.
- c. Hydrothermal method.
- d. Co-precipitation technique, etc.

Both the mechanical and chemical methods have some advantages and disadvantages. The advantages of the mechanical methods include large-scale production of bulk ceramic powder at low cost and comparatively easy adaptability. However, in the conventional solid-state reaction method the particles are being coarse due to the high temperature and heating for long time [2]. Chemical methods are generally used to prepare fine powder with improved homogeneity and densification. The chemical precursors used in the sample preparation process can simply be refined to enhance the purity of the desired composition. It is also easy to control the stoichiometry and particle size with less processing time. However, the chemical techniques are generally complex than the conventional solid-state route and the large-scale production is sometimes difficult.

In this thesis, the most economical and comparatively simple mixed oxide process (conventional solid-state reaction technique) is used for preparing the different compositions of ZnO based ceramics.

3.2 Standard Solid State Reaction Route

The solid-state reaction method is the most widely used technique for the synthesis of polycrystalline materials from a mixture of solid starting materials. It is a direct reaction technique between the starting raw materials (usually powders). At room temperature, solids do not react together. High temperature (often 800 to 1600 °C) is required to take place the reaction at an appreciable rate. There are several factors on which the rate of reaction and feasibility depend including structural

properties of the reactants, reaction conditions, surface area of the solids, reactivity of solids, and change of the thermodynamic free energy associated with the reaction [3, 4]. Solid-state reaction is generally slow because during the reaction process a large number of bonds break and the ions migrate through a solid unlike gas phase and solution reactions [2]. Diffusion acts as the limiting factor in solid state reaction. So by controlling the diffusion of the cations through the product layer the solid state reaction rate can be controlled. The reaction takes place more quickly with the increase of temperature and reaction does not take place until the reaction temperature reaches at least two third of the melting point of one of the reactants [2]. The basic steps involved in the solid state reaction method are discussed below.

3.2.1 Reagents

Reagents are the solid reactants which are used to prepare a solid sample. The selected raw materials are first weighed out according to the stoichiometry of the compound. In this case, the impurity and moisture content should be taken into consideration. Before weighing the reactants should be dried thoroughly.

3.2.2 Mixing

After weighing the required amount of raw materials, they are mechanically mixed and then grind to control the particle size and for making the mixture homogeneous. For this purpose milling operation is carried out which can reduce the particle size to 1-10 μm range [5]. For mixing small amount of reactants, generally an agate mortar and pestle are used as shown in Fig. 3.1. Sometimes volatile organic liquid (acetone or alcohol) is used to make the mixture more homogeneous. During the mixing and grinding process the organic liquid volatilizes gradually and evaporates completely after 10 to 15 minutes. Ball milling process is adopted when the quantity of raw materials are much larger than 20 to 25 gm. Since increase in surface area may increase the reaction rate, fine grained materials should be used.



Fig. 3.1: Balance, mortar and pestle.

3.2.3 Calcination

Next step is the solid state reaction between the constituents of the raw materials at suitable high temperature. This process is known as firing or calcinations. Calcination is typically a chemical reaction technique during which either complete or partial phase of the material is formed. During the calcinations process the unwanted gases and impurities are removed from the desired composition. It also helps in homogenization of the powder sample and reducing the shrinkage. Calcination causes the constituents to interact by inter diffusion of their ions and resulting in a homogeneous body. The control over the stoichiometry is necessary during the calcinations process and for it, volatile constituents should be compensated. This thermal treatment process can be carried out in the absence or limited supply of air. Calcination reactions occur at or above the thermal decomposition temperature of the constituent starting materials. This reaction takes place at temperature below the melting points of the raw materials [6]. The calcinations temperature is the temperature at which the standard Gibbs free energy for a particular calcination reaction is equal to zero [7]. The calcination temperature for a desired composition can be selected from the thermogravimetric analysis (TGA), differential thermal analysis (DTA) and the differential thermogravimetric analysis (DTG). In general, the calcination of raw materials is involved with four physical processes [2].

1. Linear expansion of the particles (< 400 °C)
2. Solid phase reaction (400 to 750 °C)

3. Contraction of product (750 to 850 °C)
4. Grain growth (> 850 °C)

A programmable furnace is typically used for the high temperature heat treatment. Crucible or boat can be used as container of sample. However, it is important to choose a suitable container material. The container material should be chemically inert to the reactants under the heating conditions used. A typical diagram of the container of sample and a programmable furnace are illustrated in Fig. 3.2.

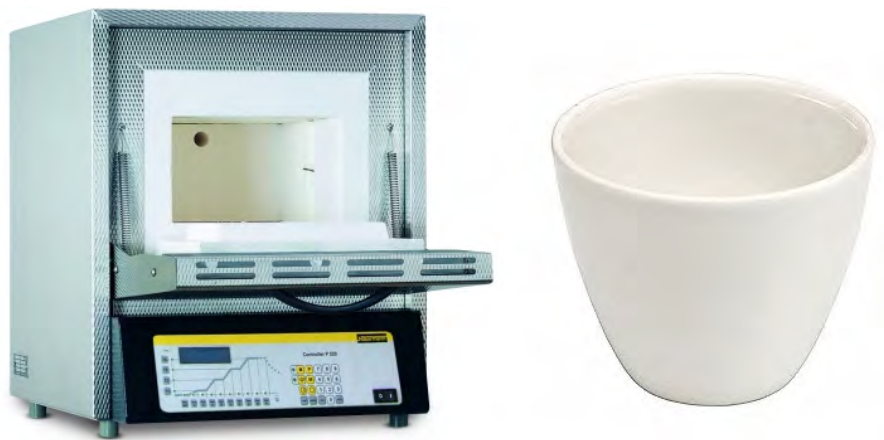


Fig. 3.2: Typical diagram of a crucible and a programmable electric furnace.

3.2.4 Green body preparation

Before further shaping the calcined powder is grind or ball milled again for few hours. Usually, the calcined powder is mixed with an organic binder (Polyvinyl alcohol-PVA) for making the sample more strengthened so that handling of the sample between the shaping and sintering process may not be difficult. It is very important that to choose such a reagent as binder which is removable from the pressed sample after sintering without any disruptive effect. There are various methods available for shaping powder sample. These are,

1. Uniaxial pressing
2. Isostatic pressing

3. Extrusion
4. Calendering
5. Jigging
6. Band casting
7. Silk screening
8. Slip casting
9. Injection moulding

However, in the present work uniaxial pressing technique is used among these different shaping methods.

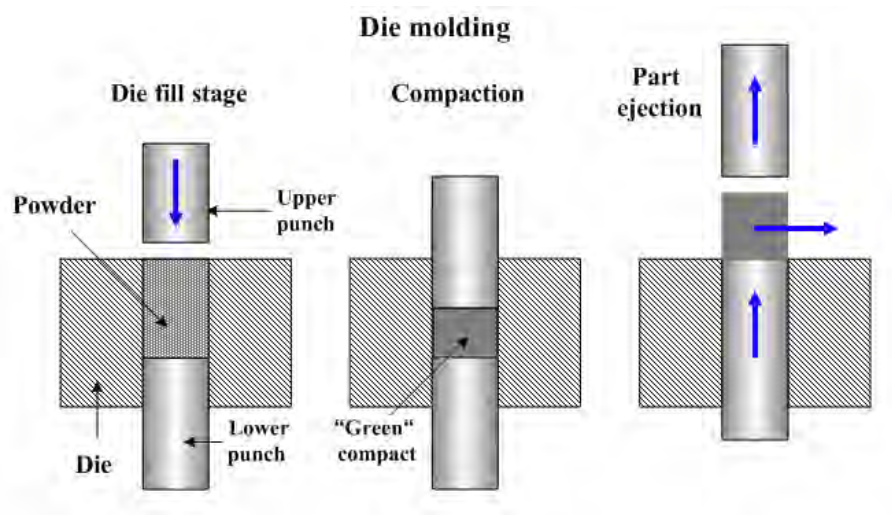


Fig. 3.3: Schematic diagram of uniaxial pressing technique [8].

Uniaxial pressing is a sample shaping method which compresses calcined powder samples by applying pressure in a single axial direction. Thus this process does not ensure maximum uniformity of the density and microstructure as the isostatic pressing. The process is illustrated in Fig. 3.3. A rigid die is used for uniaxial pressing. Generally, 4000 to 8000 psi pressure is applied by using a Hydraulic press [Fig. 3.4] to prepare the green body.



Fig. 3.4: Typical diagram of a Hydraulic press [9].

3.2.5 Sintering

Sintering is the process of compacting and forming a solid mass of material by heat or pressure without melting it to the point of liquefaction. It is the process in which the green compacts are generally consolidated into strong and dense polycrystalline aggregates [2]. During sintering at an appreciable temperature, the atomic motion is more violent and the area between grains in contact increases due to the thermal expansion of the grains and finally only one interface between two grains remains. This corresponds to a state with much lower surface energy. In this state, the atoms on the grain surfaces are affected by neighboring atoms in all directions, which results in densified ceramic [6]. Sintering is effective when the process reduces the porosity and enhances properties such as strength, electrical conductivity, translucency, thermal conductivity etc.

Coble and Burke derived an empirical relationship regarding the rate of grain

growth with sintering time given as follows [11],

$$D = kT^n \quad (3.1)$$

Where D stands for the mean grain diameter, n is about $1/3$, T is the sintering time and k is a temperature dependent parameter. Sintering can be divided into three stages as shown in Fig. 3.5.

Stage-1: Contact area between particles increases,

Stage-2: Porosity changes from open to close porosity,

Stage-3: Pore volume decreases and grains begin to grow.

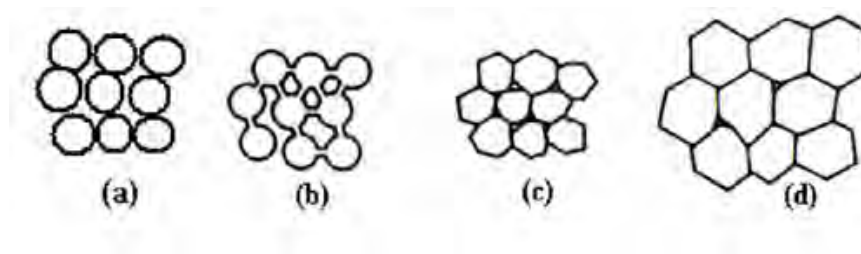


Fig. 3.5: Schematic representation of sintering stages: (a) green body, (b) initial stage, (c) intermediate stage and (d) final stage [12].

At the beginning of the sintering process, at high temperature, the lattice distortion and internal strain are reduced by atomic diffusion. This is known as the recovery process. When the temperature increases further, a recrystallization process occurs through atomic diffusion. During recrystallization, new crystal nuclei form and grow at grain boundaries and in other regions inside the grain with higher free energies. Meanwhile some grains grow by swallowing up other smaller grains. In the recrystallization stage grain growth is usually realized through the motion of grain boundaries. Generally, higher the sintering temperature, larger the grains would grow, as the grain growth is caused by atomic diffusion, which increases with the increase in sintering temperature. However, if the sintering time is too long or the sintering temperature is so high, the density of the sample may be reduced due to the formation of larger grains.

3.2.6 Etching

Etching is a technique for exposing the microscopic features of a sample. It is a process of revealing the microstructure of materials. There are several etching techniques, such as [10]-

1. Thermal etching.
2. Chemical etching.
3. Electrolytic etching.
4. Plasma etching.
5. Magnetic etching.
6. Molten salt etching.

In this work, thermal etching technique is used. For analyzing the microstructural features of a sample, a metallic sample must be polished to have a fine mirror like surface. However, the polished surface of a sample looks like a plain white field under a microscope. Hence, for creating a contrast between the elements of the sample's microstructure, thermal etching technique is used. In this case, the etching temperature is few hundred degrees less than that of the sample's sintering temperature. A flow chart for the synthesis of materials by the solid-state reaction route is illustrated in Fig. 3.6.

Now the samples are prepared for different types of characterization and analysis such as XRD, SEM, TEM etc.

3.3 Synthesis of the Present Samples

The conventional solid state reaction technique is used for synthesizing the (Li, Nd) co-doped ZnO ceramics with formula $(\text{Nd}_{0.5}\text{Li}_{0.5})_x\text{Zn}_{1-x}\text{O}$ where, $x = 0.00, 0.01, 0.03, 0.05, \text{ and } 0.10$. ZnO ($\geq 99.99\%$), Li_2CO_3 ($\geq 99.99\%$) and Nd_2O_3 ($\geq 99.99\%$) are taken as the starting materials (raw materials).

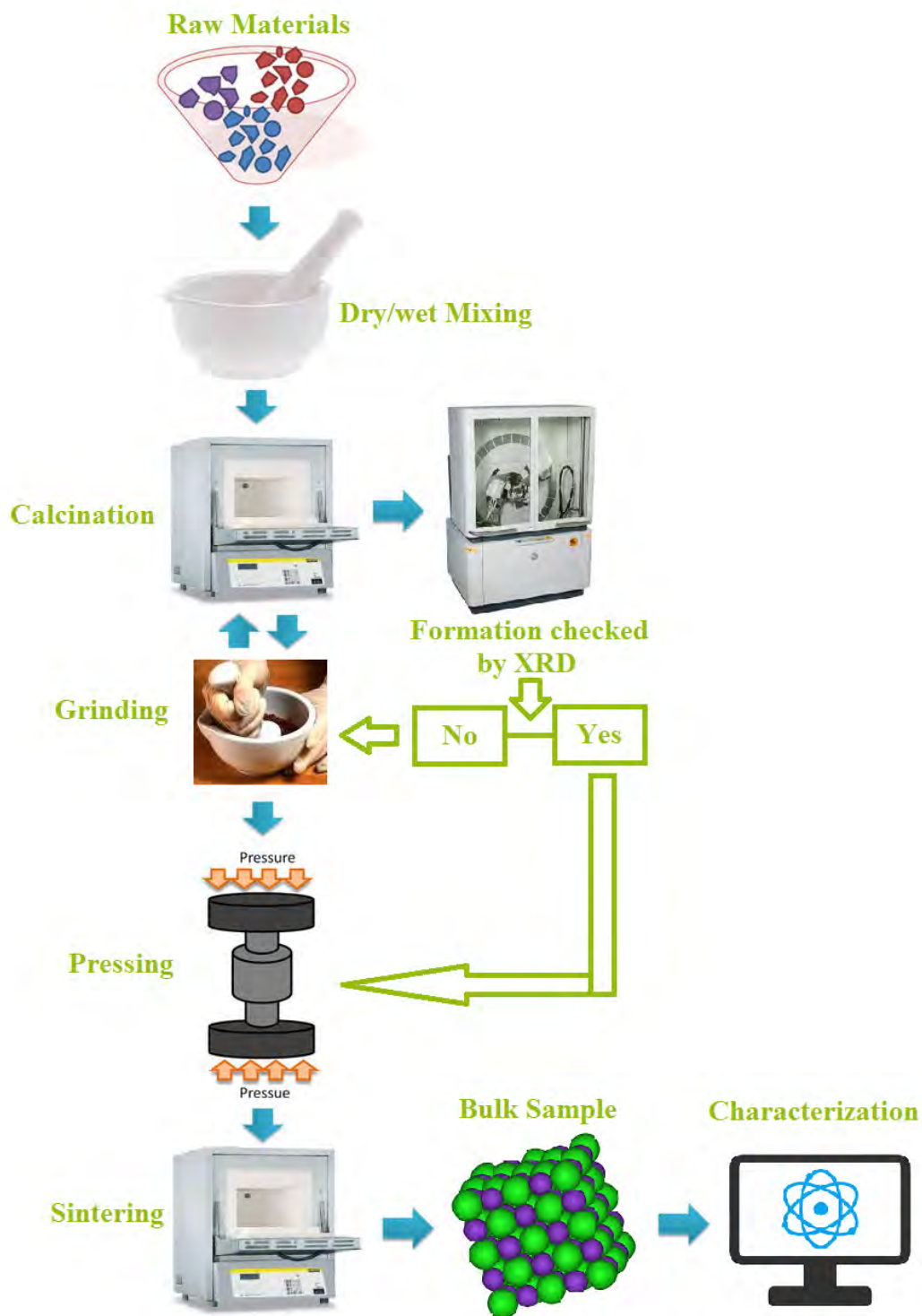


Fig. 3.6: Graphical representation for the synthesis of ceramics samples by the solid-state reaction route.

Stoichiometric amounts of the raw materials (powder form) are properly mixed in an agate mortar by hand milling for about 6 hours. Acetone (Propanone) is used as a

volatile organic liquid for making the mixer more homogeneous. During the mixing and grinding process acetone volatilizes gradually and evaporates completely after 10 to 15 minutes. After grinding and mixing properly, the dried powders are then calcined in an alumina crucible by using a programmable electric furnace at 1073 K for 5 hours in the air with a heating and cooling rate of about 10 and 5 °C/min, respectively. The calcined powder is then re-milled for 4 hours for ensuring proper homogenization. Finally, the dried fine powders are used to prepare the disc shaped pellet and toroid shaped green body (diameter 12-13 mm and thickness 1-1.5 mm) by applying uniaxial pressure of 4000 psi for 1 min through a hydraulic press as shown in Fig. 3.7.



Fig. 3.7: Cylindrical and toroid shaped green body.

Typically 0.90 gm and 0.80 gm fine powder is used to make each pellet and toroid shaped green body, respectively. A small drop of poly vinyl alcohol (PVA) is mixed as a binder for preparing each of the green body. The green samples are then sintered at 1473, 1523, 1573, 1623 and 1648 K in the air for burning out the PVA and densification. The heating and cooling rate in this case is the same as the calcination process. The sintered samples are then polished to remove roughness of the surface and any oxide layer formed during the sintering process.

Bibliography

- [1] Huang, D., Liu, Z., Li, Y., and Liu, Y., "Colossal permittivity and dielectric relaxation of (Li, In) Co-doped ZnO ceramics," *J. Alloy. Compd.*, vol. 698, pp. 200-206, 2017.
- [2] Shah, M. R., *Dielectric properties of alkaline earth ($D = Ba, Sr, Ca$) and rare earth ($T = La, Nd$) substituted polycrystalline $D_{1-x}T_x(Ti_{0.5}Fe_{0.5})O_3$ perovskite*, Ph. D. Thesis, Department of Physics, Bangladesh University of Engineering and Technology, 2013.
- [3] West, A.R. (2014) *Solid state chemistry and its applications*. John Wiley & Sons.
- [4] Gerand, B., Nowogrocki, G., Guenot, J. and Figlarz, M. (1989) *Preparative methods in Solid State Chemistry*. Academic press.
- [5] Moulson, A. J. and Herbert, J. M. (1990) *Electroceramics: Materials, Properties, Applications*. Chapman & Hall, U.K.
- [6] Xu, Y. (1991) *Ferroelectric Materials and Their Applications*. Elsevier Science Pub. Co. New York, USA.
- [7] "Calcination." Wikipedia, Wikimedia Foundation, 18 Nov. 2018, en.wikipedia.org/wiki/Calcination.
- [8] "Materials Engineering." Pitting Corrosion [SubsTech], 22 June 2013, www.substech.com/dokuwiki/doku.php?id=graphite_manufacturing_process.
- [9] "Manual Hydraulic Press." Specac, 2019, www.specac.com/en/products/sample-prep/hydraulic_press/manual/manual.
- [10] Wojes, Ryan. "Find Out How Metallographic Etching Helps Protect Metal Structures." *The Balance Small Business*, The Balance, www.thebalance.com/metallographic-etching-2340003.
- [11] Coble, R. L. and Burke, J. E., "On the reactivity of solids", 4th Int. Symp., 30 May-4 June, Amsterdam, pp. 38-51, 1960.
- [12] Miah, M. J., *Study of Multiferroic Properties of Rare Earth Substituted $xBa_{0.95}Sr_{0.05}TiO_3 - (1-x)BiFe_{0.9}Re_{0.1}O_3$ Perovskite Ceramics*, Ph. D. Thesis, Department of Physics, Bangladesh University of Engineering and Technology, 2016.

CHAPTER 4

EXPERIMENTAL TECHNIQUES

The basic principles of the experimental setup used in this thesis will be introduced in this chapter. A detailed review of how such techniques are used for further improvement of the dielectric as well as magnetic properties of ZnO based ceramics will also be discussed.

4.1 Structural and Morphological Characterization

Phase identification and structural analysis of the investigated samples are carried out by using X-ray diffractometer. Surface morphology of all the samples is investigated by using the Field Emission Scanning Electron Microscope (FESEM). The basic principles of these techniques are discussed in the following sections.

4.1.1 X-ray diffraction

X-ray diffraction (XRD) is considered as a one of the most crucial non-destructive tools for analyzing all kinds of objects ranging from fluids to powders and solids. XRD is an indispensable technique for the characterization of novel materials. XRD methods are widely used to identify crystalline phases of various materials and superior in elucidating the three dimensional atomic structure of crystalline materials. The basic properties and functions of solids largely depend upon the crystal structures. Therefore, X-ray diffraction technique is an essential means in materials research, development and production.

X-ray diffraction is a phenomenon in which the atoms of a crystalline solid, by virtue of their uniform atomic spacing, cause interference pattern of the waves present in an incident beam of X-rays. Crystalline solids are generally periodic or regular arrays of atoms. X-rays can be regarded as waves of electromagnetic radi-

ation. The X-ray waves are scattered primarily by the electrons of the atom. It can be considered just like an ocean wave which is striking a lighthouse producing secondary circular waves originating from the lighthouse [1]. Similarly, an X-ray strikes an electron of an atom and produces spherical secondary waves emanating from the electron. This phenomenon is generally called elastic scattering and the lighthouse/electron is known as the scatterer. A periodic array of scatterers generates a periodic array of spherical waves. Through the destructive interference these waves cancel one another out in most directions. However, in a few specific directions they are added constructively which is determined by Bragg's law [2],

$$2d\sin\theta = n\lambda \quad (4.1)$$

Where d denotes the spacing between diffracting planes, n is an integer, θ is the incident angle, and λ stands for the wavelength of the incident X-ray beam. These specific directions appear as spots on the diffraction pattern which is known as reflections [1]. An example of X-ray diffraction mechanism is shown in Fig. 4.1.

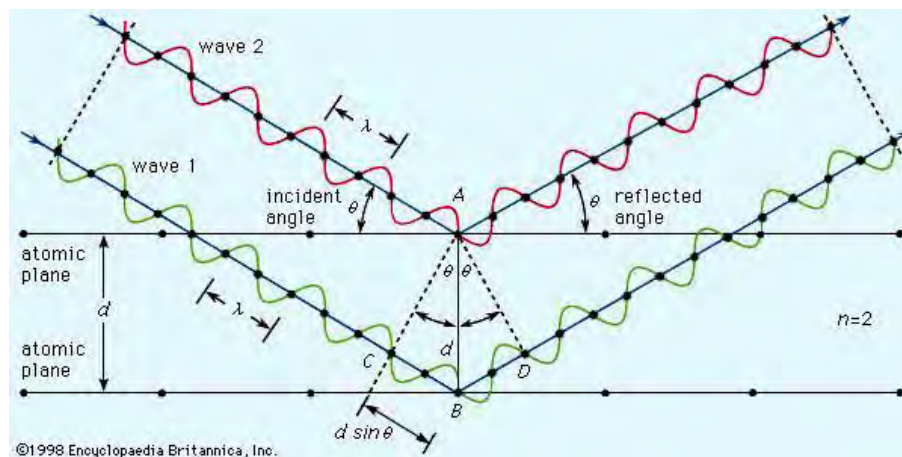


Fig. 4.1: Graphical representation of X-ray diffraction technique [3].

For producing significant diffraction, the wavelength of the striking wave should be similar in size with the spacing between the scatterers. X-rays are typically used to generate the diffraction pattern because the wavelength of X-ray is typically the same order of magnitude (1-100 angstroms) with the spacing between planes in the

crystalline solid [1]. According to the Bragg's law, diffraction is only possible when $\lambda \leq 2d$ [2]. This is the reason why visible light can not be used to determine the crystal structure of a material. For cubic structure d is given by,

$$\frac{1}{d^2} = \frac{h^2 + k^2 + l^2}{a^2} \quad (4.2)$$

Combining the two equations a relation can be obtained which defines the diffraction angle for any set of planes for a given λ if the following condition is satisfied,

$$\sin^2\theta = \frac{\lambda^2(h^2 + k^2 + l^2)}{4a^2} \quad (4.3)$$

Similarly, we can have relations for other crystal systems such as tetragonal, orthorhombic etc.

In this thesis, the crystal structure and phase purity of the studied compositions are investigated by using an advanced X-ray diffractometer (Model-Philips PANalytical X'PERT-PRO, Cu-K α is used as target with incident wavelength, $\lambda = 1.540598 \text{ \AA}$). A schematic diagram for X-ray powder diffraction (XRD) experiment is shown in Fig. 4.2. A typical X-ray diffractometer is shown in Fig. 4.3.

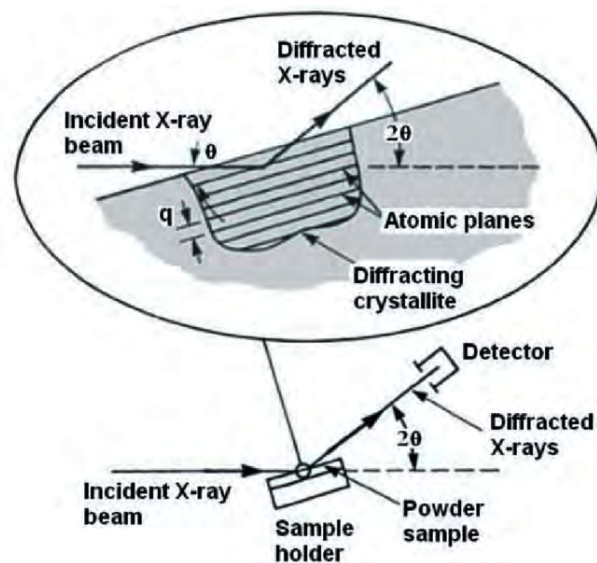


Fig. 4.2: Schematic diagram for a typical X-ray powder diffraction experiment [4].



Fig. 4.3: A typical X-ray diffractometer used for XRD [5].

The average crystallite size of the selected compositions is estimated from the width of the XRD peak by using the Scherrer equation given as follows,

$$D = \frac{0.9\lambda}{\beta \cos\theta} \quad (4.4)$$

where D denotes the average crystallite size, λ is the wavelength of X-ray, θ is the angle of the incident beam and β is the line broadening at half the maximum intensity (FWHM), after subtracting the instrumental line broadening, in radians. From the XRD data the lattice parameter of a cubic structural sample can be calculated by using Eq. (4.2). However, for a hexagonal structure the following equation is used.

$$\frac{1}{d^2} = \frac{4}{3} \left(\frac{h^2 + hk + k^2}{a^2} \right) + \frac{l^2}{c^2} \quad (4.5)$$

Now for determining the precise lattice parameter of a sample the Nelson-Riley method is used [6]. The Nelson-Riley function is given by,

$$F(\theta) = \frac{1}{2} \left[\frac{\cos^2\theta}{\sin\theta} + \frac{\cos^2\theta}{\theta} \right] \quad (4.6)$$

The values of lattice constant of all the peaks for a sample are plotted against $F(\theta)$. Then by using a least square fit method exact lattice parameter can be determined. The point where the least square fit straight line cut the y-axis (i.e. at $F(\theta) = 0$) is the actual lattice parameter of the sample.

Rietveld refinement is another method for the structural characterization of crystalline materials. The pattern resulted from the X-ray or neutron diffraction of powder sample characterized by reflections (peaks in intensity) at certain positions can be refined by using the Rietveld refinement technique. We can have many structural aspects of a material by the height, width and position of those reflections (peaks) of the XRD pattern. This method uses a least square approach to refine a theoretical line profile until it matches the measured profile [7]. In this thesis, the Rietveld refinement technique is used for the analysis of XRD data of the selected compositions implemented within FULLPROF program [8].

4.1.2 Microstructural studies by SEM/FESEM

The surface morphology of the sintered samples can be investigated by using a high resolution optical microscope, Scanning Electron Microscope (SEM), Field Emission Scanning Electron Microscope (FESEM) and Transmission Electron Microscope (TEM). Scanning Electron Microscopy (SEM) has been a powerful and popular tool for materials surface characterization. Electrons are used in electron microscope just like as the light or optical microscope which uses visible light for imaging. A scanning electron microscope (SEM) is a microstructure analysis tool which generates image of a sample by scanning the surface of the sample with a focused beam of electrons. The type of signals generated in SEM varies and can include characteristic X-rays, secondary electrons, and back scattered electrons. Fig. 4.4 shows the type of signals produced in SEM and the area from which they are produced. The most general SEM mode is the detection of secondary electrons that are emitted by the atoms of the sample excited by the incident electron beam. The resolution of SEM image is better than that of a light microscope since the wavelength of electrons is

much smaller than the wavelength of light. The resolution of SEM image can be better than one nanometer [9].

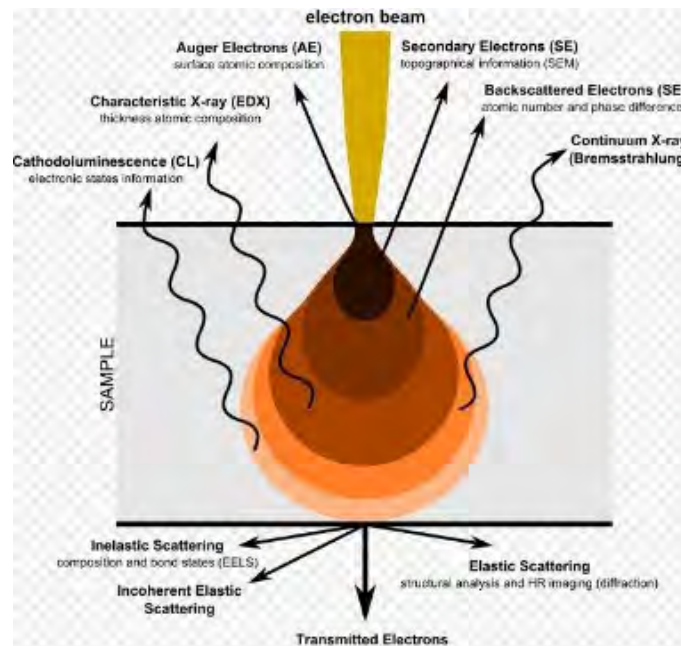


Fig. 4.4: Various types of signals which are generated by electron-matter interactions [11].

In a typical SEM, an electron gun is fitted with a tungsten filament cathode from which an electron beam is emitted. Because of having highest melting point and lowest vapor pressure of all metals tungsten is generally used in thermionic electron gun. The electron beam, which typically has an energy ranging from 0.2 KeV to 40 KeV, is focused by one or two condenser lenses to a spot about 0.4 nm to 5 nm in diameter. The beam passes through pairs of scanning coils or pairs of deflector plates in the electron column, typically in the final lens, which deflect the beam in the x and y axes so that it scans in a raster fashion over a rectangular area of the sample surface [9]. When the primary electron beam interacts with the sample, the electrons lose energy by repeated random scattering and absorption within a teardrop-shaped volume of the specimen known as the interaction volume, which extends from less than 100 nm to approximately 5 μm into the surface. The energy exchange between the sample and electron beam results in the reflection of high-energy electrons by elastic scattering, emission of secondary electrons by inelastic scattering and the emission of electromagnetic radiation, each of which

can be detected by specialized detectors. Electronic amplifier is used to amplify the signals, which are displayed as variations in brightness on a computer monitor. Each pixel of computer video memory is synchronized with the position of the beam on the specimen in the microscope, and the resulting image is, therefore, a distribution map of the intensity of the signal being emitted from the scanned area of the specimen [9]. For SEM, the sample is first made conductive for current. This is done by coating the sample with an extremely thin layer (1.5 - 3.0 nm) of gold or gold-palladium. A schematic diagram of SEM is illustrated in Fig. 4.5.

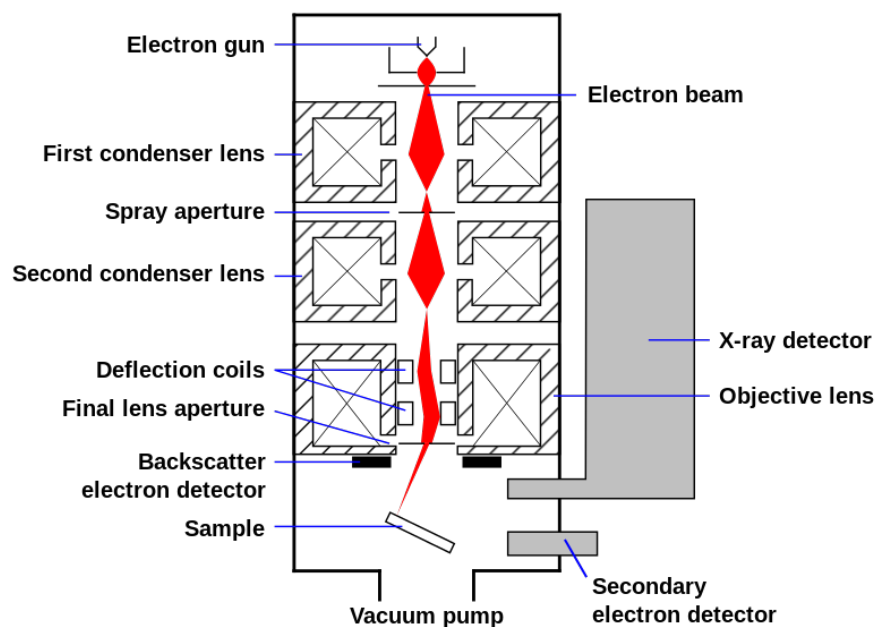


Fig. 4.5: Schematic diagram of scanning electron microscope (SEM) [9].

Field emission scanning electron microscope (FESEM) is another microstructure analysis tool just like as SEM, provides many useful information from the surface of a sample with higher resolution and much greater energy range than that of SEM. As like as SEM electron beam is used for scanning the sample surface. The main difference between a typical SEM and FESEM is the electron beam generation system. A field emission gun is used as a source of electrons in FESEM that produces extremely focused electron beam. For this reason, spatial resolution is improved greatly that enables the function to be performed at very low potentials (0.02-5 KV) [10].

In FESEM, Electrons are emitted from a field emission source. They are accelerated in a high electrical field gradient. Within the high vacuum column these so-called primary electrons are focused and deflected by electronic lenses to produce a narrow scan beam that bombards the object. As a result secondary electrons are emitted from every spot on the object. The velocity and angle of these secondary electrons are related to the surface structure of the sample. A detector catches the secondary electrons and produces an electronic signal which is amplified and transformed to a video scan-image that can be seen on a monitor or to a digital image that can be saved and processed further.

In this thesis, the microstructural analysis of the surface of sintered samples is performed by using the field emission scanning electron microscope (FESEM, JEOL, JSM-7600F) illustrated in Fig. 4.6.



Fig. 4.6: Field emission scanning electron microscope (FESEM) setup.

The average grain size is evaluated by using the linear intercept technique through the relation, $\bar{D} = 1.56\bar{L}$ [12]; where \bar{D} stands for average grain size, and \bar{L} is the average intercept length over a large number of grains as measured on the plane of the sample. For finding out the average intercept length several random

vertical and horizontal lines are drawn on the micrograph of the selected sample. For ensuring the greater accuracy, at least fifty intercept lengths are measured in different places for each sample. Then the numbers of intercept length are counted and measured the length along the line traversed. Finally, the average grain size is evaluated.

4.1.3 Energy-dispersive X-ray spectroscopy

Energy-dispersive X-ray spectroscopy (EDS or EDX) is typically a quantitative analytical technique which is used for the chemical characterization or elemental analysis of a sample. EDX can be used to determine the chemical elements which are present in a given sample. It can also be used to estimate the relative abundance of each element in the specimen. A typical setup for an energy dispersive X-ray fluorescence spectrometer is shown in Fig. 4.7.



Fig. 4.7: A typical setup for EDX/EDS [16].

In this technique, a beam of charged particles such as a beam of X-rays, electrons or protons having high energy is focused into the studied sample. At rest, electrons of an atom in the sample are in the ground state (unexcited). Due to the high energy incident beam an electron in an inner shell (lower energy shell) may be excited and ejected from the shell leaving behind an electron hole at the place where the electron was. Generally, an electron from an outer energy level (higher energy shell) fills the hole. As a result, a characteristic X-ray may be released having

energy equal to the energy difference between the higher energy level and the lower energy level. An energy-dispersive spectrometer is used to measure the number and energy of the emitted X-rays from the sample. Since the energies emitted as the form of X-rays are characteristic of the difference in energy between the two energy levels and of the atomic structure of the emitting element, EDS is used for elemental composition of the sample to be measured [13]. The characteristic X-ray generation process from a specimen is illustrated in Fig. 4.8.

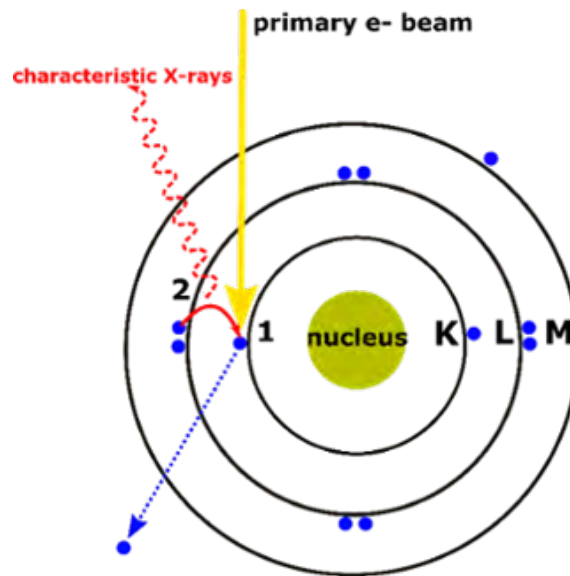


Fig. 4.8: Characteristic X-ray generation process [15].

However, the accuracy of EDX analysis is affected by many factors such as nature of the sample, overlapping X-ray emission peaks etc. Hence it requires generally a quantitative correction approach. These approaches are sometimes referred to as the matrix corrections [14].

EDX analysis can be carried out by using a typical SEM/FESEM. The basic principle involved in this case is similar as described above. In this case high energy electron beam is used to stimulate the electrons of an atom in a specimen. In this thesis, the compositional study of the selected samples are carried out by using the EDX system supplied with the FESEM (JEOL, JSM-7600F) as shown in Fig. 4.6.

4.2 Density and Porosity Calculation

The bulk density of the sintered polished pellet shaped samples can be measured by using the Archimedes method. In this method, at first weight (W_d) of each fully dried pellet is measured by using a precision balance. Then the pellet shaped sample is inserted into the beaker that is filled with distilled water. Then the beaker is placed in a small hanger and the saturated weight (W_s) of the pellet is measured. By using these two weights the density of the pellet shaped specimen can be calculated as follows,

$$\rho_B = \frac{W_d}{W_d - W_s} \times \text{Density of water} \quad (4.7)$$

However, in this thesis the experimental or bulk density of the selected compositions is calculated by using the following relation,

$$\rho_{exp} = \frac{M}{\pi r^2 h} \quad (4.8)$$

Where r is the radius of the pellet shaped sample and h is the thickness of the pellet. The theoretical density of all the pellet shaped specimens is evaluated by using the following relation,

$$\rho_{th} = \frac{ZM}{N_A V} \quad (4.9)$$

Where Z denotes the number of formula unit per unit cell, M is the molecular weight, N_A is defined as the Avogadro's number (6.023×10^{23} /mole), and V is the volume of the unit cell.

The porosity of all the selected compositions is evaluated by using the following expression,

$$P(\%) = \left(\frac{\rho_{th} - \rho_B}{\rho_{th}} \right) \times 100 \quad (4.10)$$

Where ρ_{th} and ρ_B is defined as the theoretical and bulk (experimental) density, respectively.

4.3 Dielectric Properties Measurement

A dielectric material is typically an insulator which is polarized when subjected to an applied electric field. Basically the study of dielectric properties involves the storage and dissipation of electric and magnetic energy in materials. Typically the measurement of dielectric constant involves the measurement of capacitance C_o of a test capacitor with vacuum between its plates. Then using the same capacitor and maintaining the same distance between its plates, the capacitance C with a dielectric material between the plates is measured. The relative permittivity can now be calculated as,

$$\epsilon_r = \frac{C}{C_o} \tag{4.11}$$

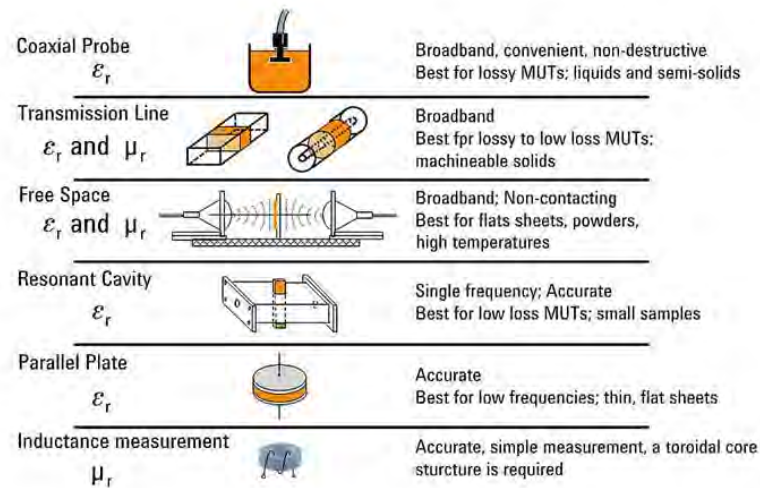


Fig. 4.9: Some techniques for the measurement of dielectric properties [17].

There are several methods available for measuring the dielectric properties of a material. The instruments that are used to employ those techniques have some common parts such as, test fixtures to hold the specimen under investigation,

precise instrumental section and software that makes the whole measurement process easier and display the results. Some key instruments are the network analyzer, impedance analyzer, LCR meters etc. Some techniques for the measurement of dielectric properties are shown in Fig. 4.9.

In the present study, a precision impedance analyzer is used for investigating the dielectric properties of the selected samples. The basic function and working principle of an impedance analyzer is discussed below.

4.3.1 Impedance Analyzer

Impedance analyzer is the most widely used instrument in dielectric measurement on a small scale. It offers an all-in-one approach for the measurement of capacitance. The instrument is used to measure the parasitic resistance and capacitance, and the dielectric constant can be evaluated if the physical dimensions of the parallel plate capacitor are known. A typical diagram of an impedance analyzer is illustrated in Fig. 4.10.

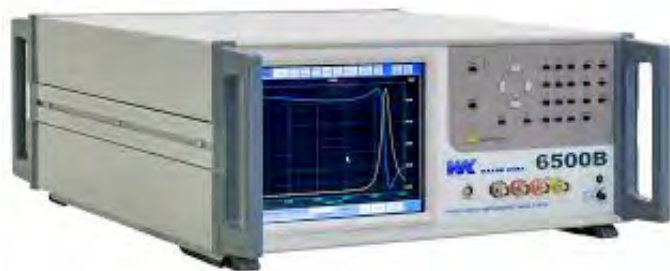


Fig. 4.10: A typical diagram of an impedance analyzer.

4.3.2 Theory and working principle of Impedance Analyzer

By applying a comparatively small sinusoidal signal of amplitude A and frequency f to the capacitor, the displacement current I through the capacitor and the voltage V across the capacitor can be measured by using an Impedance Analyzer and find

the complex impedance Z from the Ohm's Law [24]:

$$\frac{V}{I} = Z = R - jX = Z \angle \theta^\circ \quad (4.12)$$

$$X = \frac{1}{2\pi fC} \quad (4.13)$$

When the capacitance under test is small, the reactance X will be large and possibly affected by a parasitic resistance. On the other hand, if the capacitance under test is typically large then the reactance will be small and likely to be affected by a series resistance. For making the above two equations simple, the admittance Y is found instead of the impedance.

$$\frac{I}{V} = \frac{1}{Z} = Y \quad (4.14)$$

$$Y = G + jB = Y \angle \phi^\circ \quad (4.15)$$

$$|Y| = \sqrt{(G^2 + B^2)} \quad (4.16)$$

$$B = 2\pi fC \quad (4.17)$$

$$R_p = \frac{1}{G} \quad (4.18)$$

In the above equations, B is the susceptance measured in Siemens and G stands for the conductance measured also in Siemens. All of these equations are done inside the Impedance Analyzer and the capacitance C is displayed along with the parasitic parallel resistance R_p . Other useful parameters includes the quality factor Q and the dissipation or loss factor D . These two parameters provide a metric for the ratio of parasitic resistance and capacitance. The quality factor can be expressed as,

$$Q = \frac{1}{D} = \frac{|B|}{G} \quad (4.19)$$

If the capacitor is ideal then no parasitic resistance will present. As a result, the quality factor Q will be infinity. Hence, under this condition low dissipation factor and high quality factor is mostly desirable. The value of the dielectric constant

ε' can easily be evaluated by using the parallel plate capacitor equation when the capacitance is found.

$$\varepsilon' = \frac{Cd}{\varepsilon_o A} \quad (4.20)$$

Where C is the capacitance of the dielectric measured in 'F', d is the thickness of the pellet shaped sample measured in 'm', ε_o is the dielectric permittivity of free space (8.854×10^{-12} F/m) and A is the cross-sectional area of the electrode measured in 'm²'.

4.3.3 Dielectric measurement techniques

In this thesis, the measurements of dynamic (dielectric and electrical) transport properties are performed by using a precision Impedance Analyzer (Wayne Kerr Impedance Analyzer, 6500B) as shown in Fig. 4.11. For electrical and dielectric measurement, the pellet shaped samples are first polished to remove roughness of the surface and contamination of any other oxides on the surface during the sintering process. Both sides of the samples are then painted with conducting silver paste for ensuring the good electrical contacts as illustrated in Fig. 4.12. The real part of dielectric constant of the selected samples is then calculated by using the following relation [18],

$$\varepsilon' = \frac{C}{C_o} \quad (4.21)$$

Where C is the capacitance of the sample measured by the Impedance Analyzer and C_o is the capacitance of the same capacitor without the dielectric material. C_o is derived geometrically as follows,

$$C_o = \frac{\varepsilon_o A}{d} \quad (4.22)$$

Where $A (= \pi r^2)$ is the cross-sectional area of the electrode.



Fig. 4.11: Experimental setup of Wayne Kerr Impedance Analyzer (6500B).



Fig. 4.12: Silver paste painted two probe arrangements on the sintered sample.

The imaginary part of dielectric constant is calculated by using the following relation,

$$\varepsilon'' = \varepsilon' \tan \delta \quad (4.23)$$

Where ' $\tan \delta$ ' is known as the loss tangent or dissipation factor D .

4.3.4 Measurement of ac-conductivity

For understanding the mechanism of conduction the ac-conductivity of all the selected compositions are determined at room temperature for a wide range of fre-

quency. The ac-conductivity can be calculated according to the following relation [25],

$$\sigma_{ac} = \frac{d}{(A \times R_{ac})} \quad (4.24)$$

Where R_{ac} is the ac resistance. The electrical conductivity of most of the materials is expressed as,

$$\sigma(\omega, T) = \sigma_{dc}(T) + \sigma_{ac}(\omega, T) \quad (4.25)$$

Where σ_{dc} defines the dc-conductivity which depends only upon the temperature and σ_{ac} is the ac-conductivity which depends both on the frequency and temperature. The frequency dependent ac-conductivity can be expressed by the empirical formula,

$$\sigma_{ac}(\omega, T) = A\omega^n \quad (4.26)$$

Where A and n both are constants which depend on temperature as well as composition. The constant n is dimensionless and A has units of σ_{ac} . The ac-conductivity of all the sintered samples are evaluated from the dielectric constant data by using the following expression [19],

$$\sigma_{ac} = \varepsilon' \varepsilon_0 \omega \tan \delta \quad (4.27)$$

Where ω ($= 2\pi f$) defines the angular frequency.

4.4 Impedance Spectroscopy

For investigating the electrical properties of materials the complex impedance spectroscopy is a very powerful tool. There are many advantages of this technique. The main advantages include,

- a. The technique involves comparatively simple electrical measurements.

- b. The measurement can be done by using arbitrary electrodes.
- c. By using this technique the resistance of the grain and grain boundaries in most of the polycrystalline materials can be separated simply.
- d. The obtained results can be correlated with various properties including microstructure, composition, defects, chemical reaction, dielectric properties etc.

Typically a Wheatstone-bridge type setup (LCR meter or Impedance Analyzer) is used for ac measurements. In this technique, the resistance R and capacitance C of the specimen are measured and balanced against variable resistors and capacitors. The technique in which the impedance $|Z|$ and the phase difference θ between the voltage and current are measured as a function of frequency for the given specimen is known as impedance spectroscopy. For the analysis of obtained data an impedance plot (a plot between the imaginary part of the impedance $Z'' = |Z|\cos\theta$ and the real part $Z' = |Z|\sin\theta$ on a complex plane) is drawn. Generally an impedance plot with linear scale is used for analyzing the equivalent circuit. Impedance plot of a pure capacitor is a straight line coincides with the imaginary axis and that of pure resistor defines a point on the real axis. The following relation is used to express the impedance of a parallel RC combination [24].

$$Z^* = Z' - jZ''$$

$$\text{or, } Z^* = \frac{R}{(1 + j\omega RC)}$$

After simplification, we get

$$\left(Z' - \frac{R}{2}\right)^2 + (Z'')^2 = \left(\frac{R}{2}\right)^2 \quad (4.28)$$

This equation represents a circle of radius $R/2$ and centre at $(R/2, 0)$. Therefore, a plot between Z' and Z'' will represent a semicircle of radius $R/2$ as shown in Fig. 4.13. This plot is often known as Nyquist plot.

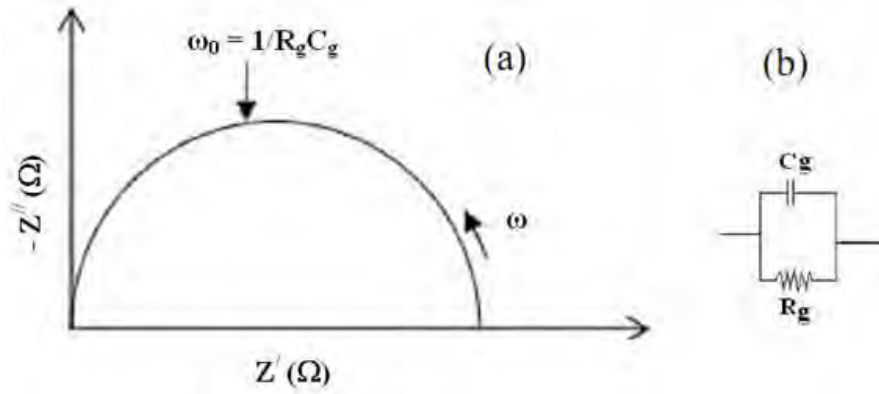


Fig. 4.13: An impedance plot with the corresponding equivalent circuit [22].

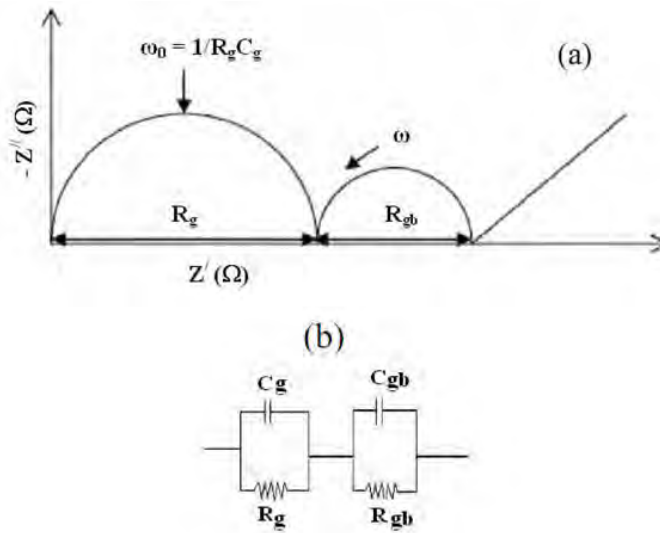


Fig. 4.14: Impedance plot for an ideal polycrystalline sample with the equivalent circuit [22].

The time constant of a simple circuit can be written as,

$$\tau = RC = \frac{1}{\omega_o} \tag{4.29}$$

This is related to the relaxation time of the specimen and the characteristic frequency lies at the peak of the semi-circle. At high frequency, the impedance plot exhibits an arc related to the bulk property of an ideal specimen. Whereas an arc at lower frequency corresponds to the grain boundary behavior and a spike at the lowest frequency is related to the electrode effect. A typical impedance plot and the equivalent circuit for a polycrystalline material are illustrated in Fig. 4.14.

In this thesis, a precision Impedance Analyzer (Wayne Kerr Impedance Analyzer, 6500B) is used for the measurement of real (Z') and imaginary (Z'') part of the complex impedance as a function of frequency at room temperature.

4.5 Modulus Spectroscopy

The study of complex modulus spectroscopy provides crucial information about the distribution parameters of different micro regions in the polycrystalline sample such as grain, grain boundary and electrode interface. This technique is very effective in separating the contributions of different factors such as grain boundary effect, bulk effect and interfaces. It is also useful for separating the components having similar resistance but quite different capacitance. The real and imaginary part of the electric modulus are obtained from the impedance data according to the following relations [23],

$$M' = \frac{\varepsilon'}{(\varepsilon'^2 + \varepsilon''^2)} = \omega C_o Z'' \quad (4.30)$$

$$M'' = \frac{\varepsilon''}{(\varepsilon'^2 + \varepsilon''^2)} = \omega C_o Z' \quad (4.31)$$

4.6 Study of Magnetic Properties

4.6.1 Complex permeability measurement

Measurements of permeability basically correspond to the measurements of the change in self-inductance of a coil in presence of the magnetic core [21]. The behavior of a self-inductance can be explained as follows:

Let us consider an ideal loss less air coil of inductance L_o . On insertion of a magnetic core with permeability μ , the inductance will be μL_o . The complex

impedance Z of this coil [20] can be expressed as follows:

$$Z = R + jX = j\omega L_o\mu = j\omega L_o(\mu' - j\mu'') \quad (4.32)$$

Where the resistive and reactive parts are given by,

$$R = \omega L_o\mu'' \quad (4.33)$$

$$X = \omega L_o\mu' \quad (4.34)$$

Here $\omega (= 2\pi f)$ defines the angular frequency. The permeability can be derived from the complex impedance Z of a coil given by Eq. 4.32. Generally, the core is taken as toroidal shape (Fig. 4.15) to avoid demagnetizing effects.

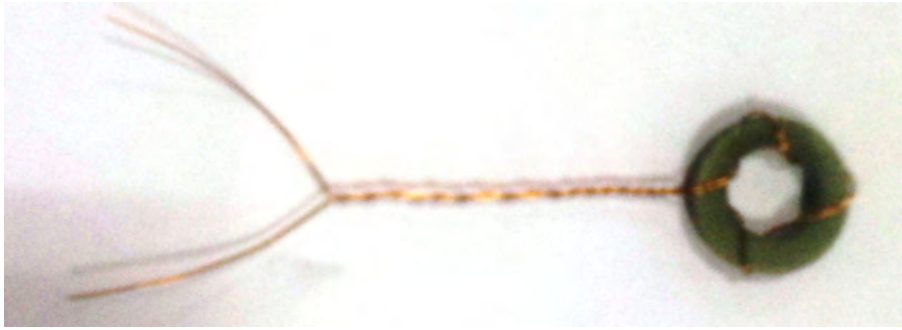


Fig. 4.15: Toroid shaped sample for the measurement of permeability.

The frequency dependent complex permeability of the selected compositions is investigated by using a precision impedance analyzer (Wayne Kerr Impedance Analyzer, 6500B). All the measurements are carried out at room temperature in the frequency range 20 Hz to 120 MHz. The real and imaginary parts of the complex initial permeability are determined by using the following expressions [20],

$$\mu'_i = \frac{L_s}{L_o} \quad (4.35)$$

$$\mu''_i = \mu'_i \tan\delta \quad (4.36)$$

Where L_s defines the self-inductance of the sample core. L_o is the inductance of the

winding coil without the sample core which is derived geometrically by using the following relation,

$$L_o = \frac{\mu_o N^2 S}{\pi \bar{d}} \quad (4.37)$$

Where N is the number of turns of the coil ($N = 4$), S denotes the area of cross section of the toroidal shaped sample and \bar{d} is the mean diameter of the toroidal sample. The cross sectional area of the toroid shaped sample can be calculated as follows,

$$S = d \times h \quad (4.38)$$

where

$$d = \frac{d_2 - d_1}{2}$$

Here d_1 is the inner diameter of the sample core and d_2 is the outer diameter of the sample core. h is the thickness of the sample core.

The mean diameter of the toroid shaped sample can be calculated as,

$$\bar{d} = \frac{d_1 + d_2}{2} \quad (4.39)$$

The relative quality factor (RQF) is evaluated by using the following relation,

$$RQF = \frac{\mu'_i}{\tan \delta} \quad (4.40)$$

Where $\tan \delta$ (*Quality factor*, $Q = 1/\tan \delta$) is the loss factor.

Bibliography

- [1] “X-Ray Crystallography.” *Wikipedia*, Wikimedia Foundation, 9 Jan. 2019, en.wikipedia.org/wiki/X-ray_crystallography.
- [2] Bragg, W.H. and Bragg, W.L., “The reflection of X-rays by crystals,” *Proc. R. Soc. Lond. A*, vol. 88 (605), pp. 428-438, 1913.
- [3] Britannica, The Editors of Encyclopaedia. “Bragg Law.” *Encyclopædia Britannica*, Encyclopædia Britannica, Inc., 30 Dec. 2016, www.britannica.com/science/Bragg-law.
- [4] Brundle, C.R., Evans, C.A. and Wilson, S. (1992) *Encyclopedia of Materials Characterization Butterworth*.
- [5] “Empyrean.” *Prolab Systems*, prolabsystems.com/wp/product/empyrean/.
- [6] Nelson, J.B. and Riley, D.P., “An experimental investigation of extrapolation methods in the derivation of accurate unit-cell dimensions of crystals,” *Proceedings of the Physical Society*, vol. 57 (3), 1945, pp. 160.
- [7] “Rietveld Refinement.” *Wikipedia*, Wikimedia Foundation, 14 Jan. 2018, en.wikipedia.org/wiki/Rietveld_refinement.
- [8] Rodriguez-Carvajal, J., “Fullprof.2k computer program,” version 4.70, 2009.
- [9] “Scanning Electron Microscope.” *Wikipedia*, Wikimedia Foundation, 8 Jan. 2019, en.wikipedia.org/wiki/Scanning_electron_microscope.
- [10] “Field Emission Scanning Electron Microscopy : Electron Microscopy Service.” *UPV*, www.upv.es/entidades/SME/info/859071normali.html
- [11] “SEM: Types of Electrons, Their Detection and the Information They Provide.” *Blog*, blog.phenom-world.com/sem-electrons-detection-provide-information.
- [12] Mendelson, M.I., “Average grain size in polycrystalline ceramics,” *J. Am. Ceram. Soc.*, vol. 52 (8), pp. 443-446, 1969.
- [13] “Energy-Dispersive X-Ray Spectroscopy.” *Wikipedia*, Wikimedia Foundation, 19 Dec. 2018, en.wikipedia.org/wiki/Energy-dispersive_X-ray_spectroscopy.
- [14] Goldstein, J.I., Newbury, D.E., Michael, J.R., Ritchie, N.W., Scott, J.H.J. and Joy, D.C. (2017) *Scanning electron microscopy and X-ray microanalysis*. Springer.
- [15] “EDX Analysis with a Scanning Electron Microscope (SEM): How Does It Work?” *Blog*, blog.phenom-world.com/edx-analysis-scanning-electron-microscope-sem.

- [16] *Chemical Equipment*, www.sunfpu.com/list/cate-11153.htm.
- [17] MA Business Ltd. "Six Techniques for Measuring Dielectric Properties." *New Electronics*, 9 Mar. 2017, www.newelectronics.co.uk/electronics-technology/six-techniques-for-measuring-dielectric-properties/152591/.
- [18] Goldman, A. (2012). *Handbook of modern ferromagnetic materials* (Vol. 505). Springer Science & Business Media.
- [19] Momin, A.A., Parvin, R. and Hossain, A.A., "Structural, morphological and magnetic properties variation of nickel-manganese ferrites with lithium substitution," *J. Magn. Magn. Mater.*, vol. 423, pp. 124-132, 2017.
- [20] Goldman, A. (1999) *Handbook of modern ferromagnetic materials*. Kulwer Acad. Pub, Boston, U.S.A.
- [21] Rafique, M., *Study of the Magnetoelectric Properties of Multiferroic Thin Films and Composites for Device Applications*, Ph. D. Thesis, Department of Physics, COMSATS Institute of Information Technology, 2014.
- [22] Macdonald, J. R. (1987) *Impedance Spectroscopy*. Wiley, New York.
- [23] Rahman, M.A. and Hossain, A.A., "Relaxation mechanism of (x) $\text{Mn}_{0.45}\text{Ni}_{0.05}\text{Zn}_{0.50}\text{Fe}_2\text{O}_4 + (1-x) \text{BaZr}_{0.52}\text{Ti}_{0.48}\text{O}_3$ multiferroic materials," *Phys. Scr.*, vol. 89 (11), pp. 115811, 2014.
- [24] Shah, M. R., *Dielectric properties of alkaline earth (D = Ba, Sr, Ca) and rare earth (T = La, Nd) substituted polycrystalline $D_{1-x}T_x(\text{Ti}_{0.5}\text{Fe}_{0.5})\text{O}_3$ perovskite*, Ph. D. Thesis, Department of Physics, Bangladesh University of Engineering and Technology, 2013.
- [25] Hossen, M. B., *Study of physical, magnetic and transport properties of cations substituted NiCuZn based spinel ferrites*, Ph. D. Thesis, Department of Physics, Bangladesh University of Engineering and Technology, 2015.

CHAPTER 5

THEORETICAL METHODOLOGY

The basic principles involved in the theoretical modeling will be discussed in this chapter. A detailed review of how such theoretical models are used for the verification of experimental results of ZnO based ceramics will also be done.

5.1 First-principles Techniques

Several computational schemes are available for materials modeling. One crucial tool is the use of calculations based on first principles, which are especially useful for materials in the solid state and phenomena that are controlled by properties of materials on the atomic length scale [1]. These calculations are known as *first-principles* or *ab-initio* calculations, which refer to the fact that they are derived from the first principles of quantum mechanics, with no experimental parameters used in the numerical model. While the central equations of quantum mechanics for many-body system are virtually impossible to solve explicitly, approximations and reformulations can be used to obtain a result that converges to the solution of the Schrödinger equation [1]. One important first-principles method for quantum mechanical modeling that uses functionals of the electron density is known as density functional theory (DFT) [1].

With the help of quantum mechanics a many-body system at the atomic level may be described by only the atomic arrangement and electronic structure of the system without any empirical parameters of the system. Here a brief review of the important topics in quantum mechanics will be done to set the stage for what equations must be solved for describing materials.

5.1.1 The Schrödinger equation

The Schrödinger equation is the fundamental equation of physics for describing quantum mechanical behavior. It is also often called the Schrödinger wave equation, and is a partial differential equation that describes how the wavefunction of a physical system evolves over time. Both density functional theory and wave function mechanics start with the formulation of the time-independent Schrödinger equation [2].

$$\hat{H}\psi = E\psi \quad (5.1)$$

Where, ψ is the wave function which contains all the information on the system described, \hat{H} is the Hamiltonian operator which operates on the wave function and presents an output E , the total energy of the system as its eigenvalue. There are several other operators available, for example for spin, electric dipole moments and so on. These can be used to obtain expectation values of physical observables from the wave function.

5.1.2 Born-Oppenheimer Approximation

The Born-Oppenheimer Approximation is the assumption that the motion of atomic nuclei and electrons in a molecule can be separated [3]. In mathematical terms, it allows the wavefunction of a molecule to be broken into its electronic and nuclear (vibrational, rotational) components. Computation of the energy and the wavefunction of an average-size molecule is simplified by the approximation. Since, the motion of the nuclei and electrons can be separated; the electronic and nuclear problems can be solved with independent wave functions. When the nuclei assumed as stationary then the Coulomb interaction between the nuclei is constant. Therefore, the final term can be omitted in solving the Schrödinger equation and added later as a constant to the total energy. This separation of electronic and nuclear problems is known as the Born-Oppenheimer approximation.

5.1.3 Hartree-Fock approximations

The Hartree-Fock (HF) method is a method of approximation for the determination of the wave function and the energy of a quantum many-body system in a stationary state [4]. The Hartree-Fock method often assumes that the exact, N -body wave function of the system can be approximated by a single Slater determinant (in the case where the particles are fermions) or by a single permanent (in the case of bosons) of N spin-orbitals. By invoking the variational method, one can derive a set of N -coupled equations for the N spin orbitals. A solution of these equations yields the Hartree-Fock wave function and energy of the system.

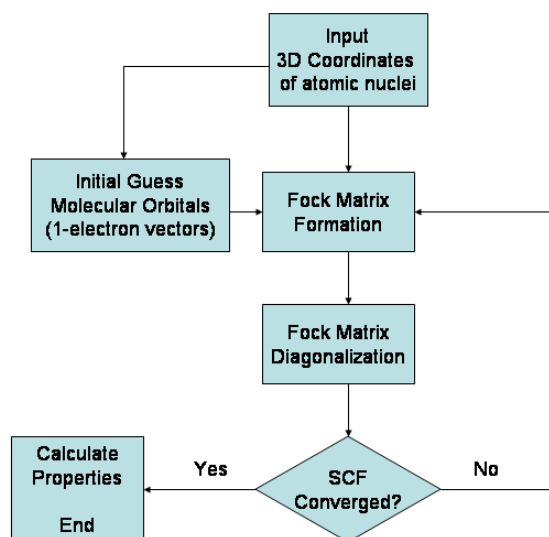


Fig. 5.1: Flowchart representing the Hartree-Fock method [4].

The Hartree-Fock method is also called the **self-consistent field method (SCF)**. In deriving what is now called the Hartree equation as an approximate solution of the Schrödinger equation, Hartree required the final field as computed from the charge distribution to be self-consistent with the assumed initial field. Thus, self-consistency was a requirement of the solution. The solutions to the non-linear Hartree-Fock equations also behave as if each particle is subjected to the mean field created by all other particles and hence the terminology continued. The equations are almost universally solved by means of an iterative method, although the fixed-

point iteration algorithm does not always converge [4]. This solution scheme is not the only one possible and is not an essential feature of the Hartree–Fock method. For both atoms and molecules, the Hartree–Fock solution is the central starting point for most methods that describe the many-electron system more accurately. A general flowchart of the Hartree–Fock method is illustrated in Fig. 5.1.

5.1.4 Density Functional Theory

Density functional theory (DFT) is an alternative type of *ab-initio* method. In physics and chemistry, this method is a quantum mechanical theory used to investigate the electronic structure (principally the ground state) of many body systems, particularly atoms, molecules and the condensed phases and which is the spatially dependent electron density [5]. The success of density functional theory not only encompasses standard bulk materials but also complex materials such as proteins. The main idea of DFT is to describe an interacting system of fermions via its density and not via its many-body wave function. For N electrons in a solid, which obey the Pauli principle and repulse each other via the Coulomb potential, this means that the basic variable of the system depends only on the three spatial coordinates x , y , and z rather than $3N$ degrees of freedom [5]. Density Functional (DF) techniques are based on two theorems, proved by Hohenberg and Khon in 1964 [6], and on a computational scheme proposed by Kohn and Sham (KS) the following years [7]. They showed that the total energy is a functional of the electron density. This means that one does not need to know the complicated many-electron wave function; but only the electron density which is the key quantity in density functional theory.

5.2 Generalized Gradient Approximation

The generalized gradient approximation (GGA) for the exchange correlation functional have led to numerous applications in which density-functional theory (DFT)

provides structures, bond energies, and reaction activation energies in excellent agreement with the most accurate *ab initio* calculations and with the experiment [5]. Many advanced theoretical codes based on density functional theory now use more advanced approximations to improve accuracy for certain physical properties. The DFT calculations in this study have been carried out by using the Generalized Gradient Approximation (GGA). The generalized gradient approximation (GGA) is more efficient than local density approximation. The LDA uses the exchange-correlation energy for the uniform electron gas at every point in the system regardless of the homogeneity of the real charge density. For nonuniform charge densities the exchange-correlation energy can deviate significantly from the uniform result. This deviation can be expressed in terms of the gradient and higher spatial derivatives of the total charge density [1]. The GGA uses the gradient of the charge density to fix this deviation. For systems where the charge density is slowly varying, the GGA has proved to be more efficient than LDA [5]. It is also applicable to the system of inhomogeneous electron gas [1]. Thus it is able to produce the more appropriate results. The purpose of introduction of GGA is to improve the quality of LDA results significantly.

5.3 k-point Sampling

k-points are sampling points in the first Brillouin zone of the material, i.e. the specific region of reciprocal-space which is closest to the origin (0,0,0) (usually called the Gamma point). Electronic states are allowed only at a set of k-points determined by the boundary conditions that apply to the bulk solid. The infinite number of electrons in the periodic solid are accounted for by an infinite number of k-points. However, It is possible to use only a finite number of k-points if these are chosen so as to appropriately sample the reciprocal space [1]. The electronic wave functions at k-points that are very close together will be almost identical. This suggests that the DFT expressions contain a sum over k-points (or, equivalently, an integral over the Brillouin zone) that can be efficiently evaluated using a numerical scheme

that performs summation over a small number of special points in the Brillouin zone. In addition, symmetry considerations suggest that only k-points within the irreducible segment of the Brillouin zone should be taken into account. A number of prescriptions exist for generating such points and corresponding weights to be used in the summation [5]. Using these methods, one can obtain an accurate approximation of the electronic potential and the total energy of an insulator by calculating electronic states at a very small number of k-points. The calculations for metallic systems require a more dense set of k-points to determine the Fermi level accurately. The magnitude of any error in the total energy due to limited k-point sampling can always be reduced by using a denser set of k-points; in much the same way as the convergence with respect to the number of basis set functions is achieved. It is important to achieve high convergence with respect to the k-point sampling when the energies of two systems with different symmetries are compared, for example if one is looking at the relative stabilities of a FCC and an HCP structure. There is no cancellation of errors in this case and both energies have to be absolutely converged. One of the most popular schemes for generating k-points was proposed by **Monkhorst and Pack** [14]. This scheme, which was later modified to include hexagonal systems, produces a uniform grid of k-points along the three axes in reciprocal space.

5.4 Cutoff energy

Since solids are composed of effectively infinite number of electrons, a wave function has to be calculated for each of the infinite number of electrons which will extend over the entire space of the solid and the basis set in which the wave function will be expressed will be infinite. Bloch's theorem uses the periodicity of a crystal to reduce the infinite number of one-electron wave functions to be calculated to simply the number of electrons within the unit cell of the crystal [1]. By the use of this theorem, it is possible to express the wave function of the infinite crystal in terms of wave functions at reciprocal space vectors of a Bravais lattice. The net effect of

Bloch's Theorem therefore has been to change the problem of an infinite number of electrons to one of considering only the number of electrons in the unit cell (or half that number, depending on whether the states are spin-degenerate or not) at a finite number of k-points chosen so as to appropriately sample the Brillouin Zone [1].

Bloch's theorem states that the electronic wavefunctions at each k-point can be expanded in terms of a discrete plane-wave basis set. In principle, an infinite number of plane waves is required for such an expansion. However, the plane waves with a smaller kinetic energy typically have a more important role than those with a very high kinetic energy [1]. Thus, the plane wave basis set can be truncated to include only plane waves that have kinetic energies that are smaller than some particular cutoff energy. The truncation of the basis set at a finite cutoff energy will lead to an error in the computed total energy and its derivatives. It is possible to reduce the magnitude of the error in a systematic way by increasing the value of the cutoff energy. In principle, the cutoff energy should be increased until the calculated total energy converges within the required tolerance.

5.5 Pseudopotential

The pseudopotential can be defined as an attempt to replace the complicated effects of the motion of the core (i.e. non-valence) electrons of an atom and its nucleus with an effective potential, or pseudopotential, so that the Schrödinger equation contains a modified effective potential term instead of the Coulombic potential term for core electrons normally found in the Schrödinger equation [1]. When all of the electrons in a system are explicitly included to perform a calculation with the full Coulombic potential of the nuclei, the computational cost would still be prohibitive using a plane wave basis set. The rapid oscillations of the wavefunctions near to the nucleus, due to the very strong potential in the region and the orthogonality condition between different states, mean that a very large cut-off energy, and hence basis set, would be necessary [5]. Fortunately, the study of chemistry and physics exhibits

that only the valence electrons participate strongly in interactions between atoms and the core electrons of different atoms are almost independent of the environment surrounding the atom. Hence, the energy states of the core electrons can be considered to be fixed and a pseudopotential may be constructed for each atomic species which takes into account the effects of the nucleus and core electrons. The pseudowavefunctions corresponding to this modified potential do not oscillate rapidly as the true wavefunctions. Thus it reduces the number of plane waves required for their representation (Fig. 5.2). The calculations then need only explicitly consider the valence electrons, offering a further saving in effort [5].

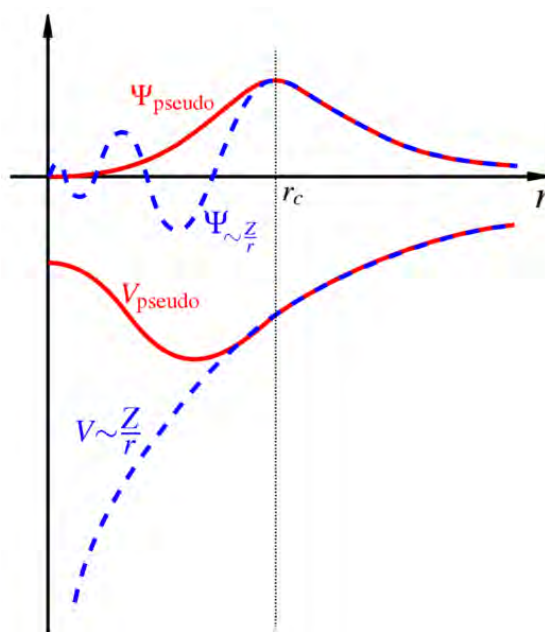


Fig. 5.2: A schematic illustration of the all-electron and pseudized wavefunctions and potentials [1].

There are two types of pseudopotentials:

1. Norm-conserving Pseudopotential
2. Ultra-soft Pseudopotential

Norm conserving pseudopotential allows the calculation to scale linearly with the size of the basis set [1]. In 1990, Vanderbilt [19] proposed a new and radical method for generating much softer pseudopotentials known as ultrasoft pseudopotentials (USP). In this scheme the pseudo-wave-functions are allowed to be as soft as possible

within the core region, so that the cutoff energy can be reduced dramatically. For this reason they are usually called ultrasoft pseudopotentials (USP). In this scheme the electron density is subdivided into (i) a smooth part that extends throughout the unit cell, and (ii) a hard part localized in the core regions. The augmented part appears in the density only, not in the wave functions. This differs from methods like LAPW, where a similar approach is applied to wave functions [1].

5.6 Ground State Energy

For obtaining a stable structure of a 3D periodic system the CASTEP Geometry Optimization task allows one to refine the geometry [1]. An iterative process is used to perform this task in which the cell parameters and the coordinates of the atoms are adjusted provided that the total energy of the system is minimized. This minimized total energy is the ground state energy of the system [1].

In the field of computational chemistry, energy minimization (also called energy optimization or geometry optimization) is the process of finding an arrangement in space of a collection of atoms where, according to some computational model of chemical bonding, the net inter-atomic force on each atom is acceptably close to zero and the position on the potential energy surface is a stationary point [1]. The collection of atoms might be an ion, a single molecule, a transition state, a condensed phase or even a collection of any of these. In this case, quantum mechanics might be the computational model of chemical bonding. The geometry of a set of atoms can be described by a vector of the atom's positions [5]. This could be the set of Cartesian coordinates of the atoms. When considering molecules, this might be so called internal coordinates formed from a set of bond lengths, bond angles and dihedral angles [1].

5.7 Computation of Different Properties

The Density Functional Theory (DFT) dependent plane wave pseudopotential approach is used to perform the theoretical calculations [8]. Cambridge Serial Total Energy Package (CASTEP) is used for executing the desired computations [9]. In order to simulate the doping effect in hexagonal wurtzite ZnO, $2 \times 2 \times 2$ supercell (8 times the unit cell of the pure ZnO) is constructed. The supercell of ZnO contains 32 atoms including 16 Zn atoms and 16 O atoms. For inserting the impurities in pristine ZnO, two Zn atoms are replaced by Li and Nd atoms (substitutional doping) as shown in Fig. 5.3 that produces a doping concentration of 12.5 atom%. Hence the new formula of the doped ZnO can be written as $(\text{Nd}_{0.5}\text{Li}_{0.5})_x\text{Zn}_{1-x}\text{O}$ ($x = 0.125$). Generalized Gradient Approximation (GGA) with the Perdew, Burke and Ernzerhof (PBE) exchange correlation functional is used for evaluating the exchange correlation energy [10]. The plane wave cutoff energy of 500 eV is used to expand the wave function in pure ZnO. The doped system is simulated by using a cutoff energy of 380 eV. The Monkhorst-Pack scheme [14] is used to constitute the K-point sampling of the Brillouin zone. Both the geometry optimization and electronic properties calculations are performed by using $4 \times 4 \times 2$ k-points and $12 \times 12 \times 7$ k-points for doped and pure ZnO, respectively. The number of k-points are enough for good convergence of the pure as well as doped profile. Vanderbilt type ultrasoft pseudopotential is used for describing the electron ion interaction [11]. The geometry optimization of both the pristine and doped system is carried out by the Broyden-Fletcher-Goldfarb-Shanno (BFGS) relaxation scheme [12]. BFGS algorithm is an iterative method for solving unconstrained nonlinear optimization problems. The BFGS method belongs to quasi-Newton methods, a class of hill-climbing optimization techniques that seek a stationary point of a (preferably twice continuously differentiable) function. For such problems, a necessary condition for optimality is that the gradient be zero. However, BFGS has proven to have acceptable performance even for non-smooth optimization instances.

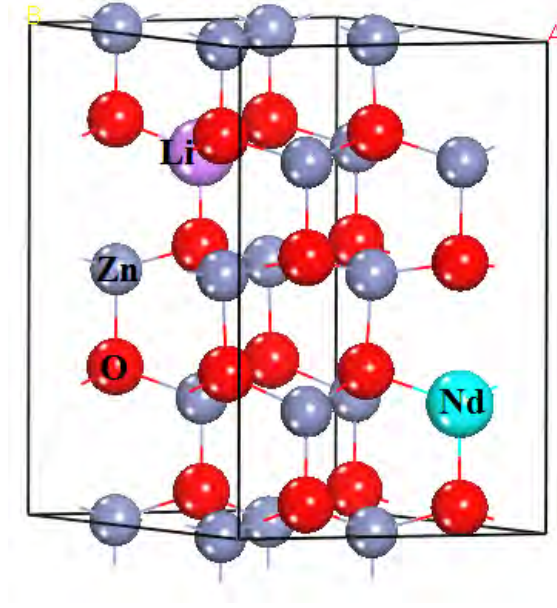


Fig. 5.3: The crystal structure ($2 \times 2 \times 2$ supercell) of Li and Nd co-doped ZnO.

The elastic constants of a material describe its response to an applied stress or, conversely, the stress required to maintain a given deformation. Both stress and strain have three tensile and three shear components, giving six components in total. The linear elastic constants form a 6×6 symmetric matrix, having 27 different components, such that $\sigma_i = C_{ij}\epsilon_j$ for small stresses, σ , and strains, ϵ [20]. Any symmetry present in the structure may make some of these components equal and others may be fixed at zero. Methods to determine the elastic constants from first principles usually involve setting either the *stress* or the *strain* to a finite value, re-optimizing any free parameters and calculating the other property (the strain or stress, respectively). By careful choosing the applied deformation, elastic constants can then be determined. However, applying a given homogeneous deformation (strain) and calculating the resulting stress usually requires far less computational effort, since the unit cell is fixed and does not require optimization. This is the method implemented in CASTEP.

Finite strain theory [13] executed within the CASTEP module is used for calculating the elastic constants of pure and doped ZnO. The maximum strain amplitude is set as 0.003. The polycrystalline elastic parameters are calculated by using the Voigt-Reuss-Hill (VRH) averaging scheme [15] from the computed C_{ij} .

The stiffness tensors for hexagonal crystal are described by six stiffness constants, including the independent components C_{11} , C_{12} , C_{13} , C_{33} and C_{44} , and the non-independent C_{66} ($C_{66} = (C_{11} - C_{12}) / 2$) [16]. For hexagonal structure, the Voigt and Reuss approximation for the bulk and shear moduli are as follows:

$$B_V = \frac{2C_{11} + 2C_{12} + C_{33} + 4C_{13}}{9} \quad (5.2)$$

$$B_R = \frac{C^2}{M} \quad (5.3)$$

$$G_V = \frac{M + 3C_{11} - 3C_{12} + 12C_{44} + 6C_{66}}{30} \quad (5.4)$$

$$G_R = \frac{15}{\left[\frac{18B_V}{C^2} + \frac{6}{(C_{11} - C_{12})} + \frac{6}{C_{44}} + \frac{3}{C_{66}} \right]} \quad (5.5)$$

Where,

$$M = C_{11} + C_{12} + 2C_{33} - 4C_{13}$$

$$C^2 = (C_{11} + C_{12})C_{33} - 2C_{13}^2$$

Hill took an arithmetic mean of B and G given below,

$$B = \frac{1}{2}(B_R + B_V) \quad (5.6)$$

$$G = \frac{1}{2}(G_V + G_R) \quad (5.7)$$

Now, we can calculate the Young's modulus (E), and Poisson's ratio (ν) by using following relations,

$$E = \frac{9GB}{3B + G} \quad (5.8)$$

$$\nu = \frac{3B - 2G}{2(3B + G)} \quad (5.9)$$

The anisotropic characteristics of pure and doped ZnO is estimated by the following

relation [17],

$$A^U = \frac{5G_V}{G_R} + \frac{B_V}{B_R} - 6 \quad (5.10)$$

A^U is zero for completely isotropic materials otherwise the material will be anisotropic.

The frequency dependent dielectric function, $\varepsilon(\omega) = \varepsilon_1(\omega) + i\varepsilon_2(\omega)$, is a key optical quantity to extract all of the optical parameters. The imaginary part $\varepsilon_2(\omega)$ is obtained from the momentum matrix elements between the occupied and the unoccupied electronic states and calculated directly by using the following expression [1].

$$\varepsilon_2(\omega) = \frac{2e^2\pi}{\Omega\varepsilon_0} \sum_{k,v,c} |\langle \psi_k^c | \mathbf{u} \cdot \mathbf{r} | \psi_k^v \rangle|^2 \delta(E_k^c - E_k^v - E) \quad (5.11)$$

where \mathbf{u} is the vector defining the polarization of the incident electric field, ω is the frequency of light, e is the electronic charge and ψ_k^c and ψ_k^v are the conduction and valence band wave functions at k , respectively. The real part $\varepsilon_1(\omega)$ is derived by using the Kramers-Kronig relation given as follows [1],

$$\varepsilon_1(\omega) = 1 + \frac{2}{\pi} P \int_0^\infty \frac{\omega' \varepsilon_2(\omega') d\omega'}{(\omega'^2 - \omega^2)} \quad (5.12)$$

where P implies the principal value of the integral. The remaining optical parameters, such as absorption spectrum, reflectivity and photoconductivity (real part) can be derived from these real and imaginary parts of the dielectric constants. Absorption coefficient $\alpha(\omega)$ can be evaluated as follows [1],

$$\alpha(\omega) = \sqrt{2}\omega \left[\sqrt{\{\varepsilon_1(\omega)\}^2 + \{\varepsilon_2(\omega)\}^2} - \varepsilon_1(\omega) \right]^{\frac{1}{2}} \quad (5.13)$$

The real part of optical conductivity $\sigma(\omega)$ is given as [1],

$$\sigma(\omega) = \frac{\omega\varepsilon_2}{4\pi} \tag{5.14}$$

The reflectivity $R(\omega)$ can be evaluated directly from the Fresnel's formula as follows,

$$R(\omega) = \left| \frac{\sqrt{\varepsilon(\omega)} - 1}{\sqrt{\varepsilon(\omega)} + 1} \right|^2 \tag{5.15}$$

The optical properties of the selected compositions are evaluated by using the CASTEP tool dependent on the standard DFT Kohn-Sham orbitals [18]. A scissor energy of 2.557 eV is applied in the calculation for compensating the gap between the theoretical value (0.743 eV) and experimental value (3.30 eV) of the pure ZnO band gap.

Bibliography

- [1] Hadi, M. A., *First-principles Study of Superconducting MAX Phases*, M.Phil. Thesis, Department of Physics, University of Rajshahi, 2015.
- [2] Schrödinger, E., “Quantisierung als eigenwertproblem,” *Annalen der physik*, vol. 385(13), pp.437-490, 1926.
- [3] “Born–Oppenheimer Approximation.” Wikipedia, Wikimedia Foundation, 15 Jan. 2019, en.wikipedia.org/wiki/Born%E2%80%93Oppenheimer_approximation.
- [4] “Hartree–Fock Method.” Wikipedia, Wikimedia Foundation, 28 June 2018, en.wikipedia.org/wiki/Hartree%E2%80%93Fock_method.
- [5] Rahaman, M. Z., *ThCr₂Si₂-type Ru-based superconductors LaRu₂M₂ (M = P and As): An ab-initio investigation*, B.Sc. Thesis, Department of Physics, Pabna University of Science and Technology, 2017.
- [6] Hohenberg, P. and Kohn, W., “Inhomogeneous electron gas,” *Phys. Rev.*, vol. 136(3B), pp. B864, 1964.
- [7] Kohn, W. and Sham, L.J., “Self-consistent equations including exchange and correlation effects,” *Phys. Rev.*, vol. 140(4A), pp. A1133, 1965.
- [8] Payne, M.C., Teter, M.P., Allan, D.C., Arias, T.A. and Joannopoulos, A.J., “Iterative minimization techniques for ab initio total-energy calculations: molecular dynamics and conjugate gradients,” *Rev. Mod. Phys.*, vol. 64(4), pp. 1045, 1992.
- [9] Segall, M.D., Lindan, P.J., Probert, M.A., Pickard, C.J., Hasnip, P.J., Clark, S.J. and Payne, M.C., “First-principles simulation: ideas, illustrations and the CASTEP code,” *J. Phys. Condens. Matter*, vol. 14(11), pp. 2717, 2002.
- [10] Perdew, J.P., Burke, K. and Ernzerhof, M., “Generalized gradient approximation made simple,” *Phys. Rev. Lett.*, vol. 77(18), pp. 3865, 1996.
- [11] Vanderbilt, D., “Soft self-consistent pseudopotentials in a generalized eigenvalue formalism,” *Phys. Rev. B*, vol. 41(11), pp. 7892, 1990.
- [12] Fischer, T.H. and Almlof, J., “General methods for geometry and wave function optimization,” *J. Phys. Chem.*, vol. 96(24), pp. 9768-9774, 1992.
- [13] Murnaghan, F.D., “Finite deformations of an elastic solid,” *Amer. J. Math.*, vol. 59(2), pp. 235-260, 1937.

- [14] Monkhorst, H.J. and Pack, J.D., "Special points for Brillouin-zone integrations," *Phys. Rev. B*, vol. 13(12), pp. 5188, 1976.
- [15] Hill, R., "The elastic behaviour of a crystalline aggregate," *Proc. Phys. Soc. Section A*, vol. 65(5), pp. 349, 1952.
- [16] Xu, X., Bai, Y., Jin, P., Li, L., Bai, X., Liu, G. and Tang, C., "First-principles calculations on the structural, elastic and electronic properties of a class of ternary carbides: A survey investigation," *Mater. Des.*, vol. 116, pp. 331-339, 2017.
- [17] Ranganathan, S.I. and Ostoja-Starzewski, M., "Universal elastic anisotropy index," *Phys. Rev. Lett.*, vol. 101(5), pp. 055504, 2008.
- [18] CASTEP GUIDE MATERIALS STUDIO 8.0, 2014.
- [19] Vanderbilt, D., "Soft self-consistent pseudopotentials in a generalized eigenvalue formalism," *Phys. Rev. B*, vol. 41(11), pp. 7892, 1990.
- [20] Ashcroft, N.W. and Mermin, N.D. (1976) *Solid State Physics* . Holt Saunders, Philadelphia.

CHAPTER 6

RESULTS AND DISCUSSION

6.1 Structural Analysis

The structural properties of $(\text{Nd}_{0.5}\text{Li}_{0.5})_x\text{Zn}_{1-x}\text{O}$ ($x = 0.00, 0.01, 0.03, 0.05, \text{ and } 0.10$) ceramics are analyzed thoroughly by using X-Ray Diffraction (XRD) techniques. The XRD patterns of the $(\text{Nd}_{0.5}\text{Li}_{0.5})_x\text{Zn}_{1-x}\text{O}$ ceramics sintered at 1623 and 1648 K are illustrated in Fig. 6.1 and Fig. 6.2, respectively. The diffraction peaks of (Li, Nd) co-doped ZnO can be indexed to the wurtzite hexagonal type zinc oxide [JCPDS 89-7102 (ZnO)] having space group $P6_3mc$ (186). In the pristine ZnO bulk material no secondary phases are appeared. However, the XRD patterns of (Li, Nd) co-doped ZnO contains some secondary peaks. The XRD pattern of 1% co-doped samples contains only one impurity peak and with the increase in dopant contents the number of secondary peaks are increased. It is also evident from Figs. 6.1 and 6.2 that the number of secondary peaks are decreased with the increase in sintering temperature. The impurity peaks are appeared due to the presence of Nd_2O_3 phase (JCPDS 83-1346) with hexagonal type structure having space group $P6_3/mmc$ (194) in the desired compositions. It has also been reported previously that Nd doped ZnO contains some extra peaks of Nd_2O_3 phase [1]. The presence of Nd_2O_3 phase in the desired compositions implies that Neodymium (Nd) atoms did not insert completely into the crystalline lattice site resulting inhomogeneous solid solution. However, the shift in peak corresponding to (101) plane as shown in Figs. 6.1(b) and 6.2(b) confirms the partial incorporation of Li and Nd at the Zn site of ZnO ceramics. The reason behind the partial incorporation of Li and Nd at the Zn site can be attributed to the comparatively large ionic radius of Nd compared to Zn. The ionic radius of Zn^{2+} is about 0.074 nm and Nd^{3+} is 0.098 nm.

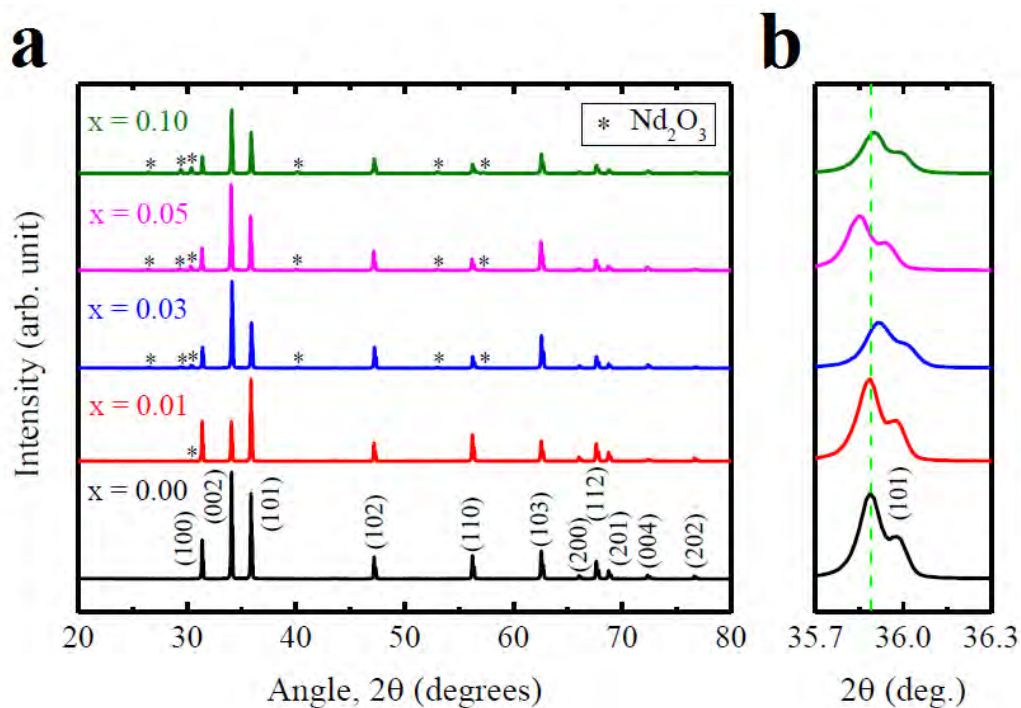


Fig. 6.1: (a) The X-ray diffraction pattern of $(\text{Nd}_{0.5}\text{Li}_{0.5})_x\text{Zn}_{1-x}\text{O}$ ceramics sintered at 1623 K and (b) the shifting of peak corresponding to (101) plane.

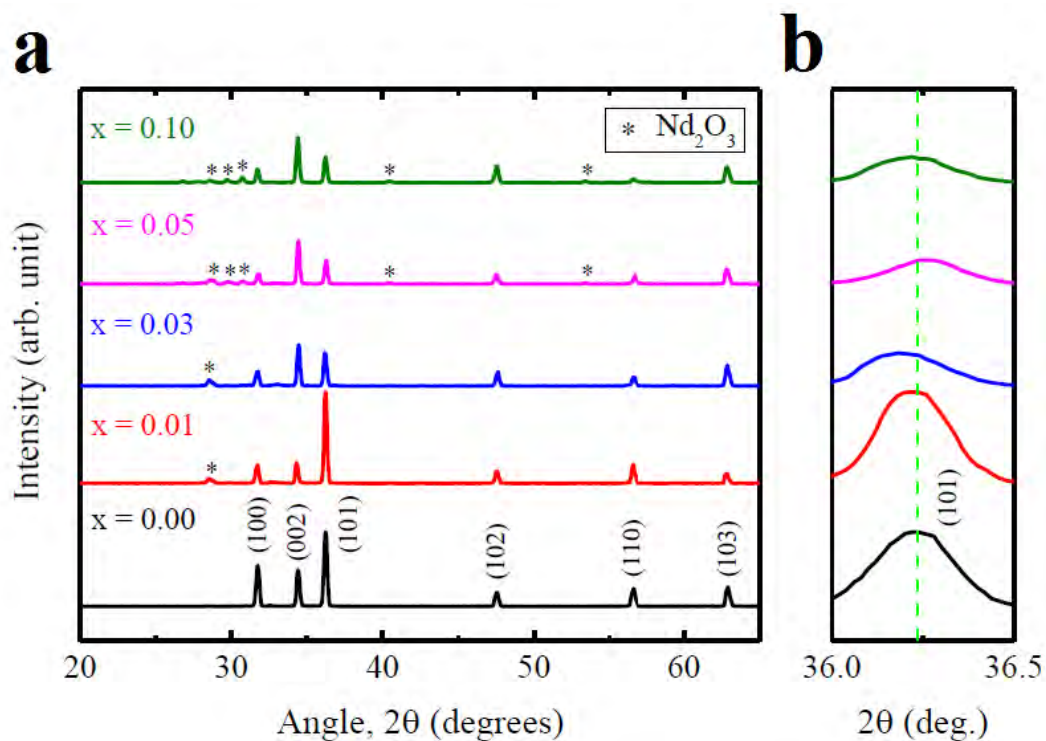


Fig. 6.2: (a) The X-ray diffraction pattern of $(\text{Nd}_{0.5}\text{Li}_{0.5})_x\text{Zn}_{1-x}\text{O}$ ceramics sintered at 1648 K and (b) the shifting of peak corresponding to (101) plane.

Due to this large ionic radius Nd^{3+} encounters some difficulty to replace the Zn^{2+} site of ZnO bulk ceramics.

Generally, the incorporation of Li at Zn site shifts the peak in the higher angle (implying the decrease in lattice parameters as a result of decreasing the interplaner spacing between the lattices) and incorporation of Nd shifts the peak in the lower angle (implying the increase in lattice parameters) [2, 3]. From Figs. 6.1(b) and 6.2(b) it is evident that the shift in peak corresponding to (101) plane is not uniform. The presence of secondary phase and partial incorporation of dopants into the lattice site can be one reason behind these anomalous shift in peaks with composition and sintering temperature. However, shifting in peaks toward higher angle results the enhancement of lattice strain and the strain is minimum when peaks shift toward the lower angle [1].

For further quantitative analysis of the structural parameters Rietveld refinement of the observed X-ray diffraction patterns have been carried out by using FULLPROF package [4]. The refined XRD patterns of the $(\text{Nd}_{0.5}\text{Li}_{0.5})_x\text{Zn}_{1-x}\text{O}$ bulk ceramics sintered at 1623 K are illustrated in Fig. 6.3. It is evident from Fig 6.3 that the calculated patterns show rather good agreement with the experimental XRD patterns. Negligible difference between the experimental and calculated profiles is observed. The value of R-factors are also low indicating rather good refinement of the observed XRD profiles. The refined crystallographic parameters of $(\text{Nd}_{0.5}\text{Li}_{0.5})_x\text{Zn}_{1-x}\text{O}$ ceramics are tabulated in Table 6.1 with the corresponding fitting parameters. The fractional coordinates of the studied compositions are listed in Table 6.2. The major phase of the co-doped samples are observed to be hexagonal structured ZnO with space group $P6_3mc$ (186). The obtained lattice parameters are in good agreement with the other previous studies [3, 5, 6]. However, all the compositions contain an impurity phase except the pristine ZnO. This extra phase is identified as hexagonal structured Nd_2O_3 with space group $P6_3/mmc$ (194) having lattice parameters nearly $a = 0.38317$ nm, $c = 0.60089$ nm and $V = 0.07640$ nm³.

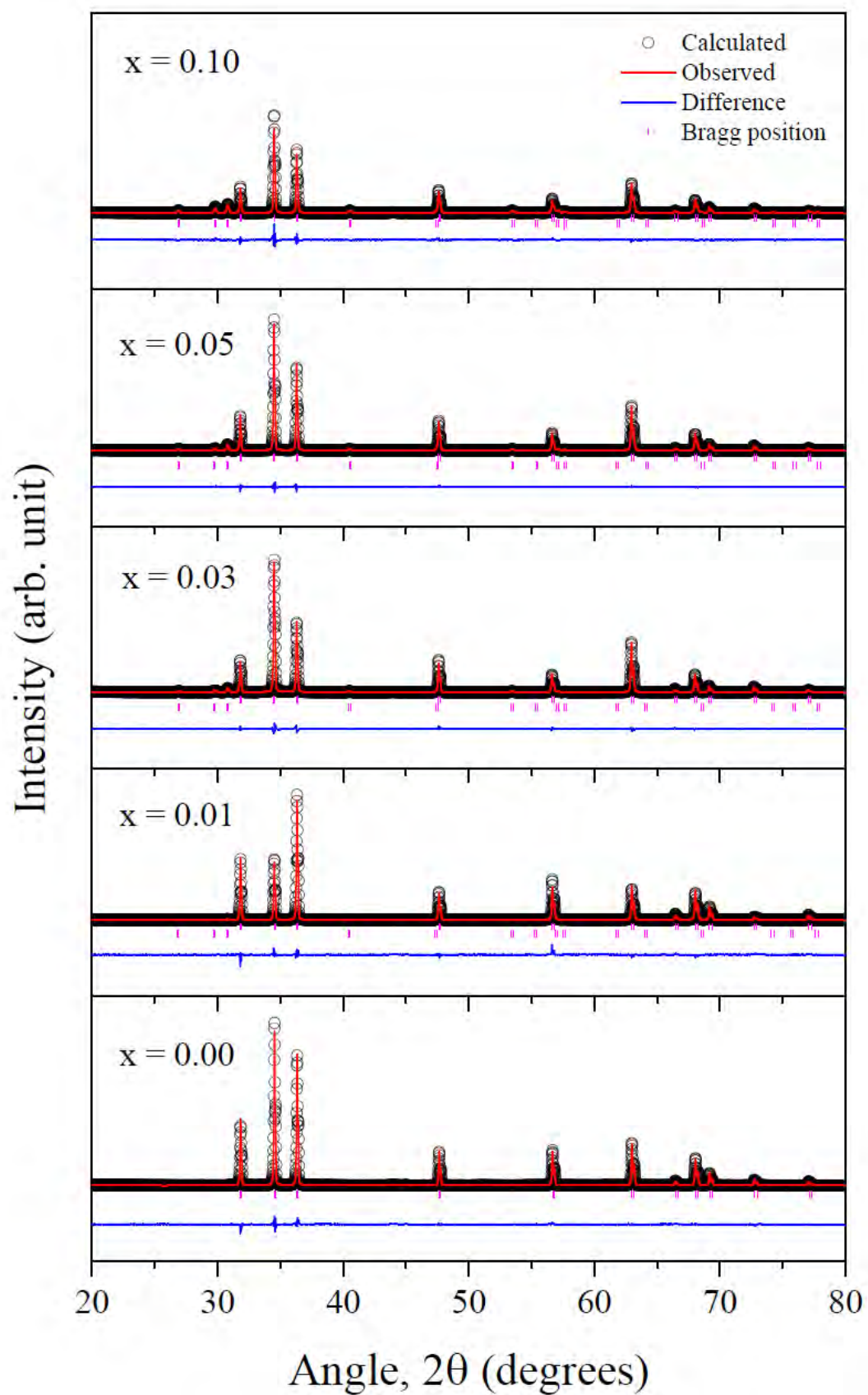


Fig. 6.3: Refined X-ray diffraction profiles of $(\text{Nd}_{0.5}\text{Li}_{0.5})_x\text{Zn}_{1-x}\text{O}$ ceramics sintered at 1623 K.

Table 6.1: Refined crystallographic data of $(\text{Nd}_{0.5}\text{Li}_{0.5})_x\text{Zn}_{1-x}\text{O}$ ceramics.

Parameters	$x = 0.00$	$x = 0.01$	$x = 0.03$	$x = 0.05$	$x = 0.10$
Crystal system	hexagonal				
Space group	$P6_3mc$ (186)				
a (nm)	0.32457	0.32465	0.32487	0.32484	0.32474
c (nm)	0.51940	0.51959	0.51982	0.51986	0.51972
c/a	1.6002	1.6004	1.60008	1.6003	1.6004
α, β, γ (deg.)	90, 90, 120				
V (nm ³)	0.04738	0.04742	0.04751	0.04750	0.04746
Z	2	2	2	2	2
χ^2	4.34	5.31	2.88	2.91	5.12
R_p (%)	5.83	8.34	6.42	6.00	8.85
R_{wp} (%)	8.07	11.0	8.42	8.28	11.5

Table 6.2: Fractional atomic coordinates of $(\text{Nd}_{0.5}\text{Li}_{0.5})_x\text{Zn}_{1-x}\text{O}$ ceramics.

Composition	Atom	x	y	z
$x = 0.00$	Zn	0.33333	0.66667	0.0
	O	0.33333	0.66667	0.39971
$x = 0.01$	Zn	0.33333	0.66667	0.0
	O	0.33333	0.66667	0.39237
$x = 0.03$	Zn	0.33333	0.66667	0.0
	O	0.33333	0.66667	0.38532
$x = 0.05$	Zn	0.33333	0.66667	0.0
	O	0.33333	0.66667	0.38313
$x = 0.10$	Zn	0.33333	0.66667	0.0
	O	0.33333	0.66667	0.39381

Fig. 6.4 illustrates the lattice parameters as a function of doping concentration (x). With the increase in doping content the lattice parameters are found to extend up to 3% doping concentration.

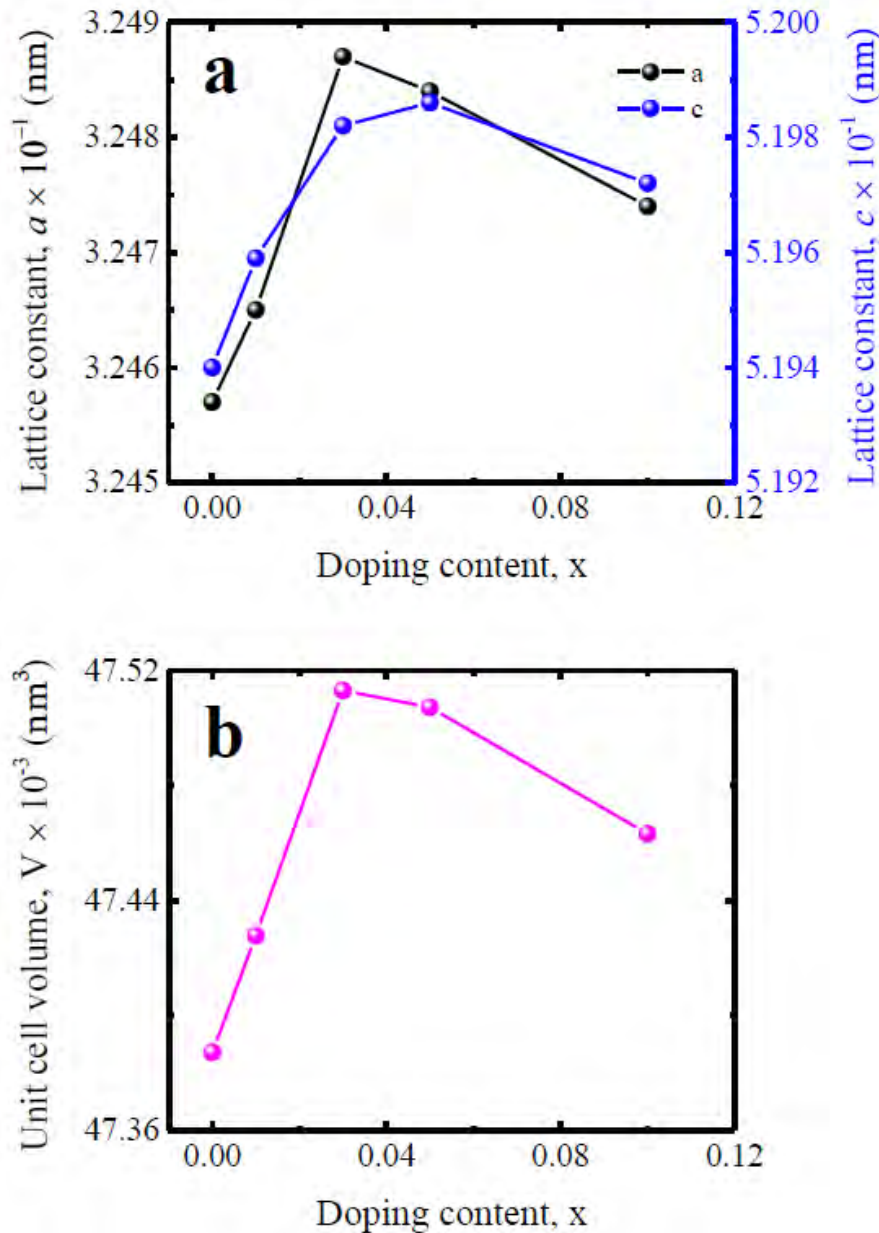


Fig. 6.4: (a) Variation of lattice constants and (b) unit cell volume, as a function of doping concentration of $(\text{Nd}_{0.5}\text{Li}_{0.5})_x\text{Zn}_{1-x}\text{O}$ ceramics.

From 5% doping concentration the lattice parameters begin to decrease. This result can be well explained from the perspective of ionic radius of the constituent ions. According to the valance balance one Nd^{3+} (0.098 nm) and one Li^+ (0.068 nm)

may substitute the 2Zn^{2+} (0.074 nm) ions. Hence the average ionic radius of the dopant ions is nearly 0.083 nm that is comparatively larger than the ionic radius of Zn^{2+} . Due to this reason the lattice parameters are found to extend up to 3% doping concentration. When the doping content exceeds 3%, Nd^{3+} dopant is not incorporated into the lattice site and may appear in the form of Nd_2O_3 (resulting increased number of impurity peaks in the XRD pattern). However, due to the smaller ionic radius of Li^+ , it can still replace Zn^{2+} . Due to this reason the lattice parameters are found to decrease from 5% doping concentration.

The average crystallites size (D) of the studied compositions are evaluated by using the well known Scherrer equation [7, 8], $D = (0.9\lambda)/(\beta\cos\theta)$, where λ is the wavelength of the X-rays, β is the width (full-width at half-maximum) of the X-ray diffraction peak in radians and θ is the Bragg angle in degrees.

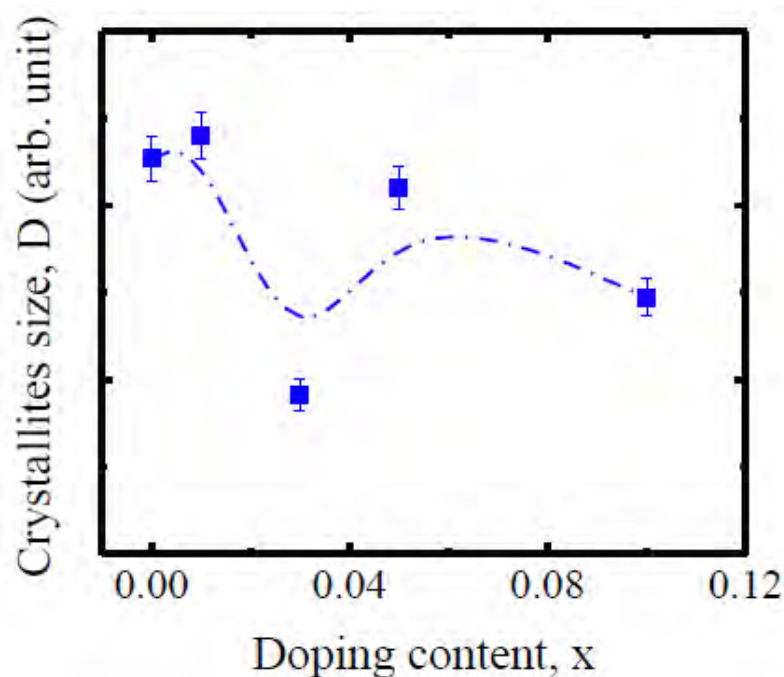


Fig. 6.5: Variation of crystallites size as a function of doping content of $(\text{Nd}_{0.5}\text{Li}_{0.5})_x\text{Zn}_{1-x}\text{O}$ ceramics.

Scherrer's formula is basically an approximation and used to estimate the average particles or crystallites size in the form of powder. This equation is only applicable for nano-scale range particles (100-200 nm) and basically inapplicable for grains

larger than 0.1 to 0.2 μm [8, 9]. However, though this equation does not provide accurate quantitative estimation for larger grains, it can provide good qualitative assessment. The evaluated crystallites size of $(\text{Nd}_{0.5}\text{Li}_{0.5})_x\text{Zn}_{1-x}\text{O}$ ceramics is plotted in Fig. 6.5 as a function of doping concentration. It is evident that on average the crystallites size is decreased with the increase in doping content. Some anomaly occurs due to the presence of secondary phase in the desired compositions.

6.2 Density and Porosity

In polycrystalline materials density plays a crucial role in controlling the dielectric and magnetic properties. The measured bulk density at various sintering temperatures is tabulated in Table 6.3. Sintering temperature dependent bulk density (ρ_B) is also illustrated in Fig. 6.6(a). It is found that ρ_B is enhanced up to 1623 K and begins to decrease after 1623 K. Generally, grain boundaries are grown over the pores by the force generated through the thermal energy during the sintering process. As a result, pore volume is decreased and the samples become more dense with the increase in T_s . Porosity in ceramic sample is generated basically from two sources, intergranular porosity and intragranular porosity [10]. The intergranular porosity depends upon the average grain size. However, some pores are trapped within the ceramic sample due to the very high driving energy at higher sintering temperature. Consequently, ρ_B begins to decrease at very high T_s .

Table 6.3: Bulk density, ρ_B of $(\text{Nd}_{0.5}\text{Li}_{0.5})_x\text{Zn}_{1-x}\text{O}$ ceramics at different sintering temperatures.

x	$\rho_B \times 10^3 \text{ (kg/m}^3\text{)}$				
	1473 K	1523 K	1573 K	1623 K	1648 K
0.00	4.86	4.77	4.91	5.05	5.05
0.01	4.66	4.89	5.09	5.29	5.22
0.03	4.63	4.87	5.12	5.25	5.38
0.05	4.15	4.53	5.07	5.09	5.32
0.10	3.64	4.59	4.83	5.44	5.42

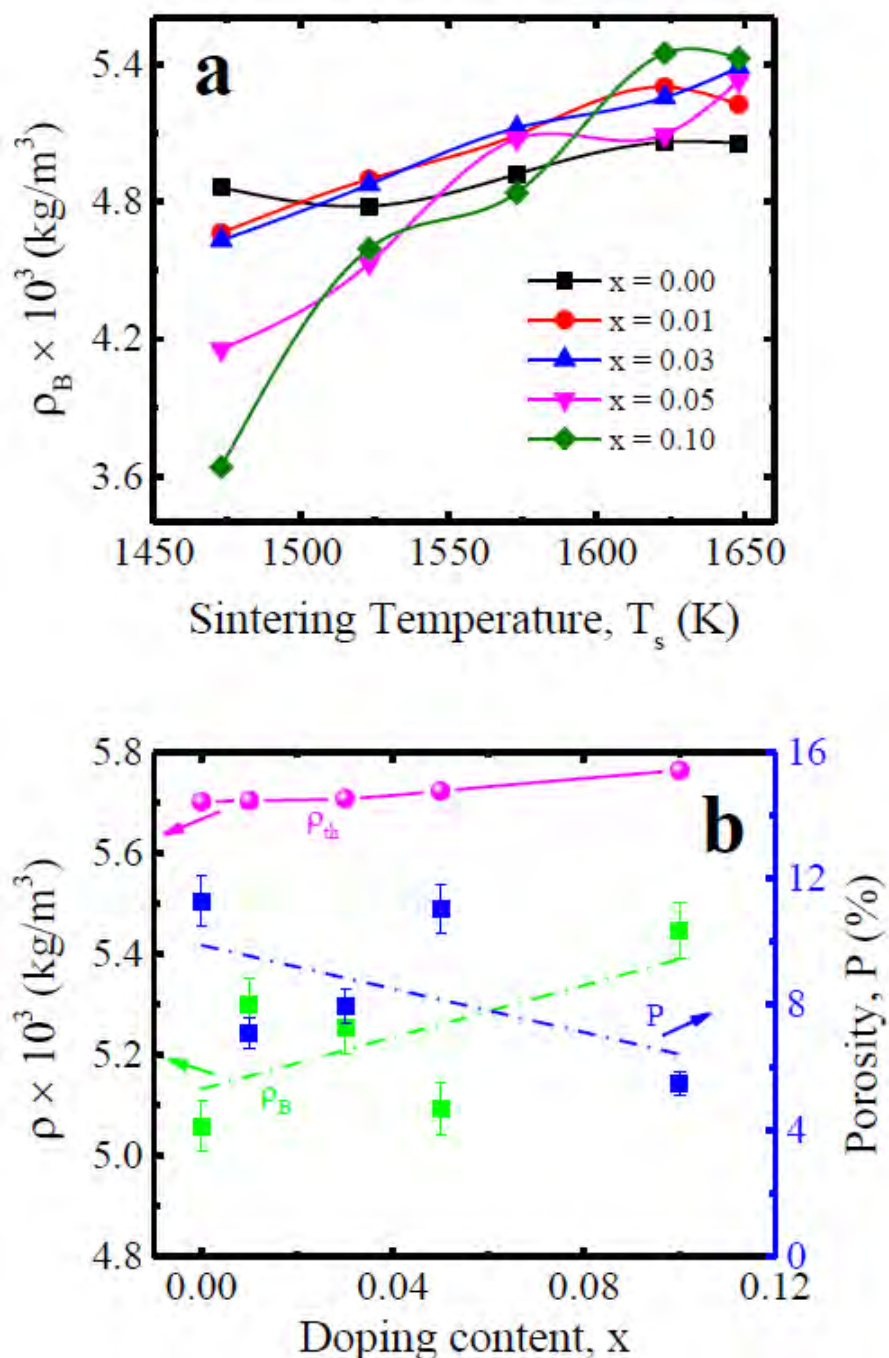


Fig. 6.6: (a) Sintering temperature dependent bulk density of $(\text{Nd}_{0.5}\text{Li}_{0.5})_x\text{Zn}_{1-x}\text{O}$ ceramics. (b) Doping content dependent bulk density, theoretical density and porosity of $(\text{Nd}_{0.5}\text{Li}_{0.5})_x\text{Zn}_{1-x}\text{O}$ ceramics sintered at 1623 K.

The values of doping content dependent bulk density, theoretical density and porosity are listed in Table 6.4. The bulk density, theoretical density and porosity as a function of doping concentration of $(\text{Nd}_{0.5}\text{Li}_{0.5})_x\text{Zn}_{1-x}\text{O}$ ceramics sintered at 1623 K are also plotted in Fig. 6.6(b). It is observed that ρ_B and ρ_{th} is enhanced with

doping content. This phenomenon can be explained in terms of atomic weight of the constituent atoms. The average atomic weight of Li (6.94 amu) and Nd (144.242 amu) is 75.591 amu that is larger than the atomic weight of Zn (65.38 amu). Since Zn is substituted by Li and Nd, it is expected to enhance the density of the studied compositions with the increase in doping content. Diffusion of oxygen ions through the ceramics during the sintering process can also accelerate the densification of the ceramic material. Some deviations occur from the linearly fitted line due to the presence of excess Nd_2O_3 contents that leads to inhomogeneities in the particles. The reason can also be attributed to the very high sintering temperature and sintering time. Since the melting temperature of Li (453.5 K) is very low than the sintering temperature there is possibility for enhancing the sinterability through liquid phase formation [13]. On the other hand, porosity exhibits completely opposite trend. Porosity is decreased with the increase in doping content as the samples become more dense.

Table 6.4: Bulk density, theoretical density and porosity of $(\text{Nd}_{0.5}\text{Li}_{0.5})_x\text{Zn}_{1-x}\text{O}$ ceramics sintered at 1623 K.

x	$\rho_{\text{B}} \times 10^3 \text{ (kg/m}^3\text{)}$	$\rho_{\text{th}} \times 10^3 \text{ (kg/m}^3\text{)}$	P (%)
0.00	5.05	5.7019	11
0.01	5.29	5.7041	7
0.03	5.25	5.7082	8
0.05	5.09	5.7231	11
0.10	5.44	5.7642	6

6.3 Morphological Analysis

The FESEM micrographs of $(\text{Nd}_{0.5}\text{Li}_{0.5})_x\text{Zn}_{1-x}\text{O}$ ceramics sintered at 1623, and 1648 K are demonstrated in Fig. 6.7 and Fig. 6.8, respectively. Fig. 6.9 illustrates the sintering temperature dependent FESEM micrographs. It is evident that substitution of Li and Nd at the Zn site of ZnO ceramics have a significant effect on the

grain size. All the compositions contain randomly aligned non-uniform grains in size and shape due to very high sintering temperature. The distribution of grains is not homogeneous and some agglomeration is appeared in higher doped samples. Non-equivalent size of dopant ions may be the reason behind this agglomeration of grains.

The average grain sizes measured by using the linear intercept technique of the studied compositions are listed in Table 6.5. The doping content dependent grain sizes of $(\text{Nd}_{0.5}\text{Li}_{0.5})_x\text{Zn}_{1-x}\text{O}$ ceramics sintered at 1623, and 1648 K are demonstrated in Fig. 6.10(a). Since the melting temperature of Li (453.5 K) is comparatively low, it leads to enormous grain growth of zinc oxide with a little amount of Nd doping. This is the primary reason behind the enhancement of grain size with 1% doping content. However, the grain size is decreased with further increase in dopant percentage due to the formation of large volume of Nd_2O_3 secondary phase that interrupt the grain growth by pinning the grain boundaries and blocking mass transportation [14].

Table 6.5: Average grain size of $(\text{Nd}_{0.5}\text{Li}_{0.5})_x\text{Zn}_{1-x}\text{O}$ sintered at 1573, 1623, and 1648 K.

x	Grain size (μm)		
	1573 K	1623 K	1648 K
0.00	10.60	5.14	9.87
0.01	5.69	8.56	11.26
0.03	-	6.05	10.99
0.05	-	6.75	-
0.10	-	6.39	8.61

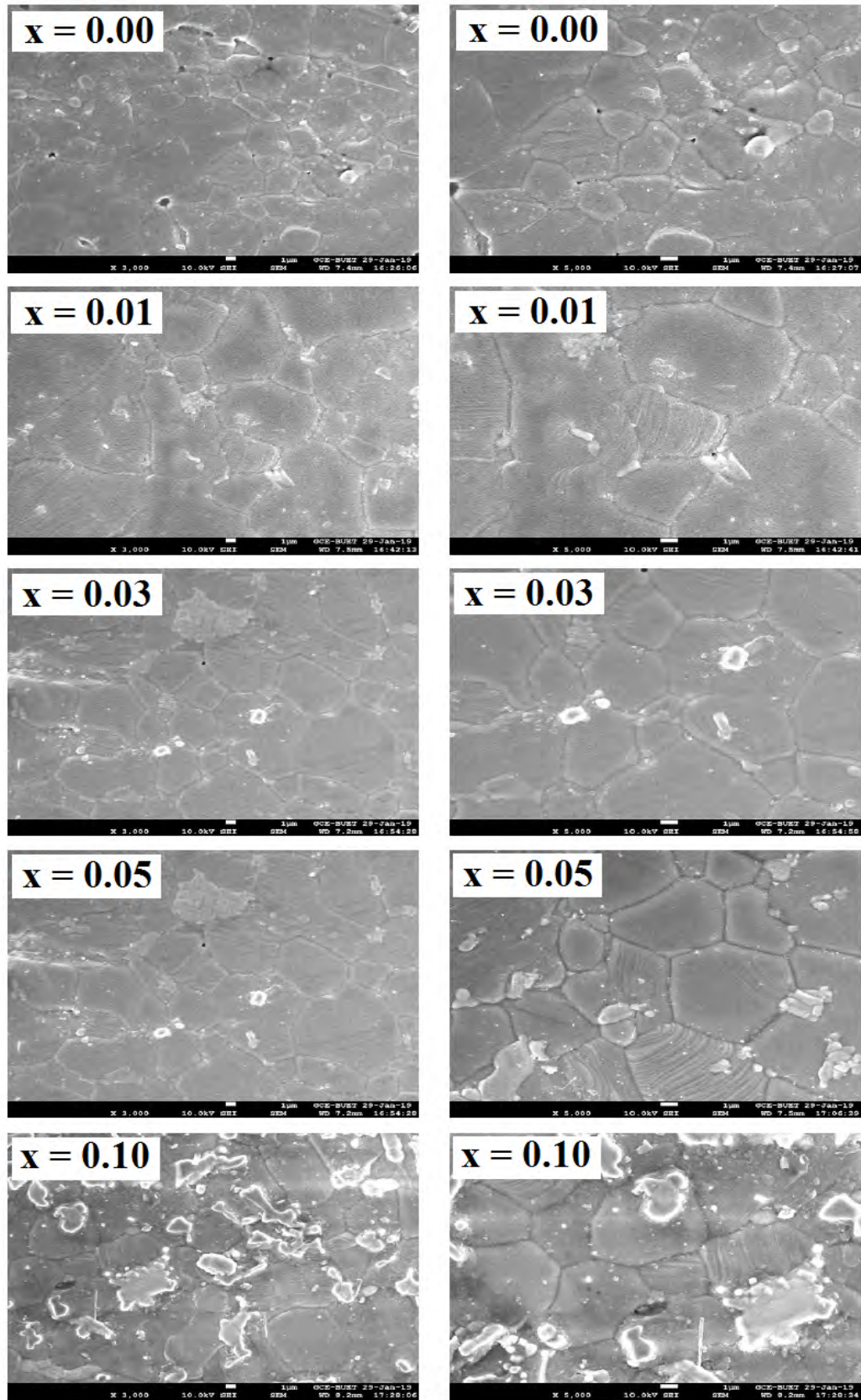


Fig. 6.7: FESEM micrographs of $(\text{Nd}_{0.5}\text{Li}_{0.5})_x\text{Zn}_{1-x}\text{O}$ ceramics sintered at 1623 K. Micrographs illustrated in the left (right) panel is 3000 (5000) times magnified.

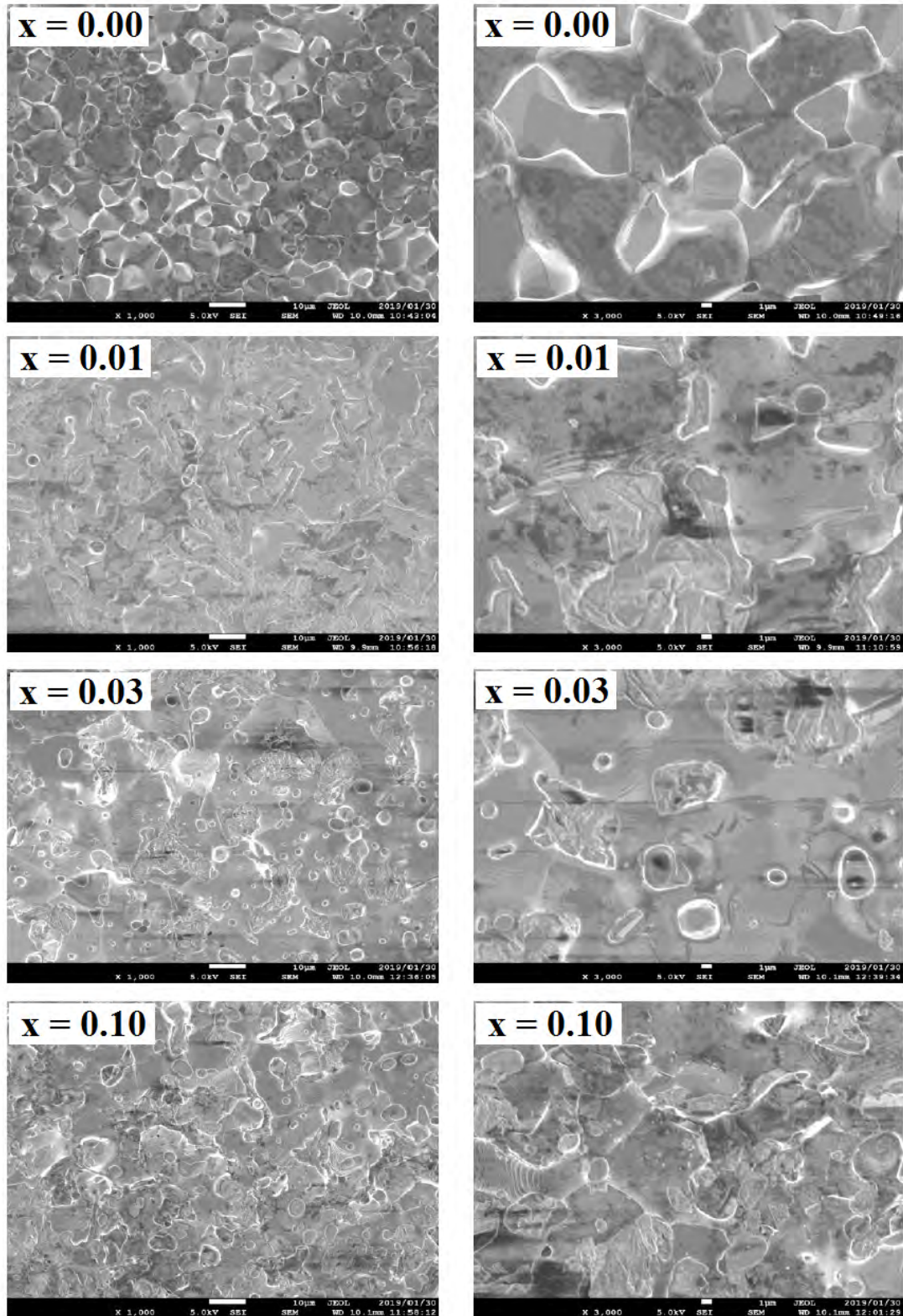


Fig. 6.8: FESEM micrographs of $(\text{Nd}_{0.5}\text{Li}_{0.5})_x\text{Zn}_{1-x}\text{O}$ ceramics sintered at 1648 K. Micrographs illustrated in the left (right) panel is 1000 (3000) times magnified.

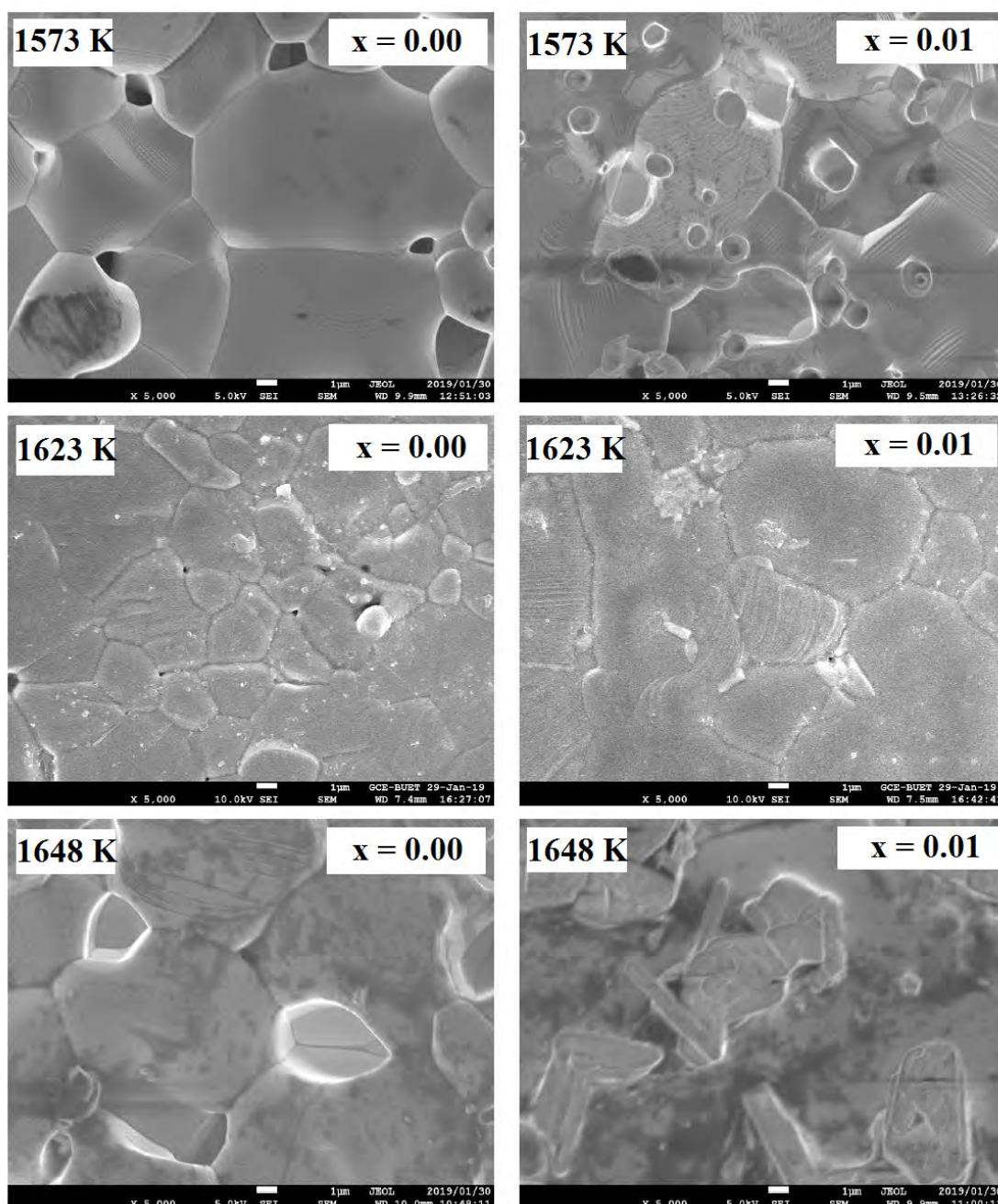


Fig. 6.9: FESEM micrographs of $(\text{Nd}_{0.5}\text{Li}_{0.5})_x\text{Zn}_{1-x}\text{O}$ ceramics sintered at 1573, 1623, and 1648 K.

However, It is observed that the average grain size is on average decreased with the increase in doping content showing similar trend as the variation of crystallites size as a function of doping content as shown in Fig. 6.5. This result accord well with others literature of donor acceptor co-doped ZnO ceramics [11, 12]. The decrease in grain size with doping content can be attributed to the slower diffusion of larger

Nd cation into ZnO ceramics. The increase in Li and Nd into ZnO leads to increase in the internal stress, resulting smaller grain size.

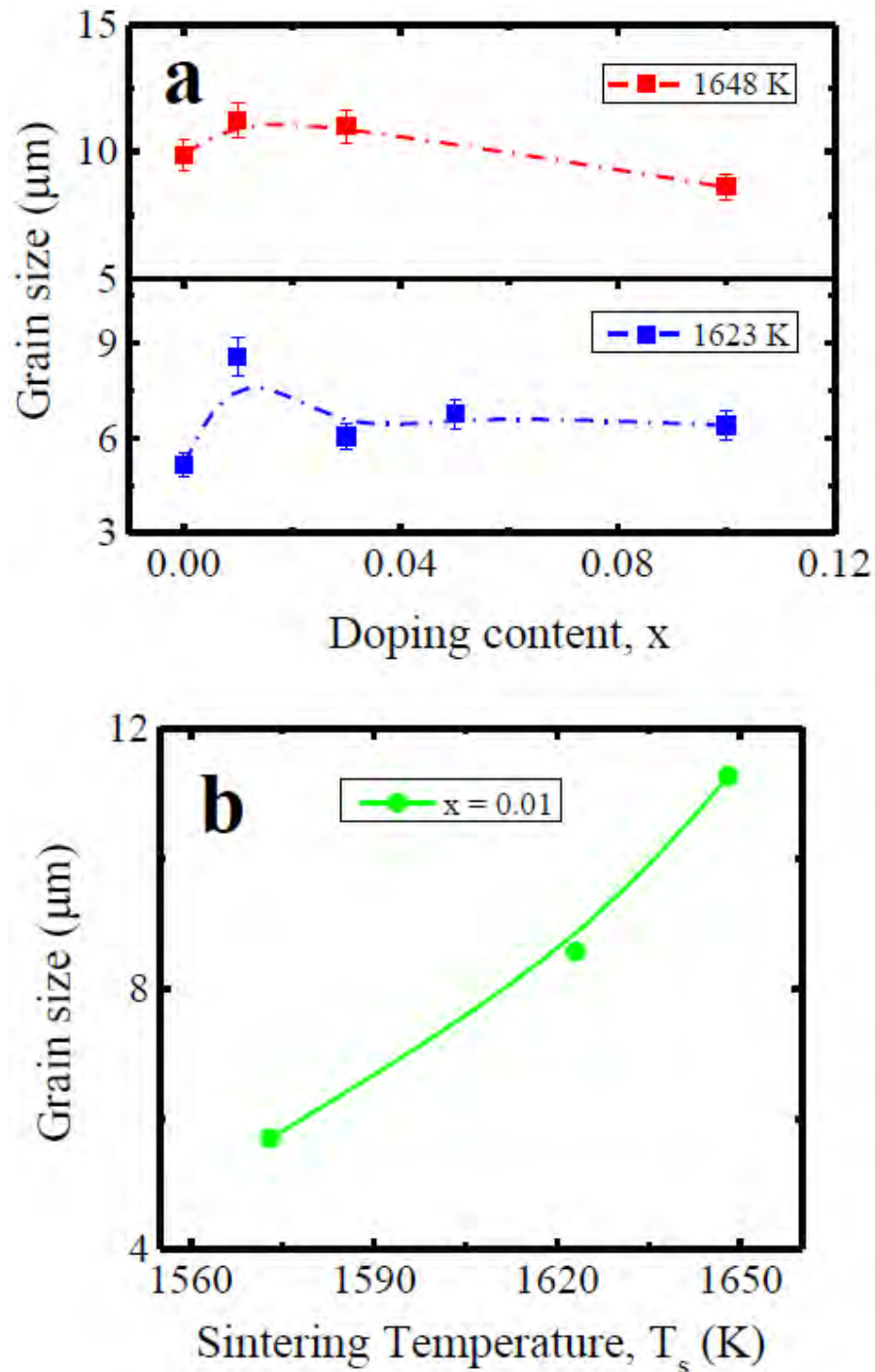


Fig. 6.10: Variation of average grain size as a function of (a) doping content and (b) sintering temperature of $(\text{Nd}_{0.5}\text{Li}_{0.5})_x\text{Zn}_{1-x}\text{O}$.

The average grain size as a function of sintering temperature of 1% (Li, Nd) co-

doped ZnO is depicted in Fig. 6.10(b). It is evident that the grain size is enhanced with the increase in T_s . Generally, a force is yielded during the sintering process because of the thermal energy that leads the grain boundaries to grow over pores thereby enhancing the grain size.

6.4 Energy Dispersive X-ray Analysis

For quantitative elemental analysis EDX spectra taken at various points of the sample is demonstrated in Fig. 6.11. The identified peaks are generated from O, Zn and Nd of the $(\text{Nd}_{0.5}\text{Li}_{0.5})_x\text{Zn}_{1-x}\text{O}$ ceramics. However, peak corresponds to Li is missing since Li is a very light element and remains undetected in EDX analysis.

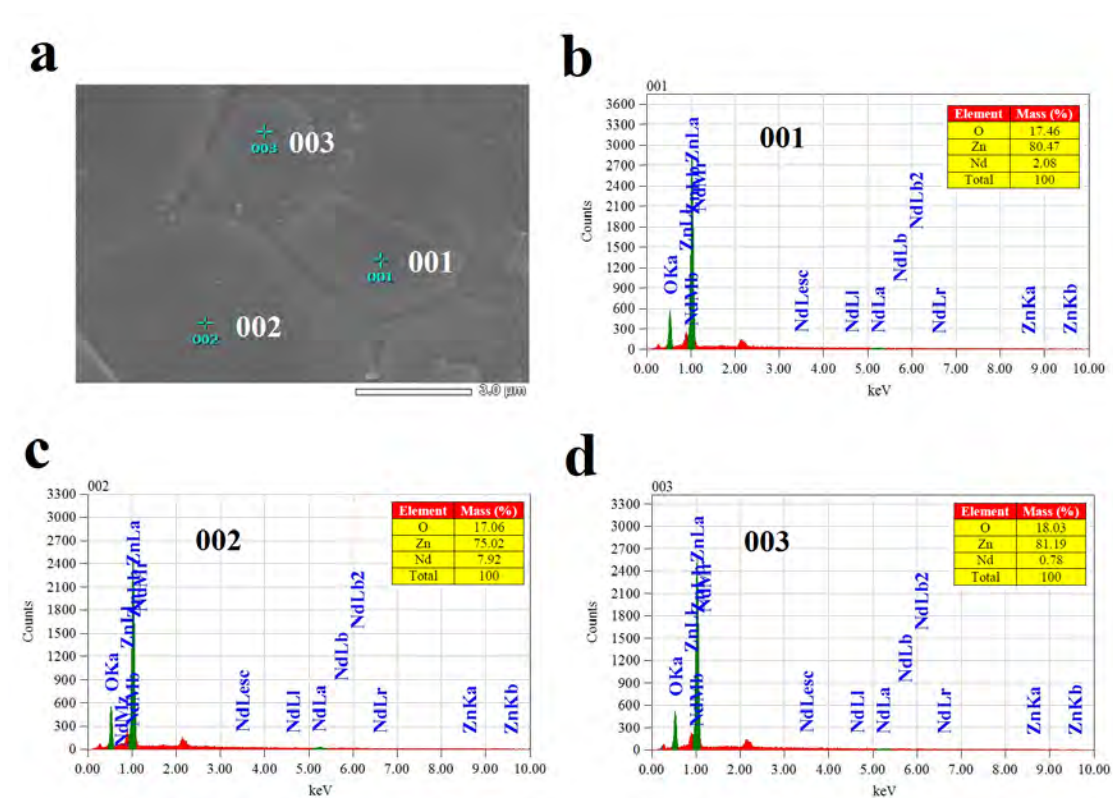


Fig. 6.11: EDX spectra of 1% (Li, Nd) co-doped ZnO ceramics sintered at 1623 K. (a) Image used for EDX analysis. Information corresponding to (b) point 001, (c) point 002 and (d) point 003, of $\text{Nd}_{0.005}\text{Li}_{0.005}\text{Zn}_{0.99}\text{O}$ ceramics.

It is found from the EDX spectra that there exist a well consistency between the

mass percentage of the elements in the component phase and nominal composition of the corresponding phase. Some variation occurs due to very high calcination and sintering temperature.

6.5 Dielectric Properties

6.5.1 Dielectric constant

Frequency dependent real part of dielectric constant (ϵ') of $(\text{Nd}_{0.5}\text{Li}_{0.5})_x\text{Zn}_{1-x}\text{O}$ ceramics sintered at 1473, 1573, 1623 and 1648 K are plotted in Fig. 6.12. It is evident that at lower frequency all the compositions exhibit higher values of dielectric constant. The permittivity is gradually decreased with the increase in frequency and becomes zero at very high frequency. Such frequency dependent dielectric behavior can be explained by Koops theory dependent on the Maxwell-Wagner model for inhomogeneous crystal structure [15-17]. This model proposed that a typical dielectric medium is composed of well conducting grains that are generally separated by resistive (poorly conducting) grain boundaries. When an external electric field is applied on a dielectric medium the charge carriers begin to migrate through the conducting grain and are piled up at the resistive grain boundaries. As a result, large polarization takes place within the dielectric medium resulting high dielectric constant. In this case the poorly conducting grain boundaries contribute to the higher value of permittivity at lower frequency.

Different types of polarization mechanism is also responsible for the higher values of permittivity at low frequency region. In the low frequency region all of the four polarization mechanisms (ionic, electronic, dipolar and space-charge polarization) contribute to the total polarization in the compound resulting high dielectric constant. But with the increase in frequency (i.e., at high frequency region) the contribution of some of the above-mentioned polarization mechanism to the total polarization is terminated resulting lower values of permittivity.

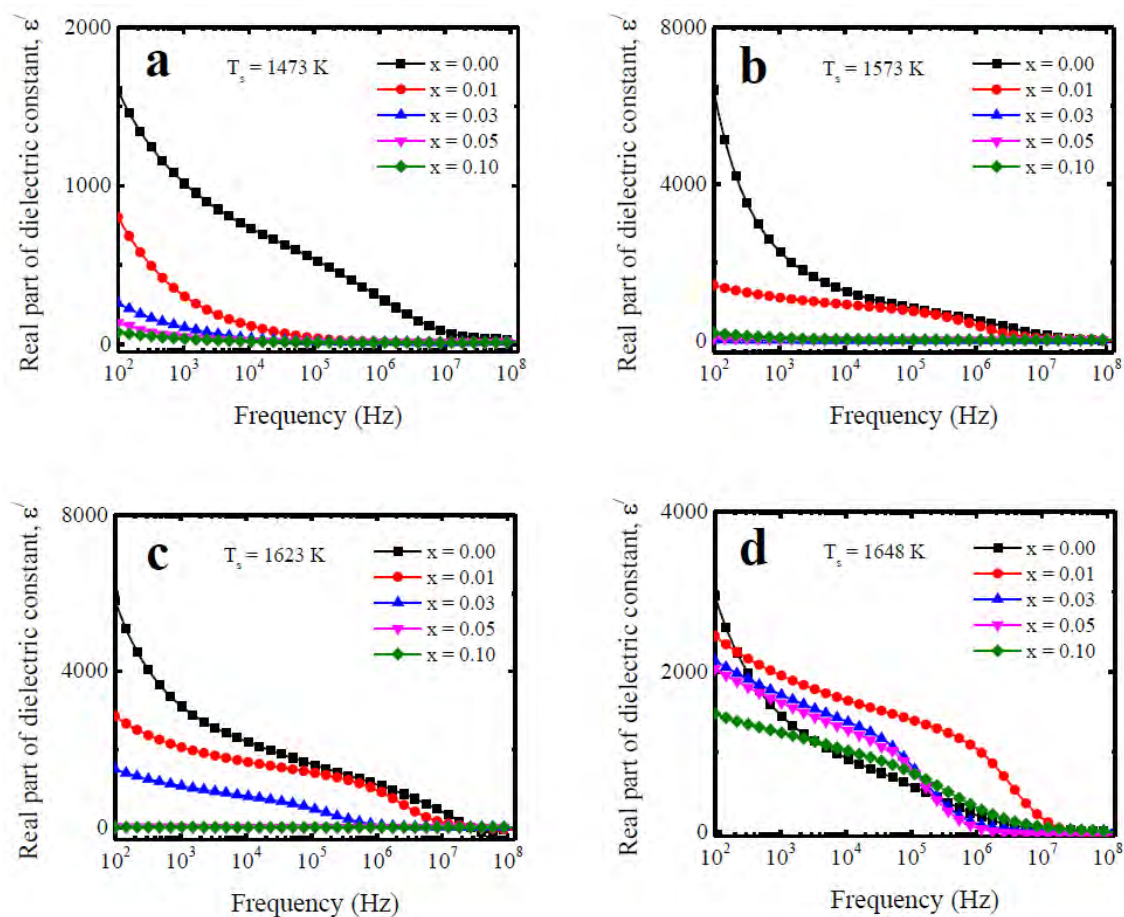


Fig. 6.12: Variation of dielectric constant as a function of frequency of $(\text{Nd}_{0.5}\text{Li}_{0.5})_x\text{Zn}_{1-x}\text{O}$ ceramics sintered at (a) 1473 K, (b) 1573 K, (c) 1623 K and (d) 1648 K.

6.5.2 Dielectric loss factor

The inherent dissipation of electromagnetic energy as a form of heat from a dielectric material is defined as the dielectric loss. There are two forms of loss in a dielectric medium. In conduction loss, the energy dissipation is caused by flowing of charge through a material. On the other hand, in dielectric loss the dissipation of energy is caused by the movement of charges in an alternating electromagnetic field as polarisation switches direction. Dielectric loss is high at the resonance or relaxation frequencies of the polarisation mechanisms as the polarisation lags behind the applied field, causing an interaction between the field and the dielectric's polarisation that results in heating [18]. Materials having higher dielectric constants generally

show higher dielectric loss.

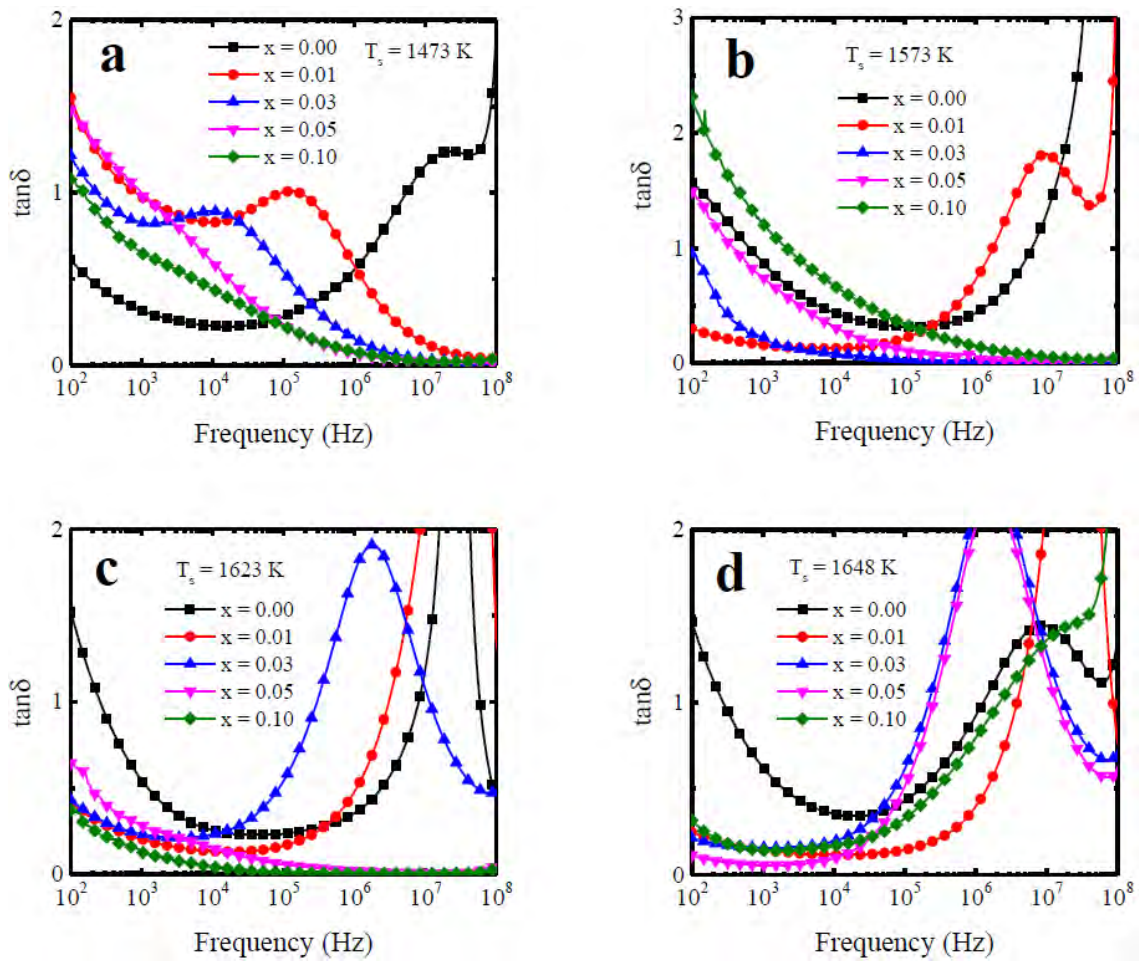


Fig. 6.13: Variation of loss tangent as a function of frequency of polycrystalline $(\text{Nd}_{0.5}\text{Li}_{0.5})_x\text{Zn}_{1-x}\text{O}$ ceramics sintered at (a) 1473 K, (b) 1573 K, (c) 1623 K and (d) 1648 K.

The frequency dependent dielectric loss factor ($\tan\delta$) of polycrystalline ceramics $(\text{Nd}_{0.5}\text{Li}_{0.5})_x\text{Zn}_{1-x}\text{O}$ sintered at 1473, 1573, 1623 and 1648 K are illustrated in Fig. 6.13. It is observed that at low frequency region the loss tangent is maximum and with the increase in frequency $\tan\delta$ is gradually decreased. The domain wall motion is suppressed at higher frequency and magnetization is changed by rotation resulting lower loss at higher frequency. However, there also appears some broad relaxation peaks at high frequency region indicating the existence of Debye-like relaxation [19]. Under the influence of externally applied field, the electric dipoles tend to align with the electric field. But the alignment is not happened instantaneously. The dipoles take some time to align with the field. This phenomenon is

known as dipole relaxation. When the relaxation or resonance frequency is equal to the applied frequency, a maximum in loss tangent may be occurred.

6.5.3 Composition and T_s dependence of ε' and $\tan\delta$

Fig. 6.14(a) illustrates the dependence of dielectric constant and dielectric loss factor on doping content of $(\text{Nd}_{0.5}\text{Li}_{0.5})_x\text{Zn}_{1-x}\text{O}$ ceramics sintered at 1623 K. It is evident that the relative permittivity is decreased with the increase in doping concentration. This phenomenon can be explained by the grain size distribution in corresponding samples. The grain size is slightly extended [Fig. 6.10] for 1% (Li, Nd) co-doping in ZnO, that allows to decrease the number of grains per unit volume resulting decrease the dipole moment of the whole system. As a result, the relative permittivity is decreased. However, for further increase in dopant content the grain size is decreased resulting further decrease in the relative permittivity. In general grains are made of multiple domains that are separated by domain walls. The value of dielectric constant depends upon the number of populations of domain and domain wall mobility [20]. Since the grain size is relatively small and non-uniform throughout the sample, the movement of domain wall is relatively difficult and irregular. As a result, the value of relative permittivity is decreased.

Moreover, it is also clear from Fig. 6.14(a) that the dielectric loss is also reduced with the increase in dopant concentration. Some anomaly occurs due to the presence of secondary phase in the desired samples. This phenomenon can be explained through the newly proposed dielectric polarization mechanism Electron Pinned Defect Dipole (EPDD) model [21]. According to this model, electrons are created by the donor atom Nd^{3+} . These electrons are then localized by the presence of acceptor atom Li^+ . These localized electrons lead to extra low dielectric loss [22].

Fig. 6.14(b) illustrates the dependence of dielectric constant and dielectric loss factor on sintering temperature of 1% doped $(\text{Nd}_{0.5}\text{Li}_{0.5})_x\text{Zn}_{1-x}\text{O}$ ceramics.

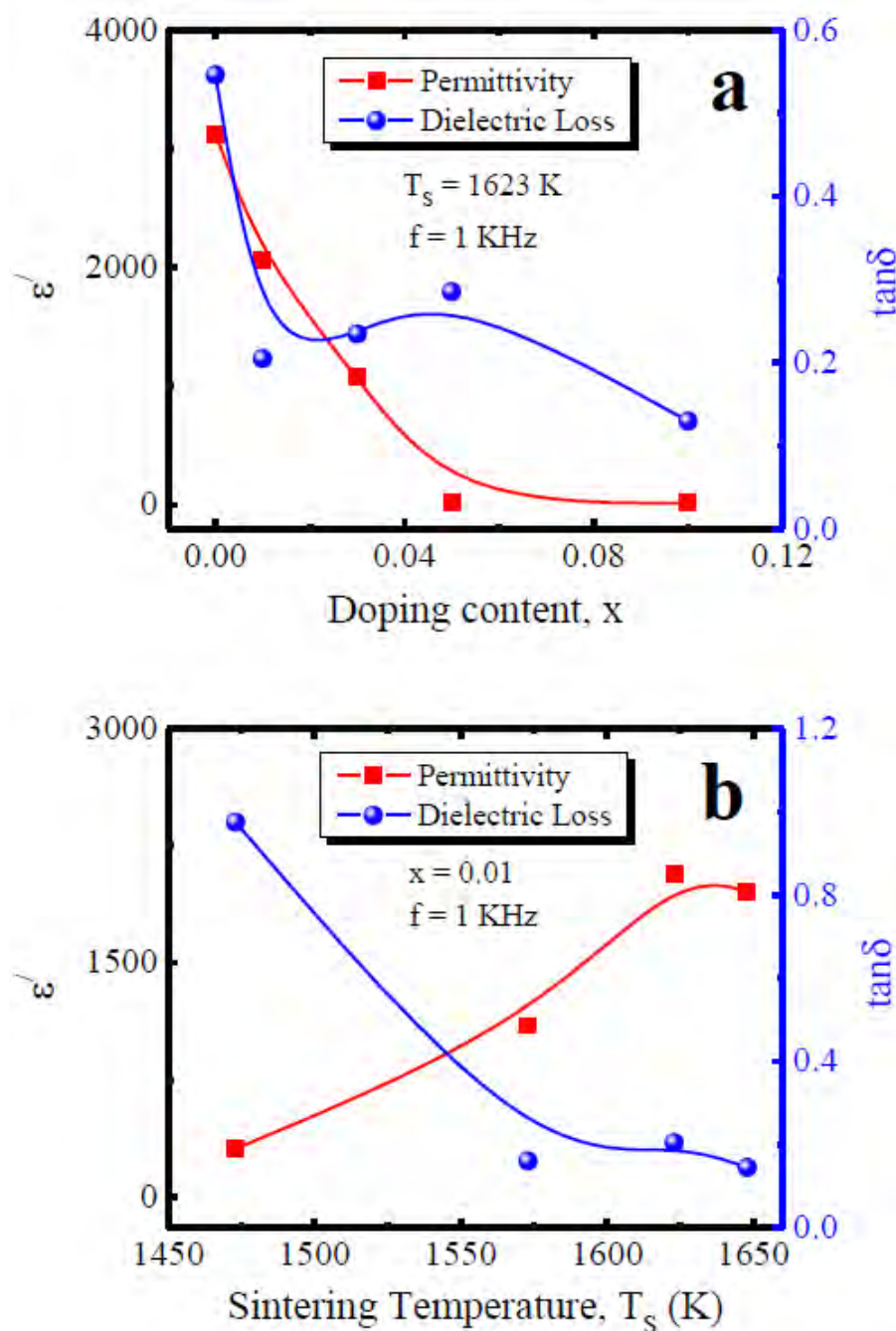


Fig. 6.14: (a) The permittivity and loss tangent as a function of doping concentration of $(\text{Nd}_{0.5}\text{Li}_{0.5})_x\text{Zn}_{1-x}\text{O}$ ceramics sintered at 1623 K. (b) Sintering temperature dependent permittivity and loss tangent of 1% (Li, Nd) co-doped ZnO ceramics.

The real part of dielectric constant is enhanced up to 1623 K and then begins to decrease for further increase in T_s . As shown in Fig. 6.10(b) the average grain size is enlarged with the increase in T_s making the movement of domain wall comparatively easier that contributes to the enhancement of relative permittivity. However,

it is also well established that density plays a vital role to control the dielectric properties of ceramic materials. As shown in Fig. 6.6(a) the bulk density of 1% doped composition is increased up to 1623 K and then begins to decrease for further increase in T_s showing exactly the similar trend with the variation of permittivity as a function of T_s . It is also observed that the dielectric loss is decreased with the increase in sintering temperature. However, It is clear from Fig. 6.14 that 1% (Li, Nd) co-doped ZnO shows slightly lower dielectric constant than pristine ZnO but relatively very low dielectric loss than pure ZnO ceramics sintered at 1623 K. Hence 1% (Li, Nd) co-doped ZnO sintered at 1623 K can be regarded as the optimum sample.

6.5.4 The ac-conductivity

For comprehending the conduction mechanism in different materials ac-conductivity σ_{ac} is a crucial parameter. The frequency dependent ac-conductivity of the studied compositions sintered at 1473, 1573, 1623 and 1648 K are illustrated in Fig. 6.15. The value of σ_{ac} of all the sintered samples is found almost constant at low frequency region. Whereas the value of σ_{ac} is increased very fast after a certain frequency. In low frequency region, the conductivity is almost independent of frequency because in this region the resistive grain boundaries are very active according to the Maxwell-Wagner double layer model [23, 24]. On the other hand in high frequency region (hopping region), the conductivity increases faster because of the very active conductive grains thereby enhances hopping of charge carriers that contributes to the rise in conductivity. Therefore, the transport phenomenon occurs through penetrating process in low frequency zone, whereas in high frequency zone the transport phenomena is kept up by hopping carriers that are generated from the substituted elements [25].

The frequency dependent ac-conductivity can also be explained through the polaron hopping model proposed by Austin and Mott [26]. Variation of $\log\sigma_{ac}$ with $\log\omega$ of the studied compositions sintered at 1473, 1573, 1623 and 1648 K

are illustrated in Fig. 6.16. According to the small polaron hopping model (large polaron hopping model) the value of σ_{ac} increases (decreases) with the enhancement of frequency [27]. It is evident from Fig. 6.16 that the mechanism of conduction of the studied samples can be explained by the small polaron hopping model since the value of σ_{ac} increases for all samples with the increase in frequency.

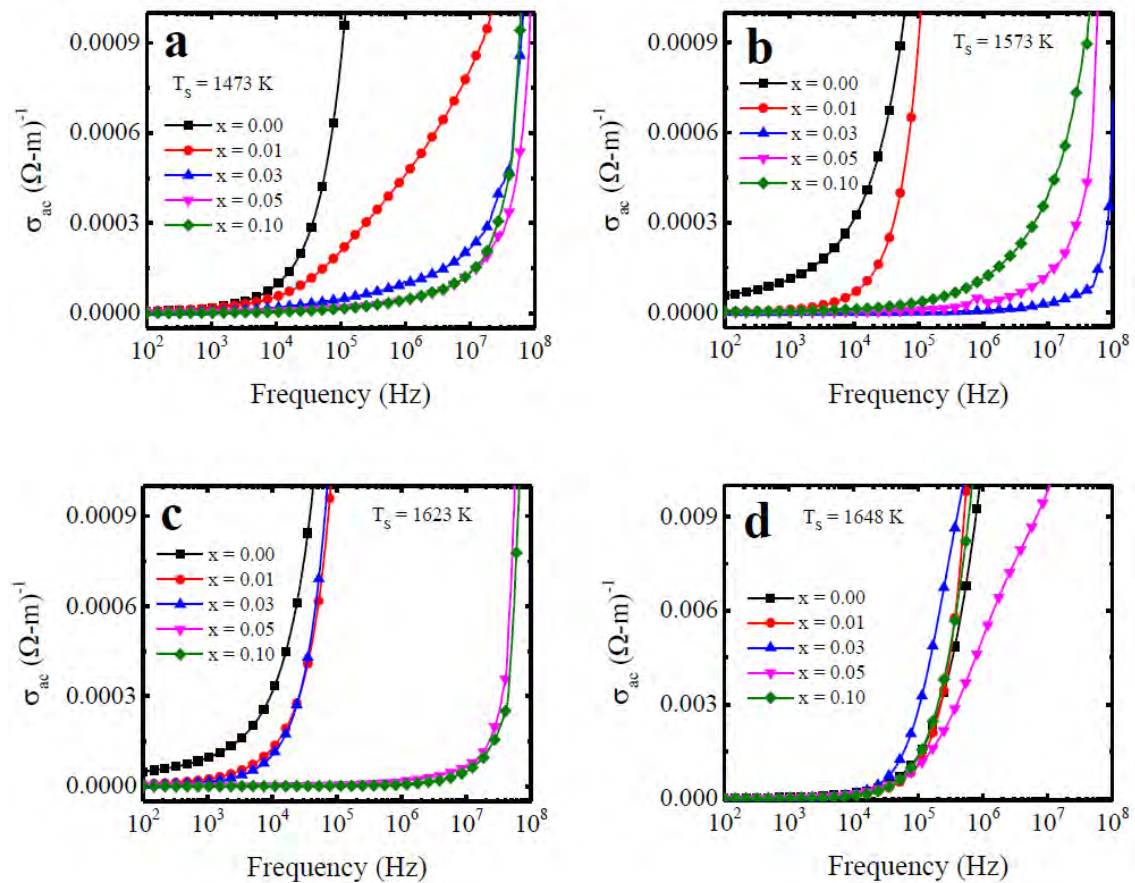


Fig. 6.15: Variation of ac-conductivity with frequency of polycrystalline $(\text{Nd}_{0.5}\text{Li}_{0.5})_x\text{Zn}_{1-x}\text{O}$ ceramics sintered at (a) 1473 K, (b) 1573 K, (c) 1623 K and (d) 1648 K.

6.5.5 Complex impedance spectra analysis

Complex impedance spectroscopy (CIS) is a very powerful approach for characterizing the electrical properties of materials. Fig. 6.17 illustrates the frequency dependent real part Z' and imaginary part Z'' of the impedance for $(\text{Nd}_{0.5}\text{Li}_{0.5})_x\text{Zn}_{1-x}\text{O}$ ceramics sintered at 1623 K.

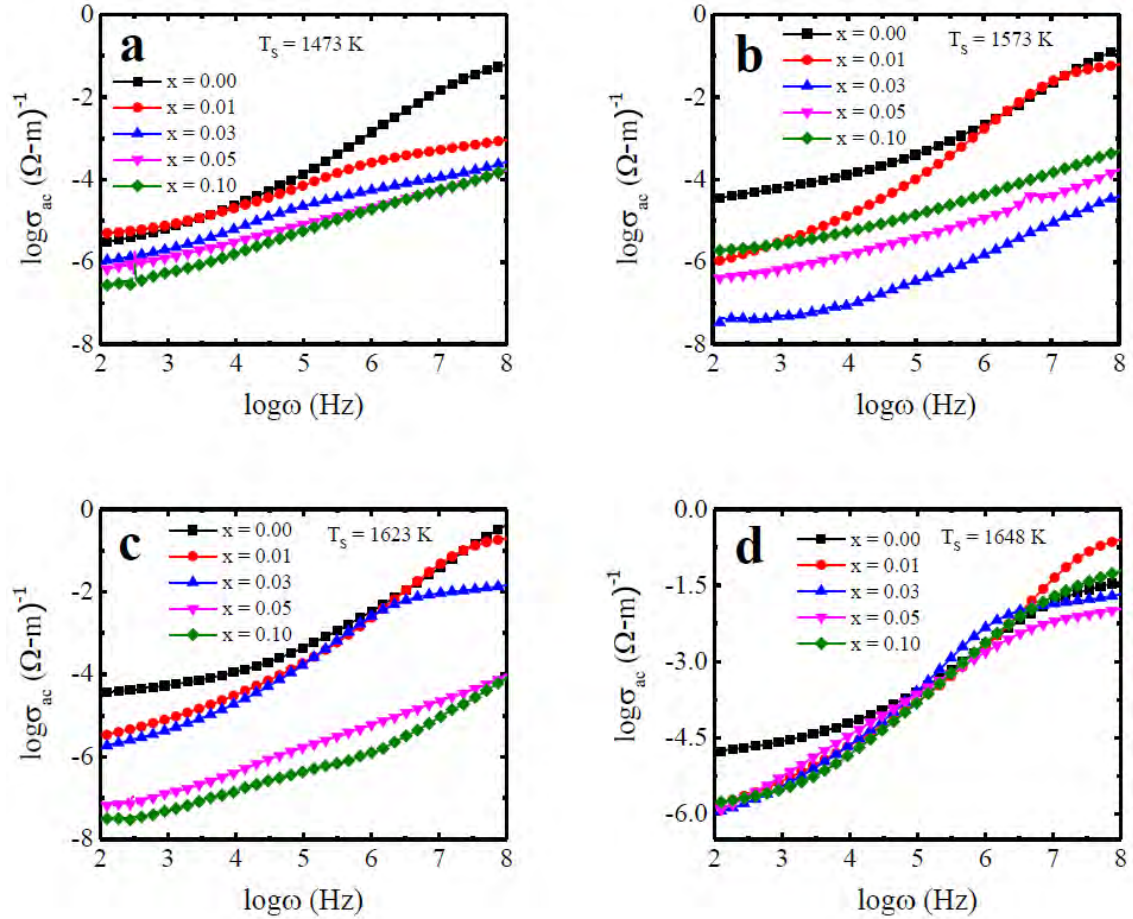


Fig. 6.16: Variation of $\log\sigma_{ac}$ with $\log\omega$ of polycrystalline $(\text{Nd}_{0.5}\text{Li}_{0.5})_x\text{Zn}_{1-x}\text{O}$ ceramics sintered at (a) 1473 K, (b) 1573 K, (c) 1623 K and (d) 1648 K.

It is evident from Fig. 6.17(a) that the value of Z' decreases sharply up to 1 KHz and then remains nearly constant at high frequency region implying the increase in electrical conductivity of the studied compositions. However, at high frequency region the plateau like nature of Z' implies possible occurrence of space charge polarization under the influence of external applied field [28]. The imaginary part of impedance Z'' exhibits similar nature as Z' [Fig. 6.17(b)]. No relaxation peak is appeared indicating the absence of immobile charges in $(\text{Nd}_{0.5}\text{Li}_{0.5})_x\text{Zn}_{1-x}\text{O}$ ceramics.

Fig. 6.18(a) shows the frequency dependent real part of electric modulus M' of $(\text{Nd}_{0.5}\text{Li}_{0.5})_x\text{Zn}_{1-x}\text{O}$ ceramics sintered at 1623 K. At lower frequency the magnitude of M' is nearly zero indicating the ease of polaron hopping [29, 30]. It also implies that the contribution of electrode effect in total impedance is very negligible in case of the studied compositions. However, the magnitude of M' increases gradually with

the increase in frequency for all the compositions.

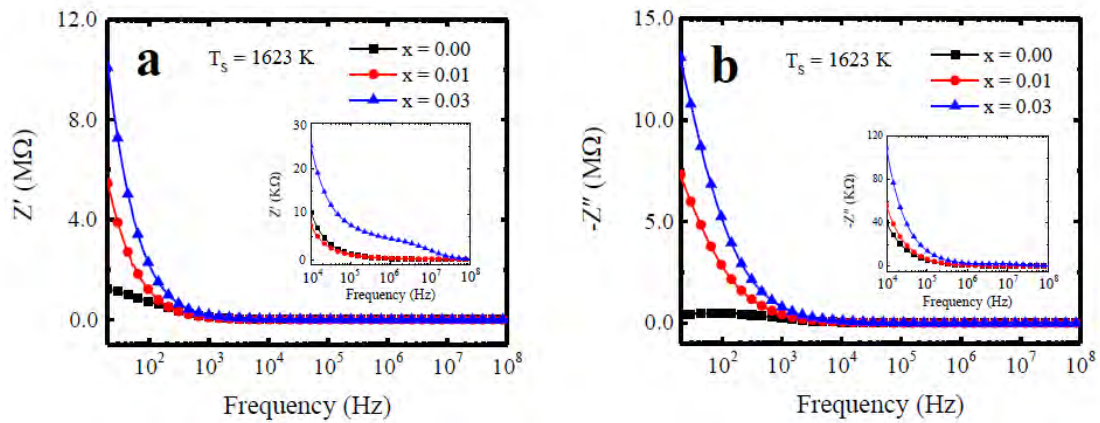


Fig. 6.17: Variation of (a) Z' and (b) Z'' , as a function of frequency of $(\text{Nd}_{0.5}\text{Li}_{0.5})_x\text{Zn}_{1-x}\text{O}$ ceramics sintered at 1623 K.

The frequency dependent imaginary part of dielectric modulus M'' is shown in Fig. 6.18(b). No relaxation peak is observed. Therefore, charge carriers are mobile in between the grains over the whole frequency range studied in the present case [31]. However, with the increase in frequency the magnitude of M'' is enhanced. Hence, at higher frequency the charge carriers may be trapped in a potential well and are allowed to mobile over short distances (inside the grains) [31].

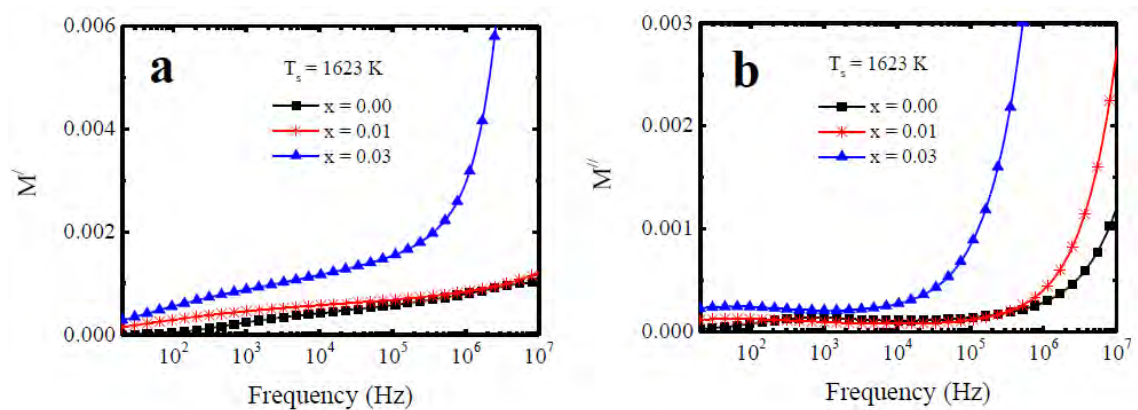


Fig. 6.18: Variation of (a) M' and (b) M'' , as a function of frequency of polycrystalline $(\text{Nd}_{0.5}\text{Li}_{0.5})_x\text{Zn}_{1-x}\text{O}$ ceramics sintered at 1623 K.

According to the brick-layer model [32] a polycrystalline ceramics can be rep-

represented by an equivalent circuit composed of three parallel RC components. By using these phenomena it is possible to separate the specific contribution of grain and grain boundaries to the total resistance. These three parallel RC circuits are connected in series combination with one another that corresponds to the grains, grain boundaries and electrode effect [33]. In a Nyquist plot (Z'' vs Z' plot) each RC component of the equivalent circuit generates a semicircle. Formation of a single semicircle indicates only the grain effects in the total resistance. Similarly, the formation of second and third semicircular arc corresponds to the grain boundary and electrode effects respectively. Fig. 6.19 demonstrates the Cole-Cole plot of $(\text{Nd}_{0.5}\text{Li}_{0.5})_x\text{Zn}_{1-x}\text{O}$ ceramics sintered at 1623 K.

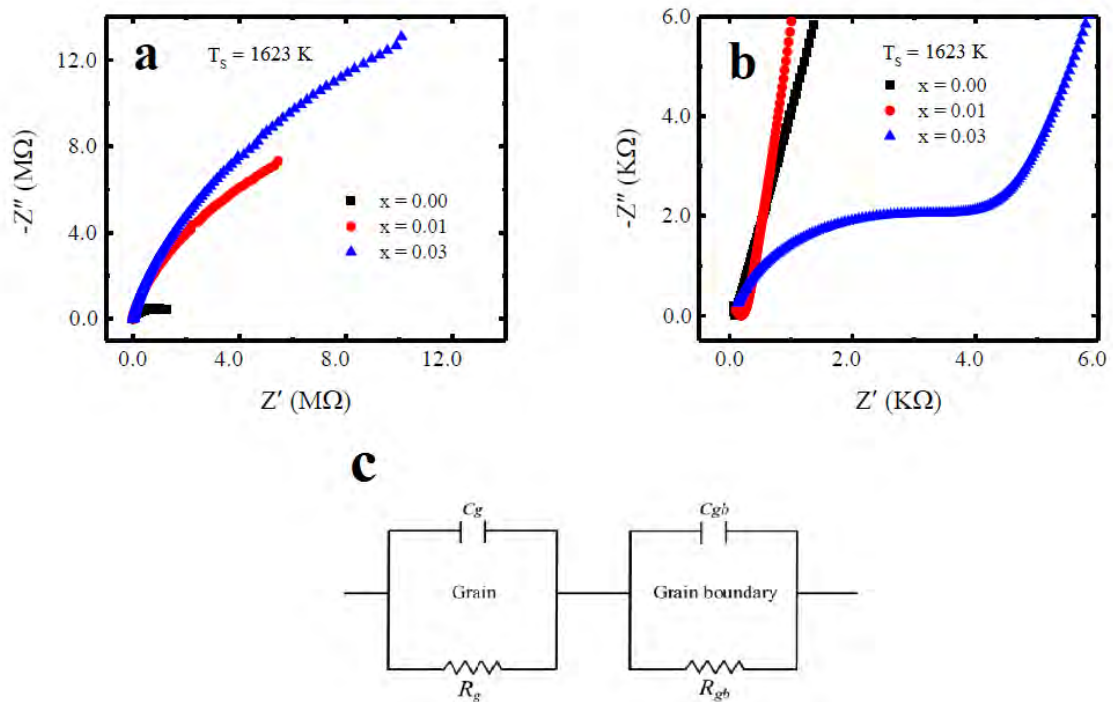


Fig. 6.19: The Cole-Cole plot of polycrystalline $(\text{Nd}_{0.5}\text{Li}_{0.5})_x\text{Zn}_{1-x}\text{O}$ ceramics sintered at 1623 K. (a) Z'' vs Z' plot at low frequency region. (b) Z'' vs Z' plot at high frequency region. (c) Equivalent circuit model.

It is observed that depressed semicircular arcs are formed indicating non Debye-type relaxation in $(\text{Nd}_{0.5}\text{Li}_{0.5})_x\text{Zn}_{1-x}\text{O}$ ceramics. Single semicircular arcs are formed for all the samples except 3% doped compositions. Two semicircular arcs are found in case of 3% doped ZnO ceramics. Therefore, dielectric contribution comes from

both the grain and grain boundary resistance in case of 3% doped profile since semicircle at high frequency [Fig. 6.19(b)] indicates only the grain effect (bulk resistance) and semicircle at low frequency indicates grain boundary effect to the total resistance. However, pristine and 1% doped profile possesses only single semicircle [Fig. 6.19(a)] which implies that in these compositions the major part of dielectric contribution comes from the grain boundary resistance. The dielectric properties of $(\text{Nd}_{0.5}\text{Li}_{0.5})_x\text{Zn}_{1-x}\text{O}$ ceramics can be represented by an equivalent RC circuit depicted in Fig. 6.19(c).

6.6 Magnetic Properties

6.6.1 Complex initial permeability

The complex initial permeability is an important magnetic parameter to have information about the dynamic properties and adaptability of a magnetic material in high frequency. The complex initial permeability is usually given by, $\mu_i^* = \mu_i' - i\mu_i''$, where μ_i' and μ_i'' are defined as the real and imaginary parts of complex initial permeability, respectively. μ_i' expresses the component of magnetic induction B in phase with the alternating magnetic field H and typically used to denote the magnetic energy that store in the system. The dissipation of magnetic energy from a system is defined by μ_i'' that usually represents the component of magnetic induction B out of phase with H.

Fig. 6.20 illustrates the frequency dependent real part of complex initial permeability μ_i' of $(\text{Nd}_{0.5}\text{Li}_{0.5})_x\text{Zn}_{1-x}\text{O}$ ceramics at various sintering temperature. It is observed that the value of μ_i' is almost constant over the whole range of frequency for all the samples. One possible reason can be their ferromagnetic resonance frequency (cut-off frequency) that lies beyond the measured frequency range. The cut-off frequency is defined as the frequency at which the value of μ_i' becomes half of its initial value. The observed results shows good accordance with the Globus

model [34], that relates the permeability with resonance frequency as,

$$(\mu_i - 1)^{1/2} f_r = \text{constant} \quad (6.1)$$

This relation implies that the larger the value of μ_i the smaller the value of f_r .

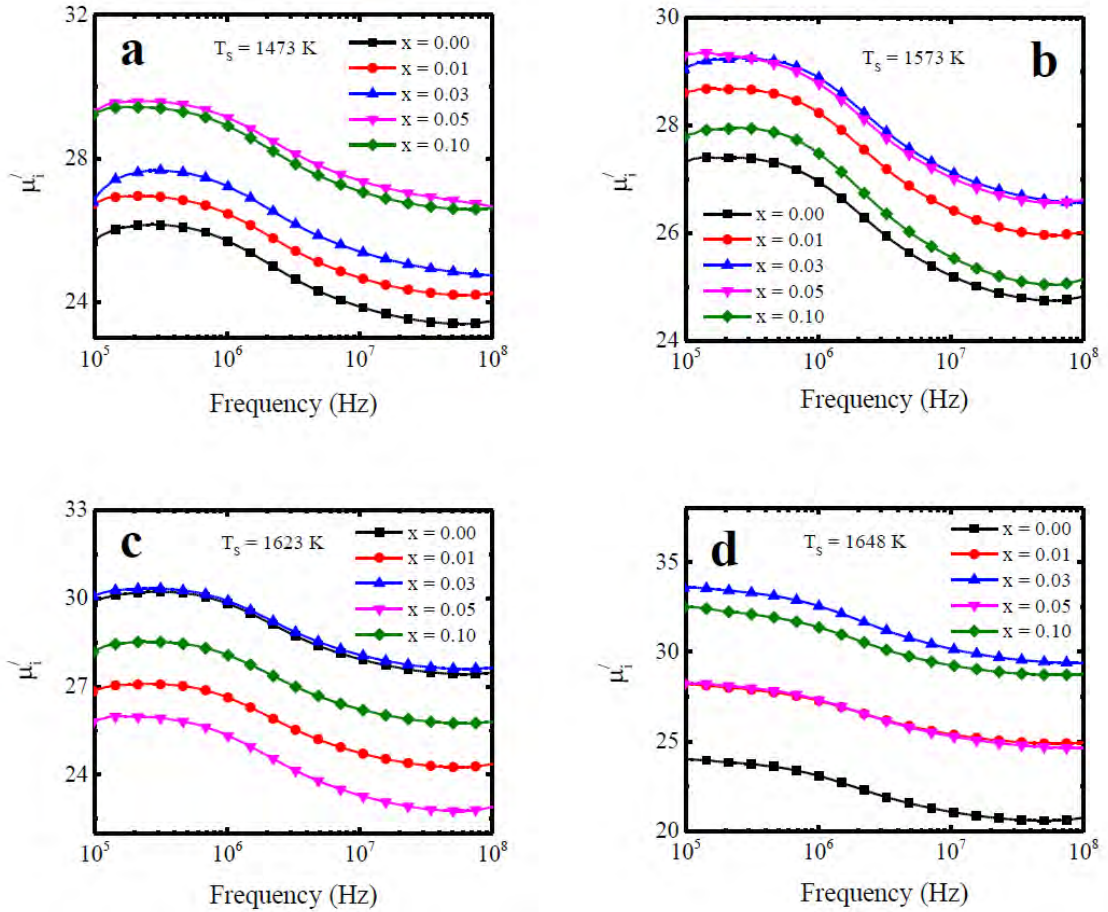


Fig. 6.20: Frequency dependent real part of complex initial permeability μ'_i of polycrystalline $(\text{Nd}_{0.5}\text{Li}_{0.5})_x\text{Zn}_{1-x}\text{O}$ ceramics sintered at (a) 1473 K, (b) 1573 K, (c) 1623 K and (d) 1648 K.

Since the value of μ'_i of all the samples is comparatively low, no resonance peak is observed in the measured frequency range. However, The reason behind the high frequency stability can be attributed to the phenomena that the magnetic moments are able to rearrange with the variation of external applied magnetic field for a long period of time during the process of magnetization [35]. This high frequency stability is very important for many technological applications including wide band read-write head for video recording and broad band transformer [36, 37]. However,

a slight decrease in the value of μ'_i is also observed with the increase in frequency due to the generation of pinning points at the surface of the samples from the impurities and intra-granular pores. For this reason the domain wall motion is hindered resulting the decrease of permeability [38]. Due to the presence of secondary phase it is very difficult to explain the composition and sintering temperature dependent μ'_i . However, permeability depends on many other factors such as stoichiometry, porosity, pressure etc.

6.6.2 Relative quality factor

The Relative quality factor (RQF) is generally used as a measure of performance of materials for real world applications.

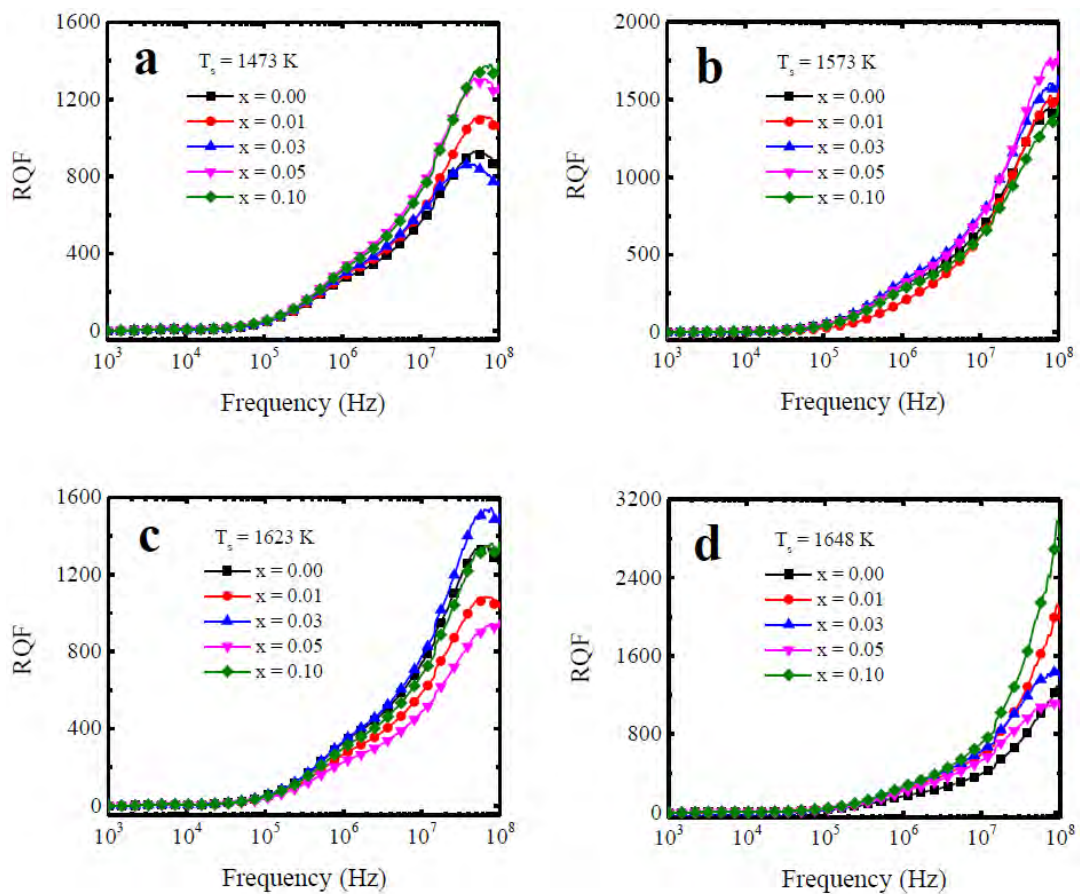


Fig. 6.21: Frequency dependent RQF of polycrystalline $(\text{Nd}_{0.5}\text{Li}_{0.5})_x\text{Zn}_{1-x}\text{O}$ ceramics sintered at (a) 1473 K, (b) 1573 K, (c) 1623 K and (d) 1648 K.

The variation of RQF with frequency of the studied compositions are illustrated in Fig. 6.21. It is evident that the value of RQF increases with the increase in frequency for all the compositions. This implies that with the increase in frequency the utility of the studied compositions is enhanced. It is also noticed that with the increase in sintering temperature the value of RQF is enhanced. Since at higher T_s abnormal grain growth may occur, it is very difficult to explain the variation of RQF with composition and sintering temperature.

6.7 Theoretical Analysis

6.7.1 Structural properties

The (Li, Nd) co-doped ZnO ceramics belongs to the space group $P6_3mc$ with wurtzite hexagonal type crystal structure as shown in Fig. 6.22. The calculated lattice parameters and unit cell volume are listed in Table 6.6 with the experimental values obtained in this study. From Table 6.6 it is evident that the theoretically calculated lattice parameters show good consistency with the experimental data bearing the reliability of this present study. The existing minor deviation of the calculated values from the experimental ones can be caused by the temperature dependency of cell parameters and GGA process [39].

Table 6.6: The theoretical and experimental unit cell parameters of pristine and (Li, Nd) co-doped ZnO ceramics.

Properties	Pure ZnO		Doped ZnO	
	Calc.	Expt.	*Calc.	**Expt.
a_0 (nm)	0.32848	0.32457	0.33394	0.32474
c_0 (nm)	0.52965	0.51940	0.52628	0.51972
V_0 (nm ³)	0.04949	0.04738	0.05082	0.04746

*12.5 atom% (Li, Nd) co-doped ZnO. **10 weight% (Li, Nd) co-doped ZnO.

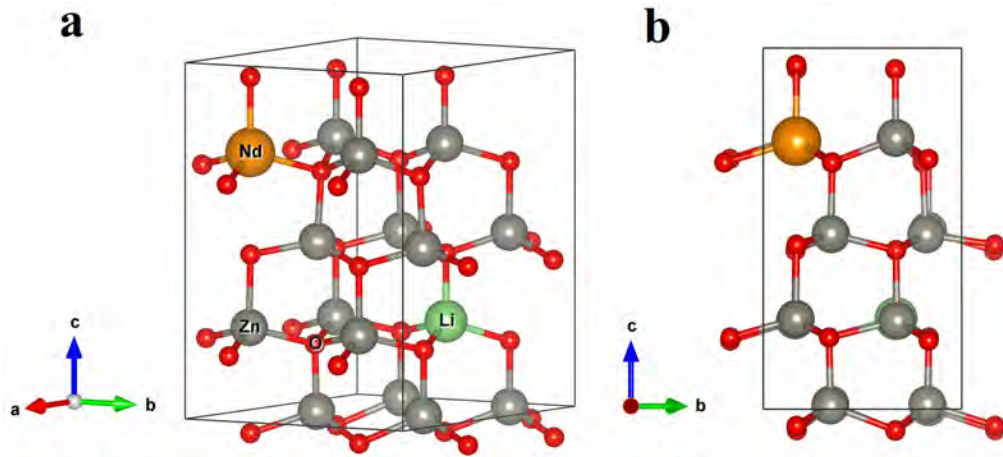


Fig. 6.22: The crystal structure ($2 \times 2 \times 2$ supercell) of (Li, Nd) co-doped ZnO ceramics. (a) Three dimensional and (b) two dimensional view.

6.7.2 Mechanical properties

For ensuring the mechanical stability of $(\text{Nd}_{0.5}\text{Li}_{0.5})_x\text{Zn}_{1-x}\text{O}$ ceramics the elastic constants of the pristine and doped phases are calculated and discussed. The calculated elastic constants of pristine and co-doped ZnO are tabulated in Table 6.7. It is evident that the studied compositions fulfill the well established Born stability criteria for hexagonal cell [40] given as follows,

$$C_{11} > 0, C_{44} > 0, C_{11} - C_{12} > 0 \text{ and } (C_{11} + C_{12})C_{33} > 2(C_{13})^2$$

Hence, both the pristine and co-doped phases are mechanically stable in nature. The Cauchy pressure ($C_{12}-C_{44}$) is a useful parameter to predict the brittleness and ductility of materials. The negative (positive) value of this parameter indicates the brittle (ductile) nature of a compound [41]. The computed values of the Cauchy pressure of pristine and co-doped samples are positive [Table 6.7] implying that the co-doped sample is ductile as the pristine ZnO.

By using the computed elastic constants the most important mechanical parameters of a compound such as the shear modulus G , bulk modulus B , Young's modulus E , B/G ratio and Poisson's ratio ν of pristine and co-doped samples are calculated and listed in Table 6.8. The bulk modulus is one of the essential me-

mechanical parameter for getting idea about the stiffness of a material. The calculated bulk modulus of both the composition is comparatively large (>100 GPa), hence these compounds can be classified as relatively hard materials. However, The value of B is slightly decreased after co-doping.

Table 6.7: The evaluated elastic constants C_{ij} (GPa) and Cauchy pressure of pristine and (Li, Nd) co-doped ZnO ceramics.

Phase	C_{11}	C_{12}	C_{13}	C_{33}	C_{44}	C_{66}	$C_{12}-C_{44}$
ZnO	187.90	108.83	88.28	192.76	38.07	39.60	70.76
$(\text{Nd}_{0.5}\text{Li}_{0.5})_x\text{Zn}_{1-x}\text{O}$	174.03	103.05	79.17	157.08	34.60	34.33	68.45

The shear modulus is used to get idea about the plastic deformation of a material under external stress. As shown in Table 6.8 the value of G of both the samples is comparatively large. The value of G is slightly decreased after co-doping into ZnO. The smaller value of G after co-doping compared to pure ZnO indicates weaker bond and lower shear resistance in $(\text{Nd}_{0.5}\text{Li}_{0.5})_x\text{Zn}_{1-x}\text{O}$ ceramics [42]. Similar trend is noticed for Young's modulus of both the compositions. The obtained young's modulus of co-doped sample is smaller than that of pure ZnO (Table 6.8) demonstrating that $(\text{Nd}_{0.5}\text{Li}_{0.5})_x\text{Zn}_{1-x}\text{O}$ is less stiffer than pristine ZnO ceramics [43].

Table 6.8: The evaluated mechanical parameters of pristine and (Li, Nd) co-doped ZnO ceramics.

Phase	B (GPa)	G (GPa)	E (GPa)	ν	B/G	A^U
ZnO	126.51	41.61	112.51	0.35	3.03	0.10
$(\text{Nd}_{0.5}\text{Li}_{0.5})_x\text{Zn}_{1-x}\text{O}$	113.53	36.69	99.38	0.35	3.09	0.08

For explaining the bonding nature and plasticity of a material the Poisson's ratio is another useful parameter. The calculated value of ν for both the compositions is 0.35 implying the existence of central force in both the samples since $0.25 < \nu < 0.50$ indicates the central force in a crystal [44]. The Poisson's ratio is another useful

indicator of ductility and brittleness of materials. The critical value for separating the ductility and brittleness of a material is 0.26 [45]. If $\nu < 0.26$, the compound will be brittle in the manner otherwise the compound will be ductile. According to this condition, both the pristine and co-doped ZnO is ductile in nature. The ratio between bulk modulus and shear modulus is usually known as Pugh's ratio which is also used to predict the failure mode of a material. In this case, the critical value for separating the ductility and brittleness of a material is 1.75 [46]. As shown in Table 6.8 both the studied compositions are ductile in nature as the value of B/G is greater than the critical value. After co-doping in ZnO the value of B/G is slightly increased. For studying the anisotropic characteristics of the studied compositions the universal anisotropy factor A^U is evaluated. A^U is zero for completely isotropic materials otherwise the material will be anisotropic [47]. From Table 6.8 it is evident that both the compositions show large anisotropic characteristics whereas $(\text{Nd}_{0.5}\text{Li}_{0.5})_x\text{Zn}_{1-x}\text{O}$ is less anisotropic than the pristine ZnO.

6.7.3 Electronic properties

For explaining the bonding features of (Li, Nd) co-doped ZnO ceramics the basic electronic properties including the band structure, density of states (DOS) and charge density of the studied compositions are calculated and discussed in details. Fig. 6.23 illustrates the electronic band structures of pristine and various metal doped ZnO ceramics. As shown in Fig. 6.23(a) the calculated band gap of pure ZnO ceramics is 0.743 eV which shows good consistency with other theoretically calculated band gap value [48] implying the reliability of the present calculation. It is evident that the computed band gap value underestimates the experimentally evaluated band gap value 3.2 eV [48]. The reason can be attributed to the well informed limitation of GGA. The Local Density Approximation (LDA) and LDA+U methods also underestimate the band gap value. Sometimes Heyd-Scuseria-Ernzerhof (HSE) hybrid potential may provide the band gap value close to the experimental one, but it is also not valid for all of the materials. Partial correction of the theoretical

band gap value relative to the experimental one can be achieved by using GGA+U approach. However, the present study only focuses on the variation of band gap due to different metal doping in ZnO ceramics by ignoring the band gap error of GGA approach.

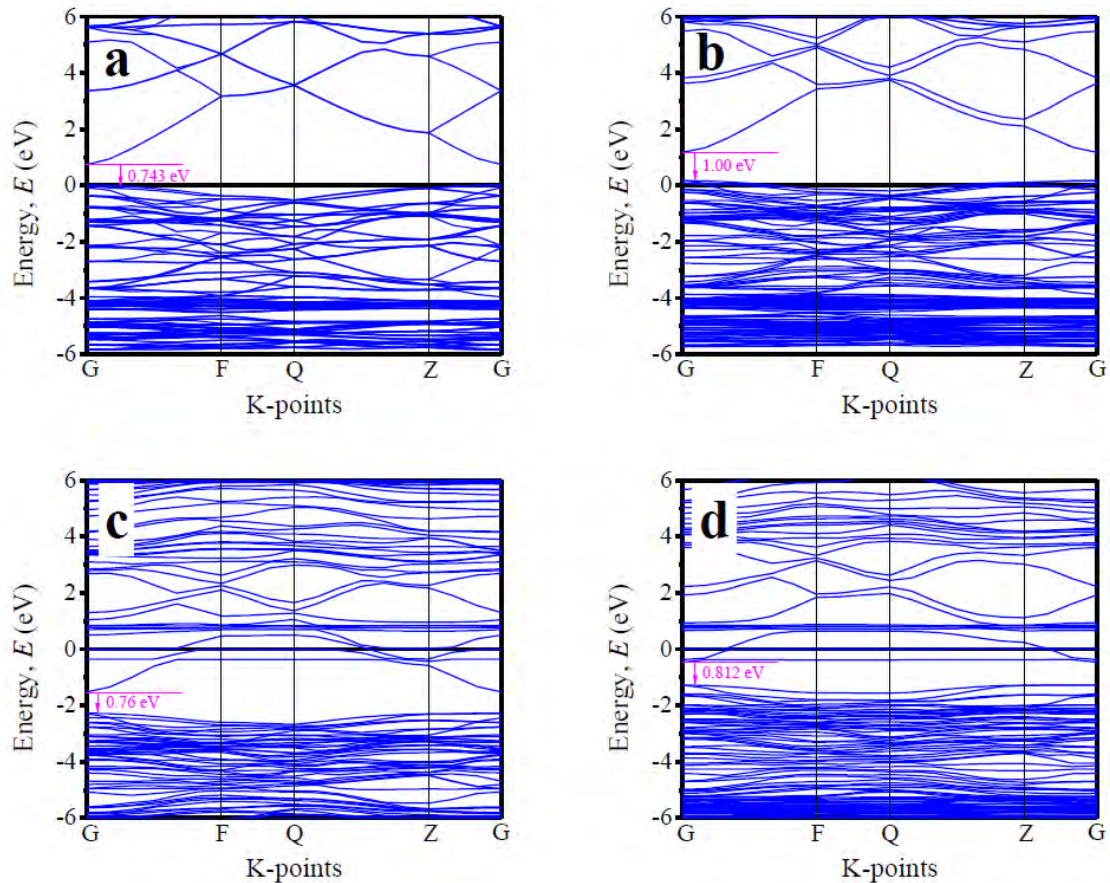


Fig. 6.23: The band structure diagram of ZnO ceramics calculated by using (a) pure supercell, (b) Li-doped, (c) Nd-doped and (d) Li and Nd co-doped sample.

Figs. 6.23(b) and (c) illustrates the band structure of individual Li and Nd doped ZnO, respectively. The calculated band gap value is well consistent with other works [49]. It is clear that Li doping at Zn-site (p-type dopant) shifts the Fermi level toward the valence band whereas Nd doping at Zn-site (n-type dopant) shifts the Fermi level toward the conduction band. The band gap is slightly increased in both the cases. Fig. 6.23(d) shows the band structure of Li and Nd co-doped ZnO ceramics. It is evident that the Fermi level shifts toward the conduction band. Here, the shift of Fermi level into the conduction band can be defined as the positive

Burstein shift. However, the band gap is slightly increased compared to the pristine ZnO. This broadening of the band gap can be ascribed to the phenomena known as Moss-Burstein effect [50].

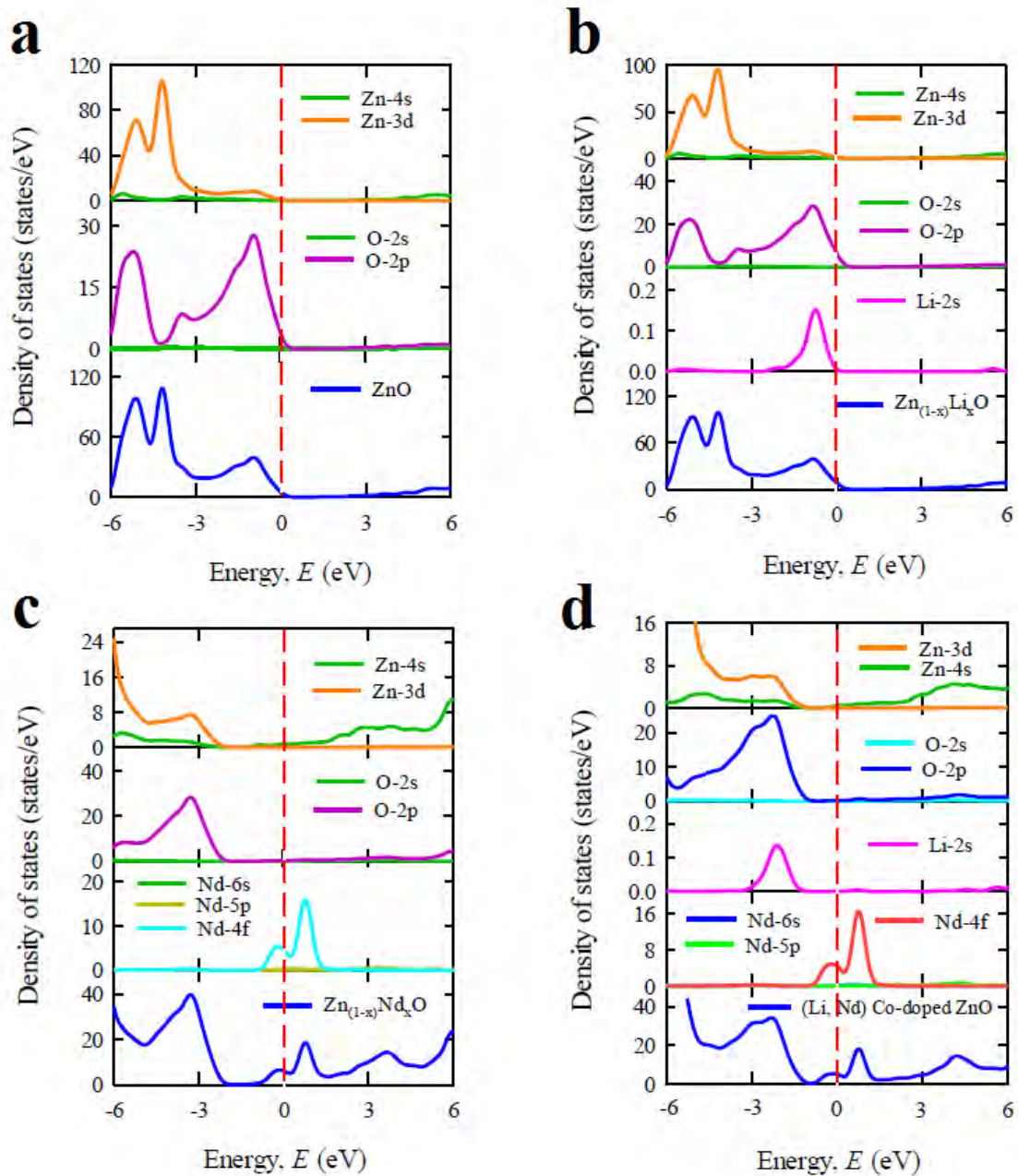


Fig. 6.24: The total and partial density of states of ZnO ceramics simulated by using (a) pure supercell, (b) Li-doping at Zn-site, (c) Nd-doping at Zn-site and (d) Li and Nd co-doping at Zn-site of ZnO.

The total and partial density of states of pristine and co-doped ZnO is depicted

in Fig. 6.24. Fig. 6.24(a) illustrates the DOS profile of pure ZnO ceramics. As shown in the figure the valence band is mostly composed of Zn-3d and O-2p orbitals with small contribution of Zn-4s and O-2s orbitals. The conduction band is mainly composed of Zn-4s orbital with small contribution of O-2p orbitals. After Li doping in ZnO a slight change is observed in the overall DOS profile as shown in Fig. 6.24(b). However, a major change is occurred when Nd is inserted into the Zn-site of ZnO ceramics as shown in Fig. 6.24(c). After Nd doping the Fermi level shifts toward the conduction band. A major change is observed in the conduction band. An extra peak is appeared in the total DOS due to the formation of dopant states (Nd-4f) in the conduction band of ZnO ceramics. Similar trend is observed for Li and Nd co-doped ZnO as shown in Fig. 6.24(d). The conduction band slightly shifts toward the lower energy region.

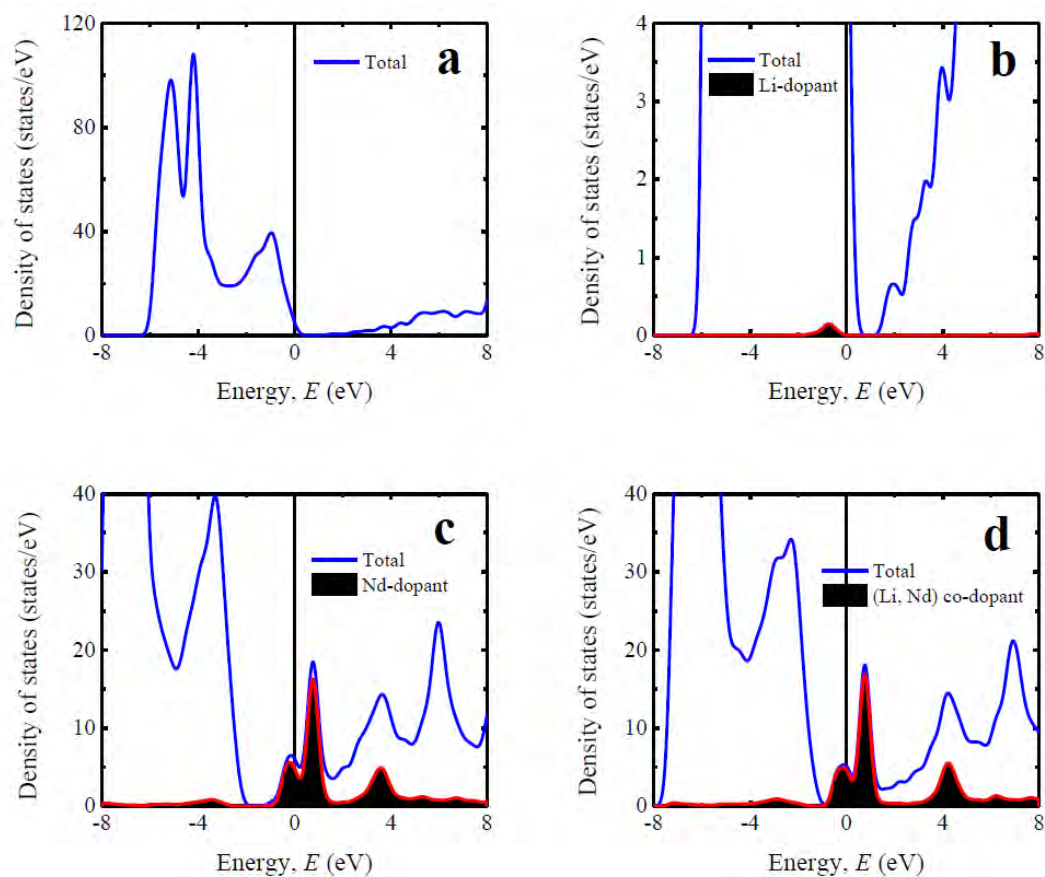


Fig. 6.25: Dopant contribution at Fermi level of ZnO ceramics. (a) Pristine ZnO, (b) Li-doped ZnO, (c) Nd-doped ZnO and (d) (Li, Nd) co-doped ZnO.

Fig. 6.25 illustrates the change of band gap due to the formation of new dopant states near Fermi level. It is evident that Li-dopant has very small contribution near the Fermi level [Fig. 6.25(b)]. In case of Nd-doped ZnO [Fig. 6.25(c)] the impurity energy states are formed over the Fermi level. These impurity states can trap the photoexcited holes which reduce the recombination rate of electrons and holes [51]. Similar effect is observed for Li and Nd co-doped ZnO as shown in Fig. 6.25(d). However, the band gap value is intermediate between the band gap of individual Li and Nd doped ZnO due to the combined effect of Li and Nd-dopant near Fermi level of ZnO ceramics.

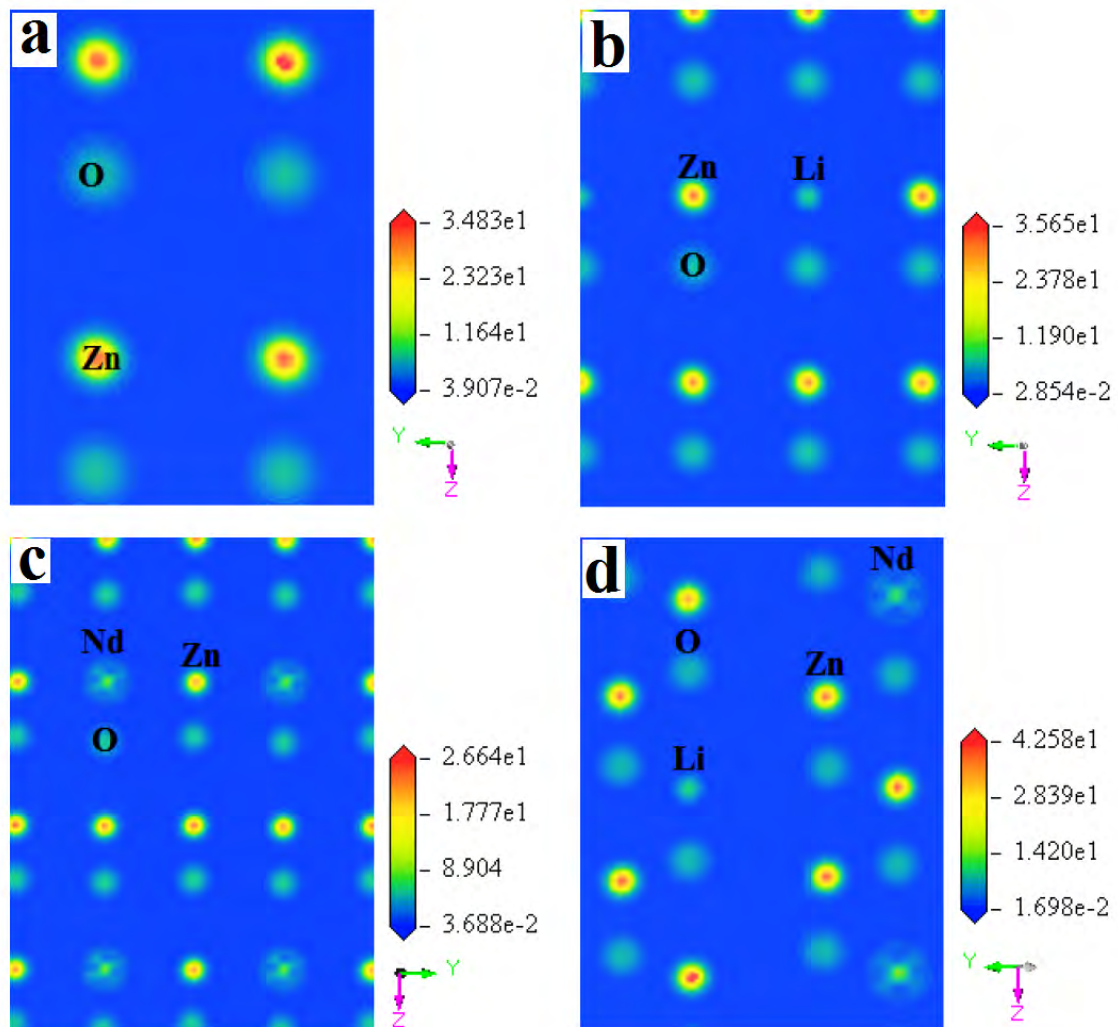


Fig. 6.26: The total charge density of (a) pristine ZnO, (b) Li-doped ZnO, (c) Nd-doped ZnO and (d) Li and Nd co-doped ZnO.

The contour diagrams of the total charge density is very useful for analyzing

the detailed chemical bonding within a material. In order to get a clear insight about the total electronic charge distribution and bonding properties, the total electronic charge density map of pristine and doped ZnO is illustrated in Fig. 6.26. For representing the intensity of charge (electron) density, a scale has been shown at the right side of all contour plots where the blue and red color indicates the light and high density of electron, respectively. From Fig. 6.26 it is evident that there is no overlapping of charge distribution among O and Zn atoms in all the cases showing the ionic character of Zn-O bonds. After doping there is no major change appeared in the charge distribution. It is evident from Fig. 6.26(d) that both the Li and Nd atoms substitute the Zn-site of ZnO ceramics. However, the size of Nd ion is comparatively larger than Zn ion causes instability in $(\text{Nd}_{0.5}\text{Li}_{0.5})_x\text{Zn}_{1-x}\text{O}$ ceramics.

6.7.4 Optical properties

The study of optical properties is essential for discovering a suitable material in the metal oxide family for the application in optoelectronic devices and solar cells. In this section of the thesis the important optical parameters including absorption coefficient, reflectivity, real and imaginary part of dielectric constant and optical conductivity of pristine and (Li, Nd) co-doped ZnO are analyzed and discussed in details.

The evaluated absorption profiles of pristine and co-doped ZnO are illustrated in Fig. 6.27. The optical absorption coefficient is defined as the fraction of energy (wavelength) absorbed per unit length of the material. It also provides crucial information about the efficiency of optimum solar energy conversion of a material. Fig. 6.27(a) exhibits the photon energy dependent absorption coefficient of pure and doped ZnO ceramics. According to the result, the absorption edge of both Li and Nd-doped ZnO is shifted toward the low energy region (red shift) relative to the pristine one. An additional peak is observed for both doped profile in the low energy region. The absorption edge of Nd-doped ZnO shifts more toward the lower energy region than Li-doped ZnO. The pristine ZnO shows no absorbance

in the visible light region. The metal doping in pure ZnO elevates the absorption coefficient to a great extent not only in the visible region but also in the ultraviolet region. However, there is no shift of absorption edge appeared in case of Li and Nd co-doped ZnO and the absorption profile is almost same as the pristine ZnO due to the combined effect of Li and Nd-dopant. For clear understanding the light absorption feature of ZnO in the visible region, wavelength dependent absorption coefficient is presented in Fig. 6.27(b). As shown in the figure Nd-doped ZnO has widest absorption area than the Li-doped ZnO. As like as the pristine ZnO the Li and Nd co-doped ZnO ceramics shows no absorbance in the visible range.

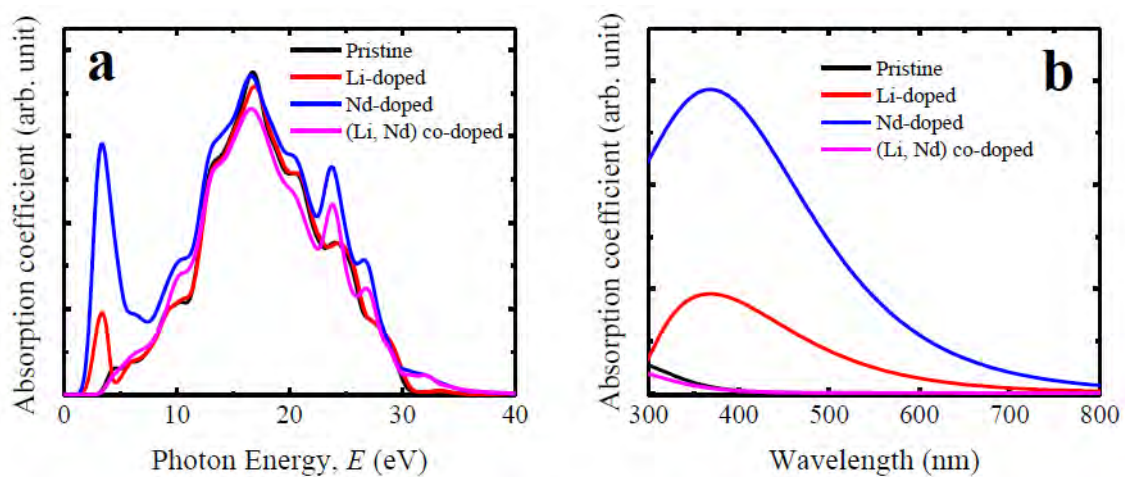


Fig. 6.27: Calculated light absorption spectra of pure and metal doped ZnO ceramics. (a) Photon energy dependent and (b) wavelength dependent absorption coefficient.

Reflectivity is one of the vital optical properties of material for photovoltaic application and is defined as the amount of light energy reflected from the surface of a material with respect to the amount of light energy incident on the surface of the material. The reflectivity spectra of pristine and doped sample for photon energy up to 40 eV are illustrated in Fig. 6.28(a). The reflectivity of individual Li and Nd doped ZnO is nearly identical with the pristine ZnO in the ultraviolet region. An additional peak is observed in the visible region for both the doped samples whereas Nd-doped ZnO has strong reflectivity in the low photon energy range than the Li-doped ZnO. The reflectivity is almost unchanged in the visible range in case of (Li,

Nd) co-doped ZnO compared with the pristine ZnO. However, the reflectivity is slightly decreased in the ultraviolet region. The optical conductivity is also defined as the photoconductivity. The conductivity spectra of doped and pristine ZnO are illustrated in Fig. 6.28(b) up to 40 eV light energy. The optical conductivity of individual Li and Nd doped ZnO is almost similar with the pure ZnO in the high energy region. A sharp peak is appeared in the visible light energy zone for both the doped profile whereas Nd-doped ZnO exhibits large photoconductivity than Li-doped ZnO. However, co-doping of Li and Nd into the ZnO ceramics does not have any major effect on the overall conductivity spectra of pure ZnO.

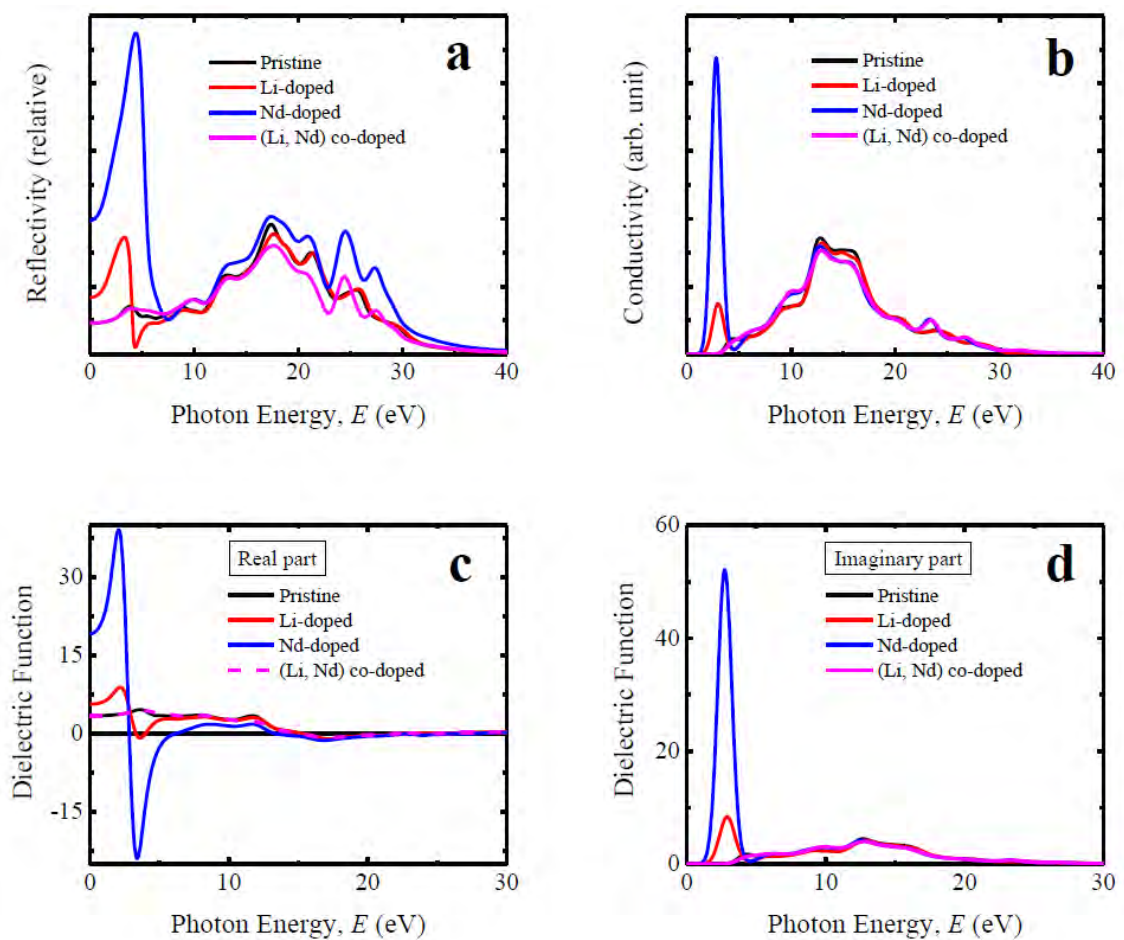


Fig. 6.28: The simulated photon energy dependent (a) Reflectivity, (b) Conductivity, (c) Real part of dielectric function and (d) Imaginary part of dielectric function of pristine and doped ZnO ceramics.

The dielectric function is characterized by the response of a material to incident light energy. The charge carrier recombination rate and hence the overall performance of optoelectronic devices depends upon the static value of dielectric function [52]. A material with high dielectric constant has relatively less charge carrier recombination rate. As a result the overall performance of optoelectronic devices is enhanced. The real and imaginary part of evaluated dielectric function of pure and doped ZnO is depicted in Figs. 6.28(c) and (d). It is evident that the Nd-doped ZnO shows relatively high dielectric constant than the pure and Li-doped ZnO. Co-doping of Li and Nd into the ZnO ceramics does not have any major effect on the dielectric constant of pure ZnO. Therefore, in terms of dielectric constant Nd-doped ZnO is a promising candidate for solar cell and optoelectronic application than the pristine one. As shown in Figs. 6.28(c) and (d) overall dielectric profile (both real and imaginary part) of doped ZnO is almost identical in the high energy region (Ultraviolet zone) with pure ZnO. The imaginary part of dielectric constant of all the samples goes to zero above 28 eV while the real part reaches approximately unity. This result implies that both the doped and pure ZnO ceramics exhibit transparency with slight absorption in the high energy zone (above 28 eV) (It is also evident from absorption coefficient graph [Fig. 6.27(a)]). Appearance of the sharp peak in the imaginary part of dielectric constant of Li and Nd doped ZnO in the visible region implies the occurrence of strong absorption in this region which also justifies the result obtained from the absorption spectra of doped ZnO. Therefore, the investigation of the dielectric constant of pure and doped ZnO suggests that pristine and individual Li and Nd doped ZnO possess high transmissivity in the high energy region (above 28 eV) and individual Li and Nd doped ZnO possess nearly zero transmissivity in the visible region. This is the reason for high absorptivity of individual Li and Nd doped ZnO in the visible region.

Bibliography

- [1] Divya, N.K. and Pradyumnan, P.P., “Enhancement of photocatalytic activity in Nd doped ZnO with an increase in dielectric constant,” *J. Mater. Sci. Mater. Electron.*, vol. 28(2), pp. 2147-2156, 2017.
- [2] Poongodi, G., Kumar, R.M. and Jayavel, R., “Structural, optical and visible light photocatalytic properties of nanocrystalline Nd doped ZnO thin films prepared by spin coating method,” *Ceram. Int.*, vol. 41(3), pp. 4169-4175, 2015.
- [3] Ullah Awan, S., Hasanain, S.K., Bertino, M.F. and Hassnain Jaffari, G., “Ferromagnetism in Li doped ZnO nanoparticles: The role of interstitial Li,” *J. Appl. Phys.*, vol. 112(10), pp.103924, 2012.
- [4] Rodriguez-Carvajal, J., “Fullprof: A Program for Rietveld Refinement and Pattern Matching Analysis,” Abstract of the Satellite Meeting on Powder Diffraction of the XV Congress of the IUCr, Toulouse, France, pp. 127, 1990.
- [5] Chauhan, S., Kumar, M., Chhoker, S., Katyal, S.C. and Awana, V.P.S., “Structural, vibrational, optical and magnetic properties of sol-gel derived Nd doped ZnO nanoparticles,” *J. Mater. Sci. Mater. Electron.*, vol. 24(12), pp. 5102-5110, 2013.
- [6] Verma, K.C. and Kotnala, R.K., “Oxygen vacancy induced by La and Fe into ZnO nanoparticles to modify ferromagnetic ordering,” *J. Solid State Chem.*, vol. 237, pp. 211-218, 2016.
- [7] Scherrer, P., “Bestimmung der inneren Struktur und der Größe von Kolloidteilchen mittels Röntgenstrahlen,” In *Kolloidchemie Ein Lehrbuch* (pp. 387-409). Springer, Berlin, Heidelberg, 1912.
- [8] Holzwarth, U. and Gibson, N., “The Scherrer equation versus the ‘Debye-Scherrer equation’,” *Nat. Nanotechnol.*, vol. 6(9), pp. 534, 2011.
- [9] “Scherrer Equation.” Wikipedia, Wikimedia Foundation, 27 Sept. 2018, en.wikipedia.org/wiki/Scherrer_equation.
- [10] Sattar, A.A., El-Sayed, H.M., El-Shokrofy, K.M. and El-Tabey, M.M., “Improvement of the magnetic properties of Mn-Ni-Zn Ferrite by the non magnetic Al-Ion substitution,” *J. Appl. Sci.*, vol. 5(1), pp. 162-168, 2005.
- [11] Huang, D., Liu, Z., Li, Y. and Liu, Y., “Colossal permittivity and dielectric relaxation of (Li, In) Co-doped ZnO ceramics,” *J. Alloys Compd.*, vol. 698, pp. 200-206, 2017.
- [12] Wu, Y., Li, J., Bai, H., He, S., Hong, Y., Shi, K. and Zhou, Z., “Colossal Dielectric Behavior

- and Dielectric Relaxation of (Li, Fe) Co-Doped ZnO Ceramics,” *Phys. Status Solidi Rapid Res. Lett.*, vol. 12(6), pp. 1800126, 2018.
- [13] Chatterjee, A., Das, D., Pradhan, S.K. and Chakravorty, D., “Synthesis of nanocrystalline nickel-zinc ferrite by the sol-gel method,” *J. Magn. Magn. Mater.*, vol. 127(1-2), pp. 214-218, 1993.
- [14] Zhang, Y. and Han, J., “Microstructure and temperature coefficient of resistivity for ZnO ceramics doped with Al₂O₃,” *Mater. Lett.*, vol. 60(20), pp. 2522-2525, 2006.
- [15] Koops, C.G., “On the dispersion of resistivity and dielectric constant of some semiconductors at audio frequencies,” *Phys. Rev.*, vol. 83(1), pp. 121, 1951.
- [16] Maxwell, J. C. (1973) *Electricity and Magnetism* . Oxford University Press, London.
- [17] Wagner, K.W., “Zur theorie der unvollkommenen dielektrika,” *Ann. Phys.*, vol. 345(5), pp. 817-855, 1913.
- [18] DoITPoMS, www.doitpoms.ac.uk/tlplib/dielectrics/loss.php.
- [19] (a) Z. W. Yin, *Dielectric Physics* , Science Press, Beijing, 2nd edn, 2003; (b) P. Lunkenheimer, V. Bobnar, A. V. Pronin, A. I. Ritus, A. A. Volkov and A. Loidhl, *Phys. Rev. B: Condens. Matter Mater. Phys.* , 2002, 66, 052105; (c) A. K. Jonscher, *Dielectric Relaxation in Solids*, Chelsea Dielectric Press, London, 1983.
- [20] Shaw, T.M., Trolier-McKinstry, S. and McIntyre, P.C., “The properties of ferroelectric films at small dimensions,” *Annu. Rev. Mater. Sci.*, vol. 30(1), pp. 263-298, 2000.
- [21] Hu, W., Liu, Y., Withers, R.L., Frankcombe, T.J., Norén, L., Snashall, A., Kitchin, M., Smith, P., Gong, B., Chen, H. and Schiemer, J., “Electron-pinned defect-dipoles for high-performance colossal permittivity materials,” *Nat. Mater.*, vol. 12(9), pp. 821, 2013.
- [22] Ke, S., Li, T., Ye, M., Lin, P., Yuan, W., Zeng, X., Chen, L. and Huang, H., “Origin of colossal dielectric response in (In + Nb) co-doped TiO₂ rutile ceramics: a potential electrothermal material,” *Sci. Rep.*, vol. 7(1), pp. 10144, 2017.
- [23] Maxwell, J.C. (1982) *A Treatise on Electricity and Magnetism*. Clarendon Press, Oxford.
- [24] Wagner, K.W., “Zur theorie der unvollkommenen dielektrika,” *Ann. Phys.*, vol. 345(5), pp. 817-855, 1913.
- [25] Miah, M.J., Khan, M.N.I. and Hossain, A.A., “Synthesis and enhancement of multiferroic properties of (x)Ba_{0.95}Sr_{0.05}TiO₃-(1-x)BiFe_{0.90}Dy_{0.10}O₃ ceramics,” *J. Magn. Magn. Mater.*, vol. 397, pp. 39-50, 2016.

- [26] Austin, I.G. and Mott, N.F., "Polarons in crystalline and non-crystalline materials," *Adv. Phys.*, vol. 18(71), pp. 41-102, 1969.
- [27] Khandekar, M.S., Kambale, R.C., Patil, J.Y., Kolekar, Y.D. and Suryavanshi, S.S., "Effect of calcination temperature on the structural and electrical properties of cobalt ferrite synthesized by combustion method," *J. Alloys Compd.*, vol. 509(5), pp.1861-1865, 2011.
- [28] Mazumdar, S.C., Khan, M.N.I., Islam, M.F. and Hossain, A.A., "Tuning of magnetoelectric coupling in $(1-y)\text{Bi}_{0.8}\text{Dy}_{0.2}\text{FeO}_{3-y}\text{Ni}_{0.5}\text{Zn}_{0.5}\text{Fe}_2\text{O}_4$ multiferroic composites," *J. Magn. Magn. Mater.*, vol. 401, pp. 443-454, 2016.
- [29] Kaiser, M., "Electrical conductivity and complex electric modulus of titanium doped nickel-zinc ferrites," *Physica B*, vol. 407(4), pp. 606-613, 2012.
- [30] Choudhary, R.N.P., Pradhan, D.K., Tirado, C.M., Bonilla, G.E. and Katiyar, R.S., "Effect of La substitution on structural and electrical properties of $\text{Ba}(\text{Fe}_{2/3}\text{W}_{1/3})\text{O}_3$ nanoceramics," *J. Mater. Sci.*, vol. 42(17), pp.7423-7432, 2007.
- [31] Pattanayak, S., Choudhary, R.N.P., Das, P.R. and Shannigrahi, S.R., "Effect of Dy-substitution on structural, electrical and magnetic properties of multiferroic BiFeO_3 ceramics," *Ceram. Int.*, vol. 40(6), pp. 7983-7991, 2014.
- [32] MacDonald, J.R. (1987) *Impedance spectroscopy*. New York: Wiley-Interscience.
- [33] Ye, H., Jackman, R.B. and Hing, P., "Spectroscopic impedance study of nanocrystalline diamond films," *J. Appl. Phys.*, vol. 94(12), pp. 7878-7882, 2003.
- [34] A. Globus, *Phys. Colloq.* 38 (1977) C1-1.
- [35] Yu, M., Hu, J., Liu, J. and Li, S., "Electromagnetic properties of multiferroic magnetoelectric $\text{BaTiO}_3\text{-Co}_x\text{Fe}_{3-x}\text{O}_4$ core-shell particles obtained by homogeneous co-precipitation," *J. Magn. Magn. Mater.*, vol. 326, pp. 31-34, 2013.
- [36] Kumar, P., Sharma, S.K., Knobel, M. and Singh, M., "Effect of La^{3+} doping on the electric, dielectric and magnetic properties of cobalt ferrite processed by co-precipitation technique," *J. Alloys Compd.*, vol. 508(1), pp. 115-118, 2010.
- [37] Verma, A. and Chatterjee, R., "Effect of zinc concentration on the structural, electrical and magnetic properties of mixed Mn-Zn and Ni-Zn ferrites synthesized by the citrate precursor technique," *J. Magn. Magn. Mater.*, vol. 306(2), pp. 313-320, 2006.
- [38] Globus, A. and Duplex, P., "Separation of susceptibility mechanisms for ferrites of low anisotropy," *IEEE Trans. Magn.*, vol. 2(3), pp. 441-445, 1966.

- [39] Zhu, Y.D., Yan, M.F., Zhang, Y.X. and Zhang, C.S., “First-principles investigation of structural, mechanical and electronic properties for Cu–Ti intermetallics,” *Comput. Mater. Sci.*, vol. 123, pp. 70-78, 2016.
- [40] Born, M., “On the stability of crystal lattices,” *I. In Mathematical Proceedings of the Cambridge Philosophical Society*, Vol. 36, No. 2, pp. 160-172, 1940, Cambridge University Press.
- [41] Rahaman, M.Z. and Rahman, M.A., “Investigation of the physical properties of two Laves phase compounds HRh_2 (H = Ca and La): A DFT study,” *Int. J. Mod. Phys. B*, vol. 32(12), pp.1850149, 2018.
- [42] Rahaman, M.Z. and Ali, M.L., “Insight into the physical properties of two niobium based compounds, Nb_3Be and Nb_3Be_2 , via a first principles calculation,” *Chin. J. Phys.*, vol. 56(4), pp. 1386-1393, 2018.
- [43] Rahaman, M.Z. and Rahman, M.A., “ ThCr_2Si_2 -type Ru-based superconductors LaRu_2M_2 (M = P and As): An ab-initio investigation,” *J. Alloys Compd.*, vol. 695, pp. 2827-2834, 2017.
- [44] Pfrommer, B.G., Côté, M., Louie, S.G. and Cohen, M.L., “Relaxation of crystals with the quasi-Newton method,” *J. Comput. Phys.*, vol. 131(1), pp. 233-240, 1997.
- [45] Rahaman, M.Z., Ali, M.L. and Rahman, M.A., “Pressure-dependent mechanical and thermodynamic properties of newly discovered cubic Na_2He ,” *Chin. J. Phys.*, vol. 56(1), pp. 231-237, 2018.
- [46] Pugh, S.F., “XCII. Relations between the elastic moduli and the plastic properties of polycrystalline pure metals,” *The London, Edinburgh, and Dublin Philosophical Magazine and Journal of Science*, vol. 45(367), pp. 823-843, 1954.
- [47] Ranganathan, S.I. and Ostoja-Starzewski, M., “Universal elastic anisotropy index,” *Phys. Rev. Lett.*, vol. 101(5), pp. 055504, 2008.
- [48] Yu, W., Zhang, J. and Peng, T., “New insight into the enhanced photocatalytic activity of N-, C-and S-doped ZnO photocatalysts,” *Appl. Catal. B.*, vol. 181, pp. 220-227, 2016.
- [49] Wen, J.Q., Zhang, J.M., Chen, G.X., Wu, H. and Yang, X., “The structural, electronic and optical properties of Nd doped ZnO using first-principles calculations,” *Physica E Low Dimens. Syst. Nanostruct.*, vol. 98, pp. 168-173, 2018.
- [50] Burstein, E., “Anomalous optical absorption limit in InSb,” *Phys. Rev.*, vol. 93(3), pp. 632, 1954.

- [51] Zhao, Z. and Liu, Q., "Effects of lanthanide doping on electronic structures and optical properties of anatase TiO₂ from density functional theory calculations," *J. Phys. D*, vol. 41(8), pp. 085417, 2008.
- [52] Liu, X., Xie, B., Duan, C., Wang, Z., Fan, B., Zhang, K., Lin, B., Colberts, F.J., Ma, W., Janssen, R.A. and Huang, F., "A high dielectric constant non-fullerene acceptor for efficient bulk-heterojunction organic solar cells," *J. Mater. Chem. A*, vol. 6(2), pp. 395-403, 2018.

CHAPTER 7

CONCLUSIONS

7.1 Summary

The present research mainly deals with the experimental investigation of structural, dielectric and magnetic properties of (Li, Nd) co-doped ZnO ceramics. The disk and toroid shaped samples are sintered at various temperatures. Different experiments are then carried out and the results are carefully analyzed to monitor the changes in structural, dielectric and magnetic properties of the studied samples. A DFT based theoretical investigation has also been carried out to study the mechanical, electronic, bonding and optical properties of (Li, Nd) co-doped ZnO ceramics. The basic outcomes of this investigation are summarized as follows,

- Multifunctional $(\text{Nd}_{0.5}\text{Li}_{0.5})_x\text{Zn}_{1-x}\text{O}$ ($x = 0.00, 0.01, 0.03, 0.05, \text{ and } 0.10$) ceramics have been prepared successfully by standard solid state reaction method.
- The XRD patterns confirm the formation of wurtzite hexagonal type zinc oxide having space group $P6_3mc$ (186). In the pristine ZnO bulk material no secondary phases are present. However, the XRD patterns of (Li, Nd) co-doped ZnO contains some secondary peaks of Nd_2O_3 phase with hexagonal type structure having space group $P6_3/mmc$ (194). The dopant ions (Li and Nd) are partially incorporated at the Zn site of ZnO ceramics due to the comparatively large ionic radius of Nd compared to Zn.
- The lattice parameters are found to extend up to 3% doping concentration. From 5% doping concentration the lattice parameters begin to decrease. This result is well consistent with the ionic radius of the constituent ions of $(\text{Nd}_{0.5}\text{Li}_{0.5})_x\text{Zn}_{1-x}\text{O}$ ceramics.
- The value of ρ_B is enhanced for all the samples sintered up to 1623 K and

begins to decrease after 1623 K. The values of ρ_B and ρ_{th} are also enhanced with the increase in doping content. This phenomenon is consistent with the atomic weight of the constituent atoms. Porosity is decreased with the increase in doping content as the samples become more dense.

- The FESEM images confirm that all the compositions contain randomly aligned non-uniform grains in size and shape due to very high sintering temperature. The distribution of grains is not homogeneous and some agglomeration is appeared in higher doped samples. Non-equivalent size of dopant ions may be the reason behind this agglomeration of grains. The average grain size is on average decreased with the increase in doping content showing similar trend as the variation of crystallites size as a function of doping content. The decrease in grain size with doping content can be attributed to the slower diffusion of larger Nd cation into ZnO ceramics. The increase in Li and Nd into ZnO leads to increase in the internal stress, resulting smaller grain size. However, the grain size is enhanced with the increase in sintering temperature.
- The frequency dependent dielectric constant (ϵ') of $(Nd_{0.5}Li_{0.5})_xZn_{1-x}O$ ceramics is measured at room temperature in the frequency range 20 Hz to 120 MHz. At lower frequencies, the higher values of ϵ' are observed due to the contributions from all four mechanisms of polarization. The value of ϵ' begins to decrease with the increase in frequency and becomes independent of frequency gradually. This phenomenon can be explained by the Koops theory based on Maxwell–Wagner model.
- The dielectric loss tangent ($\tan\delta$) is maximum at low frequency region and with the increase in frequency $\tan\delta$ is gradually decreased. The domain wall motion is suppressed at higher frequency and magnetization is changed by rotation resulting lower loss at higher frequency. There also exists some broad relaxation peaks at high frequency region.
- The values of ϵ' for $(Nd_{0.5}Li_{0.5})_xZn_{1-x}O$ ceramics are decreased with the increase in doping concentration. This phenomenon is correlated with the grain size

distribution in the corresponding samples. The dielectric loss is also reduced with the increase in dopant concentration. This phenomenon can be explained through the newly proposed dielectric polarization mechanism Electron Pinned Defect Dipole (EPDD) model.

- The value of ε' is enhanced for the 1% co-doped sample sintered up to 1623 K and then begins to decrease for further increase in T_s showing similar trend with the bulk density of the studied compositions. The dielectric loss is also decreased with the increase in T_s . However, 1% (Li, Nd) co-doped ZnO shows slightly lower dielectric constant than pristine ZnO but relatively very low dielectric loss than pure ZnO ceramics sintered at 1623 K. Hence 1% (Li, Nd) co-doped ZnO sintered at 1623 K can be regarded as the optimum sample.
- The ac-conductivity (σ_{ac}) exhibits an increasing trend with the increase in frequency of all the compositions of $(Nd_{0.5}Li_{0.5})_xZn_{1-x}O$ ceramics.
- The complex impedance plot of $(Nd_{0.5}Li_{0.5})_xZn_{1-x}O$ ceramics exhibit a tendency of forming depressed semicircular arcs indicating non Debye-type relaxation. Single semicircular arcs are formed for all the samples except 3% doped compositions. Two semicircular arcs are found in case of 3% doped ZnO ceramics. Therefore, dielectric contribution comes from both the grain and grain boundary resistance in case of 3% doped profile whereas major part of dielectric contribution comes from only the grain boundary resistance for all other compositions.
- The values of μ'_i for $(Nd_{0.5}Li_{0.5})_xZn_{1-x}O$ ceramics are almost constant over the whole range of frequency. The value of RQF increases with the increase in frequency for all the compositions. This implies that with the increase in frequency the utility of the studied compositions is enhanced.
- The theoretical investigation on mechanical properties ensures the mechanical stability of $(Nd_{0.5}Li_{0.5})_xZn_{1-x}O$ ceramics. The study of Cauchy pressure, Poisson's ratio and Pugh's ratio confirm that $(Nd_{0.5}Li_{0.5})_xZn_{1-x}O$ ceramics is ductile as the pristine ZnO. The calculated value of B , G and E suggest that

$(\text{Nd}_{0.5}\text{Li}_{0.5})_x\text{Zn}_{1-x}\text{O}$ can be classified as relatively hard ceramics.

- For explaining the bonding features of (Li, Nd) co-doped ZnO ceramics the basic electronic properties including the band structure, density of states (DOS) and charge density of the studied compositions are investigated. It is found that bonding in pure and doped ZnO is largely ionic.
- The study of optical properties indicates that the absorption profile of Li and Nd co-doped ZnO is almost same as the pristine ZnO due to the combined effect of Li and Nd-dopant. As like as the pristine ZnO the Li and Nd co-doped ZnO ceramics shows no absorbance in the visible range. Similar trend is observed for other optical parameters of $(\text{Nd}_{0.5}\text{Li}_{0.5})_x\text{Zn}_{1-x}\text{O}$ ceramics as the pristine ZnO.

7.2 Future Work

Further investigations on different aspects are possible for fundamental interest and potential applications of the studied ceramics. Following recommendations are made for further extension of the present work:

- Neutron diffraction analysis may be performed for these compositions to determine the distribution of substituted ions.
- X-ray photoelectron spectroscopy (XPS) studies may be carried out to determine the oxidation states of the substituted elements.
- Mössbauer spectroscopy can be performed to know the cation distribution.
- Transmission electron micrographs (TEM) may be taken for proper understanding of the domains.
- Ferroelectric (P-E) hysteresis loop measurement can be performed to know the ferroelectric nature of the studied compositions.
- UV-Vis spectroscopy can be performed of the studied compositions to measure the various optical properties and reflectance of light.

- Other sample preparation techniques (e.g., sol-gel, co-precipitation etc.) can be followed to prepare the studied samples for comparing the obtained properties of the present investigation.

LIST OF PUBLICATIONS

Relevant Publications

1. "An Experimental and Theoretical Insights into the Colossal Permittivity Mechanism of (Li, Nd) Co-doped ZnO Ceramics"

M. Zahidur Rahaman, Hidekazu Tanaka, A.K.M. Akther Hossain

arXiv preprint arXiv:1905.07226 (2019).

2. "Colossal Dielectric Behavior and Dielectric Relaxation of (Li, Nd) Co-doped ZnO Ceramics"

Md. Zahidur Rahaman, Abdullah Al Noman, Mithun Kumar Das, Nila Rani Kundu, A.K.M. Akther Hossain

National Conference on Physics-2019 organized by Bangladesh Physical Society, February 2019, Dhaka, Bangladesh.

Other Publications

1. "Effect of metal doping on the visible light absorption, electronic structure and mechanical properties of non-toxic metal halide CsGeCl₃"

Md. Zahidur Rahaman, A.K.M. Akther Hossain

RSC Advances 8.58 (2018): 33010-33018. (The Royal Society of Chemistry)

2. "Effect of Y substitution on magnetic and transport properties of Ba_{0.95}La_{0.05}Ti_{1-x}Y_xO₃ ceramics"

A. Ahad, M.A. Taher, Mithun Kumar Das, **M. Zahidur Rahaman**, M.N.I. Khan

Results in Physics 12 (2019): 1925-1932. (Elsevier)

3. "Analysis of grain growth, structural and magnetic properties of Li-Ni-Zn ferrite under the influence of sintering temperature"

M. A. Islam, **M. Zahidur Rahaman**, Md. Mehedi Hasan, A.K.M. Akther Hossain

Heliyon 5.2 (2019): e01199. (Elsevier)